Investigation of Ultrafast Molecular Dynamics via Covariance Mapping

A Tool for Intense XUV Light Sources

Lahl, Jan

2019

Document Version:
Publisher's PDF, also known as Version of record

Link to publication

Citation for published version (APA):
Lahl, J. (2019). *Investigation of Ultrafast Molecular Dynamics via Covariance Mapping: A Tool for Intense XUV Light Sources*. [Doctoral Thesis (compilation), Lund University]. Department of Physics, Lund University.

Total number of authors:
1

LUND UNIVERSITY

PO Box 117
221 00 Lund
+46 46-222 00 00

Investigation of Ultrafast Molecular Dynamics via Covariance Mapping

A Tool for Intense XUV Light Sources

JAN LAHL
FACULTY OF ENGINEERING | LUND UNIVERSITY

Investigation of Ultrafast Molecular Dynamics via Covariance Mapping

Investigation of Ultrafast Molecular Dynamics via Covariance Mapping

A Tool for Intense XUV Light Sources

by Jan Lahl

LUND
UNIVERSITY

Thesis for the degree of Doctor of Philosophy
Thesis advisors: Dr. Per Johnsson, Prof. Anne L'Huillier
Faculty opponent: Prof. László Veisz

To be presented, with the permission of the Faculty of Engineering of Lund University, for public criticism in the Rydberg Hall (Rydbergsalen) at the Department of Physics on Friday, the 29th of March 2019 at 13:15.

Organization **LUND UNIVERSITY** Department of Physics Box 118 SE–221 00 LUND Sweden	Document name **DOCTORAL DISSERTATION**
	Date of disputation 2019-03-29
	Sponsoring organization
Author(s) Jan Lahl	

Title and subtitle

Investigation of Ultrafast Molecular Dynamics via Covariance Mapping: A Tool for Intense XUV Light Sources

Abstract

The study of molecular dynamics involves observations of the motion of nuclei and electrons. While nuclear motion is usually on the picosecond or femtosecond timescale, attosecond precision is necessary to directly observe the motion of electrons. Ultrashort laser pulses have become established as a viable tool for probing femtosecond dynamics by irradiating the target for only extremely short times. This allows snapshots of the motion to be obtained. However, extreme ultraviolet (XUV) or soft X-ray wavelengths are required to generate attosecond pulses. Two light sources that produce ultrashort XUV pulses were used during the work presented in this thesis: the free electron laser in Hamburg (FLASH) and the high-order harmonic generation-based light source at the High-Intensity XUV Beamline in Lund.

This thesis describes the application of covariance mapping and pump-probe spectroscopy as tools to investigate molecular dynamics at these XUV light sources. A covariance mapping scheme was implemented in conjunction with a double-sided velocity map imaging spectrometer at the High-Intensity XUV Beamline. Its capabilities were demonstrated in a proof-of-principle experiment on molecular nitrogen. The scheme was subsequently applied to more complex molecules, and results from photoion-photoion covariance mapping of adamantane ($C_{10}H_{16}$) are presented. The photodissociation behavior of halomethane molecules was investigated with infrared - ultraviolet and ultraviolet - soft X-ray pump-probe schemes during several measurement campaigns at FLASH. While these time-resolved experiments probed dynamics mainly on the picosecond timescale, efforts were made at the High-Intensity XUV Beamline towards attosecond precision XUV-XUV pump-probe experiments. After demonstrating the ability to induce two-photon processes with XUV light, the XUV wavefronts were studied over several experimental campaigns. These campaigns led to a significant reduction of aberrations in the XUV wavefronts. The size and quality of the XUV focal spot as well as the XUV generation yield were improved.

Key words

Covariance, Ultrafast, High-order Harmonic Generation, HHG, Extreme Ultraviolet, XUV, Pump Probe, FLASH, Velocity Map Imaging, Wavefront, FEL, Photodissociation, Coulomb Explosion

Classification system and/or index terms (if any)

Supplementary bibliographical information		Language English
ISSN and key title <0281 − 2762>		ISBN 978-91-7753-976-6 (print) 978-91-7753-977-3 (pdf)
Recipient's notes	Number of pages 222	Price
	Security classification	

Signature Lahl Date 2019-02-18

Investigation of Ultrafast Molecular Dynamics via Covariance Mapping

A Tool for Intense XUV Light Sources

by Jan Lahl

LUND
UNIVERSITY

A doctoral thesis at a university in Sweden takes either the form of a single, cohesive research study (monograph) or a summary of research papers (compilation thesis), which the doctoral student has written alone or together with one or several other author(s).

In the latter case the thesis consists of two parts. An introductory text puts the research work into context and summarizes the main points of the papers. Then, the research publications themselves are reproduced, together with a description of the individual contributions of the authors. The research papers may either have been already published or are manuscripts at various stages (in press, submitted, or in draft).

Funding information: This project has received funding from the European Union's Horizon 2020 research and innovation programme under the Marie Skłodowska-Curie grant agreement No 641789.

Faculty of Engineering, Department of Physics

Lund Reports on Atomic Physics, LRAP 554 (2019)
ISBN: 978-91-7753-976-6 (print)
ISBN: 978-91-7753-977-3 (pdf)
ISSN: <0281-2762>

Printed in Sweden by Media-Tryck, Lund University, Lund 2019

A German joke is no laughing matter.
Mark Twain, or was it Oscar Wilde...?

Abstract

The study of molecular dynamics involves observations of the motion of nuclei and electrons. While nuclear motion is usually on the picosecond or femtosecond timescale, attosecond precision is necessary to directly observe the motion of electrons. Ultrashort laser pulses have become established as a viable tool for probing femtosecond dynamics by irradiating the target for only extremely short times. This allows snapshots of the motion to be obtained. However, extreme ultraviolet (XUV) or soft X-ray wavelengths are required to generate attosecond pulses. Two light sources that produce ultrashort XUV pulses were used during the work presented in this thesis: the free electron laser in Hamburg (FLASH) and the high-order harmonic generation-based light source at the High-Intensity XUV Beamline in Lund.

This thesis describes the application of covariance mapping and pump-probe spectroscopy as tools to investigate molecular dynamics at these XUV light sources. A covariance mapping scheme was implemented in conjunction with a double-sided velocity map imaging spectrometer at the High-Intensity XUV Beamline. Its capabilities were demonstrated in a proof-of-principle experiment on molecular nitrogen. The scheme was subsequently applied to more complex molecules, and results from photoion-photoion covariance mapping of adamantane ($C_{10}H_{16}$) are presented. The photodissociation behavior of halomethane molecules was investigated with infrared - ultraviolet and ultraviolet - soft X-ray pump-probe schemes during several measurement campaigns at FLASH. While these time-resolved experiments probed dynamics mainly on the picosecond timescale, efforts were made at the High-Intensity XUV Beamline towards attosecond precision XUV-XUV pump-probe experiments. After demonstrating the ability to induce two-photon processes with XUV light, the XUV wavefronts were studied over several experimental campaigns. These campaigns led to a significant reduction of aberrations in the XUV wavefronts. The size and quality of the XUV focal spot as well as the XUV generation yield were improved.

Contents

Thesis **1**

List of publications

This thesis is based on the following publications, referred to by their Roman numerals. First authors and authors of equal contribution are marked bold, the author of this thesis is underlined:

I **Two-photon double ionization of neon using an intense attosecond pulse train**

B. Manschwetus, L. Rading, F. Campi, S. Maclot, H. Coudert-Alteirac, J. Lahl, H. Wikmark, P. Rudawski, C. M. Heyl, B. Farkas, T. Mohamed, A. L'Huillier, and P. Johnsson
Physical Review A, 93, 6, pp. 1-4 (2016)

II **Coulomb-explosion imaging of concurrent CH2BrI photodissociation dynamics**

M. Burt, R. Boll, J.W.L. Lee, K. Amini, H. Köckert, C. Vallance, A.S. Gentleman, S.R. Mackenzie, S. Bari, C. Bomme, S. Düsterer, B. Erk, B. Manschwetus, E. Müller, D. Rompotis, E. Savelyev, N. Schirmel, S. Techert, R. Treusch, J. Küpper, S. Trippel, J. Wiese, H. Stapelfeldt, B. Cunha De Miranda, R. Guillemin, I. Ismail, L. Journel, T. Marchenko, J. Palaudoux, F. Penent, M.N. Piancastelli, M. Simon, O. Travnikova, F. Brausse, G. Goldsztejn, A. Rouzée, M. Géléoc, R. Geneaux, T. Ruchon, J. Underwood, D.M.P. Holland, A.S. Mereshchenko, P.K. Olshin, P. Johnsson, S. Maclot, J. Lahl, A. Rudenko, F. Ziaee, M. Brouard, and D. Rolles
Physical Review A, 96, 4, pp. 1-8 (2017)

III **Micro-Focusing of Broadband High-Order Harmonic Radiation by a Double Toroidal Mirror**

H. Coudert-Alteirac, H. Dacasa, F. Campi, E. Kueny, B. Farkas, F. Brunner, S. Maclot, B. Manschwetus, H. Wikmark, J. Lahl, L. Rading, J. Peschel, B. Major, K. Varjú, G. Dovillaire, P. Zeitoun, P. Johnsson, A. L'Huillier, and P. Rudawski
Applied Sciences, 7, 11, 1159 (2017)

IV **Time-resolved inner-shell photoelectron spectroscopy: From a bound molecule to an isolated atom**

F. Brauße, G. Goldsztejn, K. Amini, R. Boll, S. Bari, C. Bomme, M. Brouard, M. Burt, B. Cunha De Miranda, S. Düsterer, B. Erk, M. Géléoc, R. Geneaux, A.S. Gentleman, R. Guillemin, I. Ismail, P. Johnsson, L. Journel, T. Kierspel, H. Köckert, J. Küpper, P. Lablanquie, J. Lahl, J.W.L. Lee, S.R. Mackenzie, S. Maclot, B. Manschwetus, A.S. Mereshchenko, T. Mullins, P.K. Olshin, J. Palaudoux, S. Patchkovskii, F. Penent, M. N. Piancastelli, D. Rompotis, T. Ruchon, A. Rudenko, E. Savelyev, N. Schirmel, S. Techert, O. Travnikova, S. Trippel, J.G. Underwood, C. Vallance, J. Wiese, M. Simon, D.M.P. Holland, M. Marchenko, A. Rouzée, and D. Rolles
Physical Review A, 97, 4, pp. 1-10 (2018)

V **A Versatile Velocity Map Ion-Electron Covariance Imaging Spectrometer for High-Intensity XUV Experiments**

L. Rading, J. Lahl, S. Maclot, F. Campi, H. Coudert-Alteirac, B. Oostenrijk, J. Peschel, H. Wikmark, P. Rudawski, M. Gisselbrecht, and P. Johnsson
Applied Sciences, 8, 6, 998 (2018)

VI **Coulomb explosion imaging of CH3I and CH2ClI photodissociation dynamics**

F. Allum, M. Burt, K. Amini, R. Boll, H. Köckert, P.K. Olshin, S. Bari, C. Bomme, F. Brauße, B. Cunha de Miranda, S. Düsterer, B. Erk, M. Géléoc, R. Geneaux, A.S. Gentleman, G. Goldsztejn, R. Guillemin, D.M.P. Holland, I. Ismail, P. Johnsson, L. Journel, J. Küpper, J. Lahl, J.W.L. Lee, S. Maclot, S.R. Mackenzie, B. Manschwetus, A.S. Mereshchenko, R. Mason, J. Palaudoux, M.N. Piancastelli, F. Penent, D. Rompotis, A. Rouzée, T. Ruchon, A. Rudenko, E. Savelyev, M. Simon, N. Schirmel, H. Stapelfeldt, S. Techert, O. Travnikova, S. Trippel, J.G. Underwood, C. Vallance, J. Wiese, F. Ziaee, M. Brouard, T. Marchenko, and D. Rolles
The Journal of Chemical Physics, 149, 20, 204313 (2018)

VII **Spatio–temporal coupling of attosecond pulses**

H. Wikmark, C. Guo, J. Vogelsang, P. W. Smorenburg, H. Coudert-Alteirac, J. Lahl, J. Peschel, P. Rudawski, H. Dacasa, S. Carlström, S. Maclot, M. B. Gaarde, P. Johnsson, C. L. Arnold, and A. L'Huillier
Proceedings of the National Academy of Sciences of the United States of America, accepted for publication

VIII **Single-shot extreme-ultraviolet wavefront measurements of high-order harmonics**

H. Dacasa, H. Coudert-Alteirac, C. Guo, E. Kueny, F. Campi, J. Lahl, J. Peschel, H. Wikmark, B. Major, E. Malm, D. Alj, K. Varjú, C. L. Arnold, G. Dovillaire, P. Johnsson, A. L'Huillier, S. Maclot, P. Rudawski, and P. Zeitoun
Optics Express, 27, 3, pp. 2656-267 (2019)

Other related publications by the author:

Ultrafast dynamics of methyl iodide studied with XUV Free-Electron Laser

Y. Cheng, B. Oostenrijk, J. Lahl, S. Maclot, S. Augustin, G. Schmid, K. Schnorr, S. Meister, D. Rompotis, B. Manschwetus, C. Bomme, B. Erk, D. Rolles, R. Boll, P. Olshin, A. Rudenko, M. Meyer, P. Johnsson, R. Moshammer, and M. Gisselbrecht
Manuscript in preparation

Acknowledgments

First and foremost I want to thank my *handledare* Per, for giving me the opportunity to do my PhD here, in this most welcoming group. Your support in even the tougher times is something one can always count on. Thank you for teaching me how to deal with never ending to do lists (In case anyone asks: just don't do everything. ;)). You always ask the right questions when we were out of ideas in the lab, or you just show up, flip a switch/push a button and it just works! Thank you for always being so optimistic and dedicated to the group's success and wellbeing.

I also want to especially thank Anne, my co-supervisor, for supporting not just me, but every member of the Atto group. You are always approachable and have time, even in the busiest of times. The positive atmosphere, the work and research environment that you facilitate is what makes the group such a great place to be a part of. I admire your enthusiasm and the ability to still have this spark of passion for science when we are onto something new.

I already started talking about it: the Atto group. I had the time of my life in these 4 years here, thank you all so much. No better place to work, research, lunch, complain, have coffee, eat cake, make puns, defend dissertations, argue, have coffee, teach, go to meetings, learn more clichés about other cultures, count the number of German and French people, complain, burn optics, burn filters, have coffee, burn cameras, misalign lasers, eat cake, talk to Mathieu endlessly, make fun of Danish, complain, make fun of Scanian (be careful though), write papers, have coffees... you might start to see the pattern by now. Thank you Christoph, Miguel, Marcus, Anne H, Ello, Maïte, Stefanos, Arthur, Esben, Bastian, Saikat, Marija, Lisa, Simon, Shekhar (we have to play Bridge again!), Emma K, David K, Alexandre, Timothé, Ingrid, wavefront Fabian, Hugo L, Sara, Marcus, Cord, Mathieu, Chen, Jan (not me), Shiyang, Ivan. Thank you Samuel for being such a good person, take care of the bees! Thank you Emma for all the great little (or often longer) chats and being such a good friend. David, you are going to complain about whatever I write here, good. Neven, thank you for all the good times and laughs we had and for letting me know about the lizard ways. Anna, thank you for your backing in the more difficult times and for making bad puns from time to time, way to go. Lana, thank you for being so outspoken, this is a very refreshing quality up here, say hi to Vuk. Fabian, one day (or rather night) we'll get you that crown back, thanks for all the fun we had. Yu-Chen, one day, you'll find people that appreciate your amazing singing voice more than we do, Sylvain and I will then probably still argue about the color of my phone though.

Next up, the 10Hz team. Our laser might have lowest rep-rate, but our music has the most bpm. Sylvain, best mustache east of Mexico, thanks for all the good times and especially all the good meals! Thanks Piotr for being such a friendly person and all the fun we had.

Fillipo, it is good to know someone that has an even worse sense of humor than me, thank you for that. Thank you Hampus for sharing these great 4 years in the group with me and literally showing me (the) Magic®. Thanks Jasper for the nice times in the office and for letting me know where the real north is. Thank you Linnea for teaching me so much about the VMIS, the many *pingis* matches and for your great "Unswedish" moments. Thanks Hélène, for all the funny conversations in which we cemented the French-German friendship. Thanks to Hugo, for letting me know how things in Spain are even more stupid sometimes, hilarious chats. Thanks to all the 3 Balázs, especially Balázs M for being such a fun office mate.

To be part of the Medea network was such a unique opportunity and experience. It was a real privilege: the summer/winter schools, the network meetings, journal clubs and webinars were so valuable for the PhD education and the networking. Special thanks to the management; to Giuseppe for doing such a great job leading the network; to Johan helping us in all the educational parts and for showing us that outreach can be fun; to Anders for tracking our progress and all the great courses you lectured; Panos for welcoming me at Photek. Thank you to all my fellow MEDEA peers, you are the reason this network was so much fun. Cheers James! Where is Nils by the way? On a more serious note: I would like to acknowledge my Master thesis supervisor Maria Krikunova, for supporting me in finding a PhD position abroad and Marc Vrakking for advising me to apply for the position in the MEDEA network here in Lund.

I would also like to acknowledge all the collaborators from the FLASH campaigns: Daniel, Rebecca, Benjamin, Dimitrios, Joss, Melanie, Pragya, Donatella, Sadia, Amanda, Pavel, Christopher, Felix, Cedric, Jochen, Arnaud and probably about 50 more... Thanks Arne, for having coffees with me at DESY and generally having a good time in Hamburg in between the FEL shifts.

What I said about the atmosphere in the group, being a great place to work, applies also to the whole Division of Atomic Physics. Beginning with Claes-Göran, who puts great emphasis on maintaining this environment. The remaining professors and lecturers/senior researcher are contributing to this of course: Lars Engström, tirelessly managing the teaching, Lars Rippe, cracking the loudest jokes, Stefan Kröll, Olle Lundh, Andreas Walther, Sune Svanberg and so on. Thank you Anders for keeping the laser running, every year, the summer holidays prove that we would be lost without you (or at least the majority of the pulse energy would be). A very special mention here should also go to Anne PJ, Jakob and Åke, I wouldn't have made through my first month without you, let alone 4 years! Thanks also to Diego, Giada, Isabel, Henrik, Martin, Lovisa, Hannes, Kristoffer, Åsa, Jonas, Jenny, Bart, Arman. Sasha, for your efforts to be better person, sometimes. And everyone I didn't mention from the Division.

Shoutout to the SEV, for all the fun during the long Swedish winter evenings: Morjo, Celin, Roshan, Suro, Andreas, Richard, Axel. Thanks to the Govindas man, for being a seemingly endless source of friendliness. Thanks also to the "new" (not the old) coffee machine in the division, the CFEL coffee machine and the chocolate vending machine for making my thesis possible. I would like to use the opportunity to explicitly exclude Skånetrafiken from the acknowledgments, they made it impossible to ever show up on time for a 9 sharp meeting and always manage to cancel exactly my train or at least delay it considerably, without advance notice. Thank you for having me wait for a replacement bus in Gantofta that doesn't show up, repeatedly. The frequency of the occurrence of "signalfel" is so periodical, it could be interpreted as actual signal.

Zu guter Letzt: vielen Dank an meine Familie, speziell meine Eltern, für die jahrelange Unterstützung. Es scheint, dass mit fast 32 Jahren, meine Ausbildung bald tatsächlich beendet ist. Lebenslanges Lernen haben sie gesagt, hätte gedacht das Leben sei länger. Danke Sandra, dass du mich die ganzen Jahre ausgehalten hast, obwohl ich meist mit dem Kopf bei der Arbeit war. Und Momo, bleib flauschig.

Popular summary in English

Explosions are not just spectacular, on a molecular level they can contain valuable information about the nature of the exploding molecule. These molecular explosions (Coulomb explosion) can be initiated by focusing intense laser beams onto the molecules. This pumps them with big amounts of energy. The molecules release this energy by emitting negatively charged electrons, causing the molecules to build up positive electrical charges. These charges distribute within the molecule and repel each other so strongly that they overcome the forces that hold the molecule together. The molecule literally explodes. Today, unprecedented amounts of data can be accumulated imaging processes like these molecular explosions. In most cases the data consists of several hundreds of gigabytes (GB) of pictures. The main tasks after the data is collected are data management, analysis and interpretation. Also in the more fundamental sciences, handling of big data is one of the main challenges of the 21st century. But often, smart statistical approaches can be applied to overcome this challenge for both the scientists and almost more importantly, their computers.

Statistics are everywhere Most statistical tools have been around in science for more than a hundred years now. But only since the dawn of computers, the amounts of data and the complexity of the data recorded have exceeded dimensions that can be easily grasped by the human mind and simple statistics like averages and variance. But especially multivariate analysis, which is the investigation of the combined statistical behavior of several measured quantities, became increasingly important recently. In the non-academic world, banks and investment funds use these tools to analyze their portfolios of stocks. Their goal is to hedge (as in hedge fund) their investments against losses, which they would make if one of the stocks they invested in would lose in value. A thorough analysis of the market situation and the relationships of the stocks would have them invest in stocks whose value is not correlated to the stocks they already invested in. That means: if one loses value, the others don't necessarily follow suit. A successful fund might hold a number of those unrelated stocks, in order to cushion the blow of losses in some of their investments.

Snapshots of molecular explosions In the world of science however, big amounts of data are prominent for decades by now and scientists and engineers applied the tools of statistics to make these mountains of data manageable. In this work, advanced statistical methods were applied to analyze the behavior of molecules that are irradiated by intense ultraviolet (UV) laser light. By initiating and observing basic processes within rather simple molecules, the aim is to understand mechanisms in larger biomolecules, like DNA. For example those, that are responsible for the protection from most damages caused by the sun's UV light or play a role in photosynthesis. In the results, depicted in Figure 0.3, dynamics were recorded in a particular carbohydrate molecule: $C_{10}H_{16}$, adamantane. It is the smallest diamond-

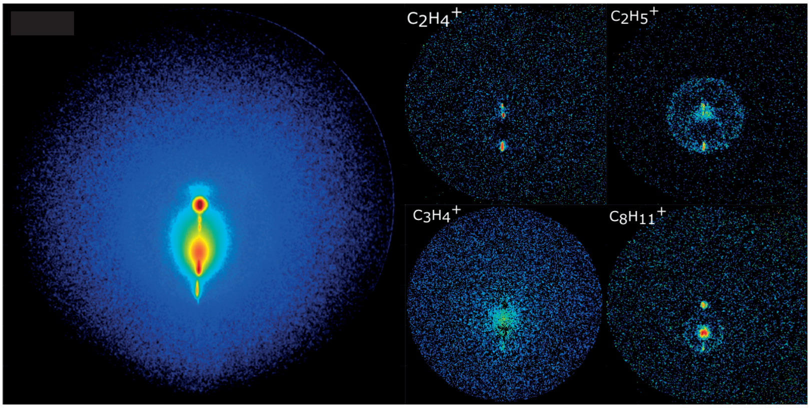

Figure 0.1: Example of data treatment by statistical means: The left half represents a 270 GB dataset that contains the contributions of about 30 different molecular fragments, collected over more than 200 000 laser shots. Filtering via multivariate analysis unveiled the individual contributions of each of these fragments. The panels on the right half show the results for 4 selected fragment. These images contain valuable information about the molecular dynamics that occurred after the molecule was irradiated with intense UV light. The rings in the images of $C_2H_5^+$ and $C_8H_{11}^+$ are hallmarks for a so-called Coulomb explosion, which was predicted from an earlier investigation.

structured molecule in nature. After the molecule was subjected to the intense laser light, the products of the ensuing breakup were imaged for more than 200 000 laser shots. In the analysis process, several Coulomb explosion reactions were successfully identified and analyzed. This information about the breakup behavior can be crucial to understand the mechanisms of energy and charge transfer within the molecule. This knowledge may then be applied to more complex systems.

Big data is one of today's biggest challenges Steady improvement of the measurement apparatus as well as the methodology will lead to improvement of our understanding of the physical processes and chemical reactions in relevant biomolecules. This could lead to unprecedented innovations in biotechnology, medicine, food and energy production or the chemical industry. One of todays' biggest challenges on this path is the management of the enormous amounts of data and their efficient analysis. But the scientific community among many others are steadily pushing forward to overcome these challenges.

Populärwissenschaftliche Zusammenfassung auf Deutsch

Explosionen sind nicht nur spektakulär: auf molekularem Niveau können sie wertvolle Informationen über die Natur der explodierenden Teilchen enthalten. Diese molekularen Explosionen (sogenannte Coulomb-Explosionen) kann man einleiten, indem intensive Laserstrahlung auf die Moleküle fokussiert wird, welche sie mit großen Mengen Energie aufpumpt. Ein großer Teil dieser Energie kann durch das Aussenden von elektrisch negativ geladenen Elektronen abgegeben werden. Jedoch laden sich die Moleküle dadurch positiv auf, diese Ladungen verteilen sich und einzelne Teile beginnen sich dadurch voneinander abzustoßen. Sobald diese Abstoßung stärker ist als die Kräfte, welche die Moleküle zusammen halten, explodieren sie förmlich. Beim Aufzeichnen dieser Explosionen und anderer Prozesse werden heutzutage zuvor unerreichte Datenmengen aufgenommen. Datensätze können leicht Größen von mehreren hundert Gigabyte (GB) annehmen. Die Hauptaufgaben bestehen dann darin, die Daten zu sichern, analysieren und zu interpretieren. Gerade in den Grundlagenwissenschaften ist das Handhaben dieser gewaltigen Datenmengen, auch als Big Data bezeichnet, eine der großen Herausforderungen des 21. Jahrhunderts. Oftmals jedoch, gelingt es, statistische Methoden geschickt anzuwenden um dieser Schwierigkeiten Herr zu werden, die ansonsten den Wissenschaftlern und fast noch viel mehr ihren Computern drohen.

Statistik ist überall Die meisten statistischen Methoden sind in der Wissenschaft seit mehr als 100 Jahren längst etabliert. Aber erst seit der Ära der Computer, sind die Datenmengen und ihre Komplexität in einem Maße gewachsen, welches nicht mehr einfach durch den menschlichen Verstand und einfache statistische Mittel wie Mittelwerte und Varianzen erfasst werden können. Aber speziell multivariate Analysis, welche die Untersuchung des kombinierten statistischen Verhaltens mehrerer gemessener Größen umfasst, wurde in jüngster Vergangenheit immer bedeutender. Außerhalb der akademischen Welt verwenden zum Beispiel Banken und Investmentfonds diese Methoden um Aktienportfolios zu analysieren. Das Ziel ist hier sich gegen Verluste abzusichern, falls eines der Wertpapiere in das investiert wurde an Wert verliert. Eine sorgfältige Marktanalyse und Untersuchung der Abhängigkeiten zwischen den Aktienwerten führt dazu, dass nur Wertpapiere ausgewählt werden deren Kurse nicht miteinander korrelieren. Ein erfolgreicher Fond hält für gewöhnlich eine Vielzahl solcher unabhängiger Positionen um gegen Verluste einzelner Aktien abgesichert zu sein.

Momentaufnahmen von molekularen Explosionen In der Wissenschaftswelt sind große Datenmengen schon seit Jahrzehnten ein Thema: Wissenschaftler und Ingenieur gleichermaßen verwenden statistische Mittel um diese Datenberge zu beherrschen. In dieser Arbeit werden komplexe statistische Methoden verwendet um das Verhalten von Molekülen zu erforschen, die intensiver ultravioletter (UV) Strahlung ausgesetzt sind. Dazu werden

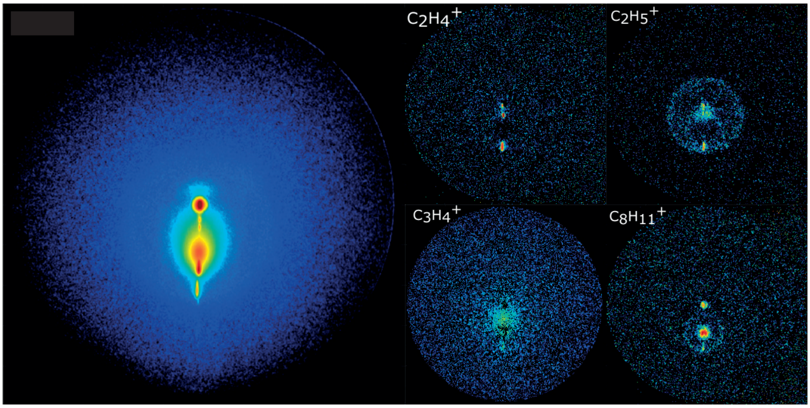

Abbildung 0.2: Datenanalyse durch Statistik: Links wird ein 270 GB großer Datensatz abgebildet, aufgenommen in über 200.000 Bildern. Darin sind Beiträge von mehr als 30 Molekülfragmenten enthalten. Durch multivariate Analyse konnten diese Beiträge isoliert werden. Rechts sind Ergebnisse von 4 ausgewählten Fragmenten zu sehen. Diese Bilder enthalten aufschlussreiche Informationen über die Vorgänge, die während und nach der Bestrahlung mit dem intensiven UV Licht abgelaufen sind. Die Ringe in den Abbildungen von $C_2H_5^+$ und $C_8H_{11}^+$ sind Kennzeichen für sogenannte Coulomb-Explosionen, welche durch frühere Untersuchungen vorhergesagt wurden.

grundlegendere Prozesse in eher kleinen Molekülen ausgelöst und untersucht. Das Ziel ist es, dadurch Einsicht in die komplexen Mechanismen in großen Biomolekülen wie der DNS zu gewinnen. Interessant sind etwa Vorgänge, welche die Moleküle vor den zerstörerischen Auswirkungen von UV Strahlung schützen oder in der Photosynthese eine Rolle spielen. In Abbildung 0.2 werden die Ergebnisse einer solchen statistischen Analyse gezeigt. Das untersuchte Molekül, Adamantane ($C_{10}H_{16}$), ist die kleinste mögliche Diamantstruktur in der Natur. Es wurde zunächst mit intensivem UV Laserlicht beschossen, um dann die Produkte des darauffolgendem Zerfalls aufzuzeichnen. Dieser Vorgang wurde für über 200.000 Laserschüsse wiederholt, um ausreichend Statistik aufzunehmen. In der anschließenden Analyse konnten mehrere Coulomb-Explosionen identifiziert und ausgewertet werden. Die gewonnen Informationen über den Zerfall könnten wesentlich zum Verständnis der Energie- und Ladungsverschiebungen innerhalb der Moleküle beitragen, und dann auf komplexere Systeme angewendet werden.

Big Data ist eine der größten Herausforderungen von heute Stetige Verbesserung der Messapparate und der Methodologie führen zu immer besserem Verständnis der physikalischen und chemischen Prozesse in Biomolekülen. Dies könnte zu bislang unerreichten Innovationen in Biotechnologie, Medizin, Nahrungs- und Energieproduktion und der chemischen Industrie führen. Eine der größten Herausforderungen auf diesem Weg ist der Umgang mit den enormen Datenmengen, die erzeugt werden und ihre effiziente Analyse. Deswegen arbeitet neben vielen anderen Teilen der Gesellschaft, auch die Wissenschaft fortlaufend an neuen Wegen um diese Herausforderungen zu bewältigen.

Populärvetenskaplig sammanfattning på svenska

Explosioner är inte bara spektakulära, utan innehåller också värdefull information på molekylnivå om den exploderande molekylen. Dessa molekylära explosioner (Coulomb-explosioner) kan startas genom att fokusera starka laserstrålar på molekylerna, vilket tillför molekylerna stora mängder energi. Molekylerna frigör denna energi genom att skicka ut negativt laddade elektroner, vilket gör en positiv laddning byggs up hos molekylen. Laddningen fördelas i molekylen och den repellerande kraften från olika delar av molekylen med positiv elektrisk laddning blir till slut större än krafterna som håller ihop molekylen. Molekylen kommer då bokstavligt talat att explodera. I dag är det möjligt att dokumentera mer information än någonsin tidigare om dessa molekylära explosioner. I de flesta fall innefattar dokumentationen så mycket information att datamängden uppgår till flera hundra gigabytes (GB). Efter att informationen samlats in är det en utmaning att hantera datamängden, och att analysera och tolka informationen den innehåller. Inom grundforskninger räknas hanteringen av ”Big data” till en av 2000-talets största utmaningar. Dock kan smarta statistiska tekniker tillämpas, för att övervinna denna utmaning.

Statistik finns överallt. Statistiska verktyg har använts i forskningssyfte i mer än hundra år. Men det är bara efter att datorerna dök upp som mängden information och informationens komplexitet blivit större än vad mänskliga hjärnor och enkel statistik som medelvärden och varians kan hantera. Därför har multivariat analys, som undersöker det kombinerade statistiska beteendet hos flera uppmätta variabler, på senare tid blivit allt viktigare. I den icke-akademiska världen använder banker och investeringsfirmor dessa verktyg för att analysera sina aktieportföljer. Deras mål är att skydda sina investeringar mot förluster som skulle kunna uppstå om någon aktie de investerat i skulle sjunka i värde. En grundlig undersökning av aktiemarknadens tillstånd och olika aktiekursers inflytande på varandra kan se till att de investerar i aktier vars kurs inte påverkas av kursen hos aktier de redan äger. Det innebär att om en (aktie) sjunker i värde så behöver det inte betyda att de andra följer efter. En framgångsrik fond kan ha ett flertal aktier som inte påverkas av varandra för att dämpa effekten av en förlust hos en del av deras placeringar.

Ögonblicksbilder av molekylära explosioner Inom forskningsvärlden emellertid, har stora mängder information varit en vanlig företeelse i flera decennium och forskare och ingenjörer använder statistiska metoder för att göra dessa gigantiska mängder av information hanterbara. I denna avhandling används avancerade statistiska metoder för att analysera molekylers beteende när de bestrålas med starkt ultraviolett (UV) ljus. Förhoppningen är att kunna förstå de kemiska mekanismerna i stora biomolekyler, som exempelvis DNA, genom att initiera och observera fundamentala processer hos enklare molekyler. Andra exempel på stora biomolekyler är molekyler som skyddar oss från skador orsakade av från

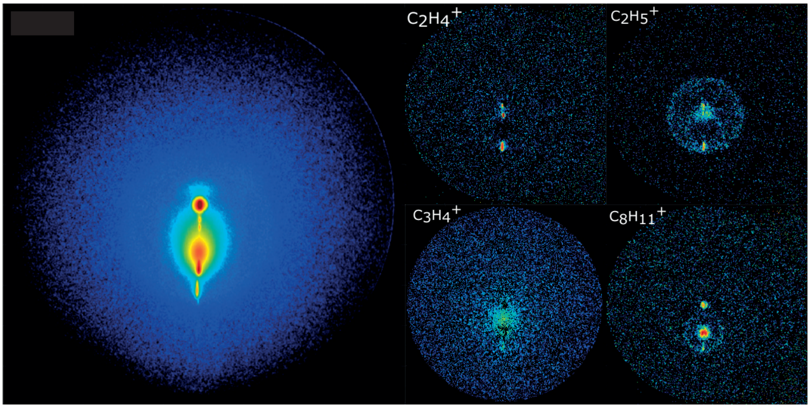

Figur 0.3: Exempel på hur information kan se ut efter att statistiska verktyg tillämpats: den vänstra halvan ($C_{10}H_{16}$) innehåller information från en datamängd på 270 GB där 30 olika fragment av molekyler dokumenterats under mer än 200000 laserpulser. Genom att behandla den insamlade informationen med multivariat analys kunde varje enskilt fragments bidrag urskiljas. Panelerna på den högra sidan visar utfallet för fyra utvalda fragment. Dessa bilder visar värdefull information om den molekylära dynamiken som uppstod efter att molekylen belysts med starkt UV-ljus. Ringarna i $C_2H_5^+$-bilden och $C_8H_{11}^+$ kännetecknar en så kallad Coulombexplosion.

solens UV-ljus, eller molekyler som är delaktiga i fotosyntesen. I resultaten som visas i bild 0.3, dokumenterades dynamiska processer hos en särskild molekyl: $C_{10}H_{16}$, Adamantan. Det är den minsta molekylen med diamantstruktur som förekommer naturligt. Efter att molekylen blivit belyst med laser UV-ljus dokumenterades produkterna av dess nedbrytning, för mer än 200000 laserpulser. Under bildanalysen hittades och analyserades flera Coulombexplosioner. Denna information om nedbrytningsprocessen kan vara nödvändig för att förstå energi- och laddningsöverföringar inom molekylen. Denna insikt skulle sedan kunna användas för att förstå mer komplexa system.

”Big Data” är en av vår tids största utmaningar. Ständiga förbättringar av såväl mätinstrument som mätmetoder kommer leda till en förbättrad förståelse av de fysikaliska och kemiska processerna i viktiga biomolekyler. Detta skulle kunna leda till innovation inom bioteknik, medicin, livsmedel, energiproduktion och kemiindustri utan dess like. En av vår tids största utmaningar för att uppnå detta är att hantera och effektivt analysera enorma mängder information. Dock gör forskningssamhället såväl som andra aktörer ständigt framsteg med att övervinna denna utmaning.

Abbreviations

ASG	Advanced Study Group
APT	Attosecond Pulse Train
CAMP	CFEL - ASG Multi-Purpose
CCD	Charge-Coupled Device
CFEL	Center for Free-Electron Laser Science
CPA	Chirped Pulse Amplification
DFT	Density Functional Theory
DM	Deformable Mirror
DVMIS	Double-sided Velocity Map Imaging Spectrometer
FEL	Free-Electron Laser
FLASH	Free-electron LASer in Hamburg
FWHM	Full Width at Half Maximum
HHG	High-order Harmonic Generation
IR	Infrared
MC	Monte Carlo
MCP	Micro-Channel Plate
PES	Potential Energy Surface
RMS	Root-Mean-Square
SASE	Self-Amplified Spontaneous Emission
SFA	Strong Field Approximation
TDSE	Time-Dependent Schrödinger Equation
TOF	Time-of-flight
UV	Ultraviolet
XUV	Extreme ultraviolet

Thesis

1 Introduction

According to Max Born and Robert Oppenheimer, molecular dynamics can be quantum mechanically separated into nuclear and electronic dynamics [1]. Although these are not necessarily independent, electronic transitions occur on extremely short timescales, while the much heavier nuclei follow more slowly. The observation of molecular photodissociation after the absorption of only a single photon led to the formulation of the Franck-Condon principle in 1926 [2]. After the electronic excitation caused by the absorption of the photon, which happens seemingly instantaneous, the equilibrium position of the nuclear potential is shifted, leaving the molecule vibrationally excited. If this excitation exceeds the dissociation energy, photodissociation can occur. The Franck-Condon principle, illustrated in Fig. 1.1, expresses the fundamental difference in timescale between electronic dynamics and nuclear motion. Electronic transitions are more likely if they do not involve changes in the positions of the nuclei, and thus vibrationally excited states may be favored. When the (binding) energy is plotted against the nuclear distance, as in Fig. 1.1, the Franck-Condon principle is expressed by “vertical” electronic transitions, without any change in nuclear coordinate. While the electronic structure of a molecule can change on the timescale of attoseconds to few femtoseconds (fs) [3], the response of the nuclei is on the many femtosecond or the picosecond (ps) scale [4].

The rearrangement of nuclear positions, mentioned above, which is effectively a change in bond length, also occurs in chemical reactions. This can lead to bond breaking and dissociation processes followed by fragmentation into neutral or charged fragments. These processes can be associated with hydrogen transfers or charge and energy transfers in general, which occur on a faster timescale. Conventional devices such as fast (camera/detector) shutters or electronics are not suitable to investigate these ultrafast processes. An alternative approach is to use ultrashort flashes of light that freeze the molecular motion by illuminating it for only a brief period, similar to a stroboscope, removing the need for a fast shutter. In the case of nuclear motion, femtosecond light pulses are required, which is possible

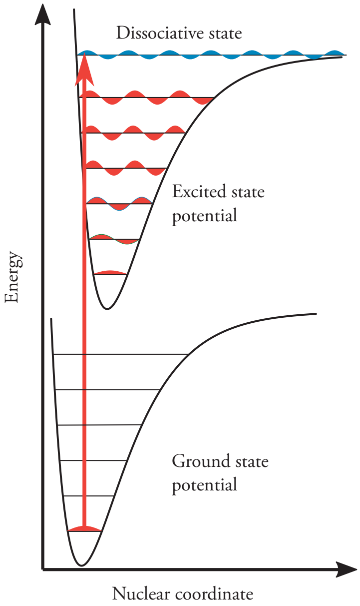

Figure 1.1: Illustration of the Franck-Condon principle.

with modern infrared (IR) laser systems, thanks to the development of mode-locking in 1964 [5, 6] and chirped pulse amplification (CPA) in 1985 [7]. However, these light pulses are often not sufficiently short for the investigation of electronic dynamics. The laser oscillation period, $T = \lambda/c$, defines the ultimate lower limit of the pulse duration, which is on the order of 3 fs for IR lasers [8]. Producing pulses on the attosecond timescale requires extreme ultraviolet (XUV) to X-ray wavelengths and was first reported on in 2001 [9, 10, 11].

Two kinds of XUV light sources, capable of producing ultrashort pulses, became available in the recent past: free-electron lasers (FELs) and high-order harmonic generation (HHG). Although the concepts of X-ray and XUV FELs, were proposed as early as 1971 [12], they only became available to users in 2005 [13]. Many FEL facilities have opened since then, but the pulse duration is limited to a few tens of femtoseconds, although FELs with pulse durations as short as 2 fs are planned [14]. Since the first reports of HHG in the late 1980s [15, 16], HHG has become established as a tabletop light source capable of delivering attosecond light pulses in the XUV and soft-X-ray regimes [9, 10]. The availability of these light sources enables the investigation of molecular dynamics, not only on the timescale of the nuclei, but also on that of the electrons.

1.1 Aim of the work

Two intense XUV light sources were used in this work: the free-electron laser in Hamburg (FLASH) [17], and the high-order harmonic generation-based High-Intensity XUV Beamline in Lund [18]. The aim of the work presented in this thesis was to develop and apply experimental and analytical methods to investigate molecular dynamics in combination with high-intensity XUV light sources. Irradiating molecules with XUV light pulses usually leads to photoionization and the molecules subsequently undergo rearrangement or fragmentation processes. These processes can be studied by observing the photoions and photoelectrons produced, and in particular their momenta or their yield depending on their mass/charge ratios (m/q).

The articles this thesis is based on can be divided into three categories:

- **Covariance mapping of photoions and photoelectrons at the High-Intensity XUV Beamline:**
  The implementation of a double-sided velocity map imaging spectrometer (DVMIS), presented in Paper V, in order to study photoion-photoion and photoelectron-photoion correlations in molecules via covariance mapping.

- **XUV metrology at the High-Intensity XUV Beamline:**
  Two-photon double ionization in neon was demonstrated with an XUV attosecond pulse train, reported in Paper I. The aberrations in the XUV wavefront introduced and compensated for by the XUV focusing optics were studied with a wavefront sensor, leading to the publication of Paper III. Further XUV and IR wavefront metrology was performed, leading to improved XUV wavefront quality and increased HHG yield (Paper VIII). The influence of the frequency and intensity dependent dipole phase on the focus and divergence of the generated harmonic generation is presented in Paper VII.

- **Time-resolved experiments on molecules at the free electron laser FLASH:**
  The study of UV-induced photodissociation of CH_2BrI is presented in Paper II. Similar dynamics were investigated in CH_3I and CH_2ClI and reported on in Paper VI. The transistion from a bound molecule to an isolated iodine atom was observed in CH_3I, leading to Paper IV.

1.2 Outline of the Thesis

Chapter 2 describes experimental techniques like pump-probe spectroscopy, high-order harmonic generation and velocity map imaging. Also described in Chapter 2, are the two used XUV light sources: the FLASH FEL and the High-Intensity XUV beamline. In Chapter 3, the coincidence and covariance methods are introduced. Covariance mapping is described in details. In Chapter 4 the experimental results, first at the High-Intensity XUV beamline (Papers I, III, V, VII and VIII) and then at the FLASH free-electron laser (Papers II, IV and VI), are presented. The work is summarized in Chapter 5 and an outlook on future developments and planned experiments is given.

2 XUV Light Sources and Experimental Techniques

This chapter descibes the experimental techniques and the XUV light sources used in this work. First, a brief inroduction to pump-probe spectroscopy is given. This technique was used at the free-electron laser facility FLASH in Hamburg. The general principle of free electron lasers is introduced next, followed by a description of the CAMP (Center for free-electron laser science - Advanced study group Multi-Purpose) endstation at the FLASH facility. However, most of the experimental work was carried out with a tabletop XUV light source based on HHG. The HHG process is outlined in detail, including the three-step model, the intensity dependence of the dipole phase leading to the spatio-temporal coupling presented in Paper VII, phase matching considerations and scaling (up) of the generation process. An example of the application in upscaled HHG is the High-Intensity XUV Beamline in Lund, which is described next. This beamline features a DVMIS for the simultaneous detection of photoions and photoelectrons, which is presented in Paper V. The principle of velocity mapping is introduced, simulations for the estimation of energy resolution are discussed as well as the implementation of the DVMIS.

2.1 Pump-Probe Spectroscopy

Conventional detectors and cameras are not able to detect ultrashort dynamics, even in the picosecond regime, so the underlying idea of ultrafast optics is to use very short laser pulses, usually on the femtosecond timescale, to "freeze" the motion of atoms and molecules. A single light pulse creates a snapshot of the state of the target at the moment of interaction, which can then be recorded with these detectors, since the short light pulse acts as a very fast camera shutter.

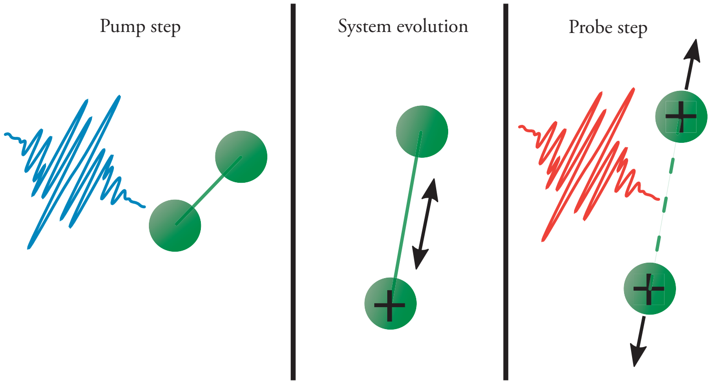

Figure 2.1: Sketch of the principle of pump-probe spectroscopy. In this example, a diatomic molecule absorbs a photon in the pump step. This causes ionization of the molecule, leaving a positive charge on the lower atom of the molecule, leading to rearrangement of the electronic structure. This may be accompanied by, e.g., bond stretching and the excitation of vibrational modes. In the probe step, the molecule in this example is ionized a second time, and the other positive charge is located on the upper atom. This leads to breaking of the bond, and both ionic fragments can be detected.

The introduction of a second light pulse with a precisely controlled variable delay with respect to the first one, provides more possibilities. The first pulse can be used to pump the system and initiate a dynamic response that can then be probed by the second pulse after a certain delay, as shown in the sketch in Fig. 2.1. Scanning over a range of delays around the temporal overlap of the pulses, allows these snapshots to be combined into a movie, revealing the dynamics of the system, such as the lifetime of the pumped states, bond breaking times, and transition rates in chemical reactions [4].

As an example of a time-resolved experiment, some results from Paper IV are shown in Fig. 2.2. In this experiment, carried out at FLASH, a photodissociation process was initiated in mehtyliodine (CH_3I) molecules by absorption of a 272 nm UV photon. This process is caused by C-I bond cleavage and leads to fragmentation into neutral CH_3 and neutral iodine. This process was then probed with a soft X-ray pulse with 11.6 nm wavelength, close to the resonance of the iodine 4d orbital, leading to mulitple photoionization and subsequent Coulomb explosion. The iodine 4d orbital undergoes a chemical shift from 58.3 eV to 57.3 eV when the atom is bound in a molecule. In the experiment, the binding

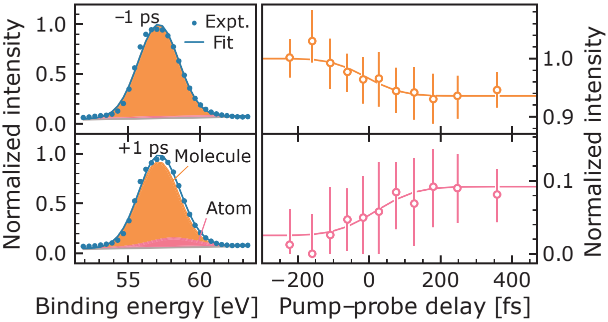

Figure 2.2: Time-resolved data from an XUV-IR pump probe experiment on methyliodine carried out at FLASH. The time-dependent behavior of the chemical shift of iodine 4d orbital was observed. (Adapted from Paper IV.)

energy of the released photoelectrons was determined for varying delays and the yield analyzed around the iodine 4d peak. For negative delays between the light pulses, where the photodissociation was not started before the ionization, the recorded photoelectrons originated purely from bound molecules. For increasingly positive delays however, an atomic distribution appears and its yield increases the more the photodissociation is progressed, displayed on the right half of Fig. 2.2. This way, the transition from the bound molecule to atomic iodine could be observed on a femtosecond timescale. More details from this and other time-resolved experiments carried out at FLASH, leading to the publication of the Papers II, IV and VI, can be found in Section 4.3.

2.2 Free Electron Lasers

An FEL is a light source based on the emission of radiation from electrons at relativistic velocities that are undulating in spatially alternating magnetic fields. FELs are currently available from the microwave region [19] up to the X-ray region [14]. Since only the XUV to X-ray range is of importance for this work, this section will focus on the devices and facilities delivering radiation in this range. The first scientific user studies at the FLASH facility started in 2005 [13, 20], providing radiation in the XUV to soft X-ray regime. The first hard X-ray FEL facility is the Linac Coherent Light Source (LCLS) at the SLAC National Accelerator Laboratory in Stanford (USA), which became available to users in 2009 [21]. Other FELs operating in the XUV-X-ray regime are: the Spring-8 Angstrom Compact free electron laser (SACLA) in Japan, operating in the hard X-ray regime [22], and the Fermi FEL at the Elettra Sincrotrone Trieste in Italy, with FEL-1 in the XUV range [23] and FEL-2 in the soft X-ray range [24]. Planned FELs include European X-FEL (Hamburg) [25], the Korean X-FEL [26], the Swiss X-FEL [27], and LCLS-II in Stanford [28].

Compared to other XUV and X-ray sources, the light generated by FELs is characterized by its unparalleled brilliance. Brilliance is expressed as the number of photons per second, per unit angle, per unit area in a 0.1 % bandwidth. While conventional X-ray tubes have brilliances around 10^8 to 10^{10} and first and second-generation synchrotron light sources using bending magnets have a brilliance of about 10^{15}, light sources using undulating magnets, such as modern synchrotrons and FELs, can reach a peak brilliance of 10^{20} (third generation) or even above 10^{30} (fourth generation) [29, 30, 31]. This enables experiments to be performed in the XUV and X-ray regime that were previously only feasible in photon energy regimes where laser-based light sources were available, like for example femtosecond pump-probe spectroscopy [32], coherent diffraction imaging [33, 34], and multiphoton ionization experiments [35].

In this section, the general principles of XUV/X-ray FELs based on the self-amplified spontaneous emission process will be introduced, after which the CAMP endstation at the FLASH facility, at which the experiments presented in Papers II, IV, VI and IX were carried out, will be described.

2.2.1 General principle

A schematic of an FEL is shown in Fig. 2.3. In the first step, free electrons are driven through a linear accelerator, reaching relativistic speeds with kinetic energies up to several GeV. The relativistic electrons then propagate through undulator stages, where they are forced into transverse motion by (spatially) periodically alternating magnetic fields. This causes the emission of synchrotron radiation in a forward cone. The periodic magnetic field

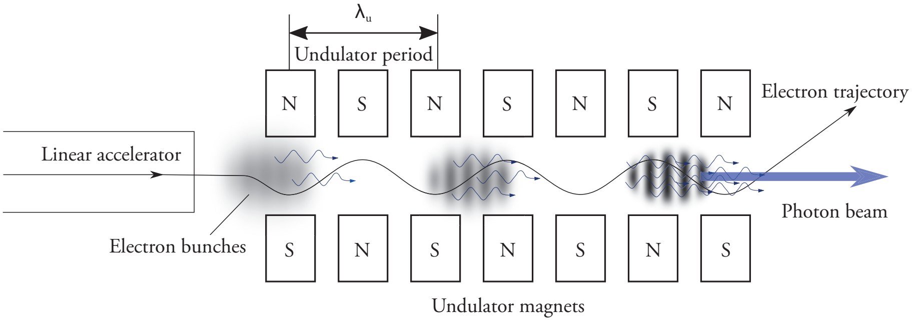

Figure 2.3: Schematic illustrating the principle of SASE-based FEL. The electrons are generated in bunches by a pulsed source and are accelerated to relativistic velocities before they arrive at the undulator, where they are forced into a transverse motion by the periodic magnetic field. Synchrotron radiation is emitted in a forward cone as a result of the acceleration, caused by the Lorentz force in the magnetic field. The electron density in the bunches is altered periodically (microbunching) due to the interaction with the electric field of the emitted radiation. This leads to amplification of the emitted radiation, as the microbunched electrons emit in phase with the light field.

in the undulator leads to electron density modulation with a spatial periodicity close to the resonance wavelength of the undulator period. Since the electrons move at relativistic velocities, they can interact with the radiation emitted by the electron bunch before it moves away, which leads to periodic longitudinal variations in the electron density (microbunching). Subsequent emission of radiation by the microbunches will then be in phase, which will enhance the microbunching and increase the intensity of the emitted radiation. The amplification of the emitted radiation varies exponentially with the length of the undulator until saturation is reached. Saturation is reached, when no additional energy is transferred from the electron bunch to the radiation field, even with increasing undulator length. The typical undulator length in FELs is several tens of meters, exceeding 100 m for X-ray FELs. In this regime, gains on the order of 10^7 can be achieved [36]. As the initial emission of radiation is based on shot noise in the electron bunch, this process is called self-amplified spontaneous emission (SASE) [37, 38, 39, 40]. The wavelength of the emitted light depends the period and magnetic field of the undulator and the kinetic energy of the electrons. This allows for some tunability of the wavelength by adjusting the undulator period and gap.

2.2.2 The CAMP endstation at the FLASH facility

The FLASH FEL facility operates in the XUV to soft X-ray regime ($24 - 295$ eV) [20]. Peak brilliances of 10^{31} can be achieved and up to 10^{14} photons can be delivered in pulses with durations between 30 fs and 200 fs.

During the course of this work, five campaigns were carried out at Beamline 1 (BL1) at the FLASH1 FEL, which have so far resulted in three publications. Beamline 1 features a mul-

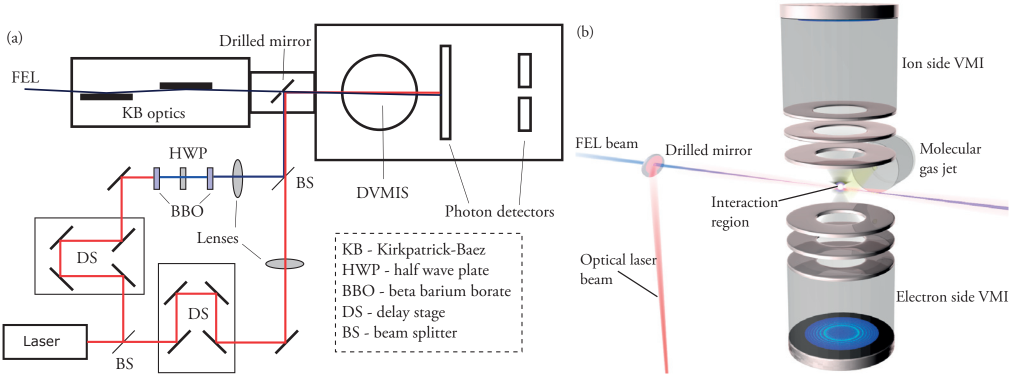

Figure 2.4: (a): Sketch of the layout of the CAMP endstation. The pump-probe laser setup is versatile. The fundamental 810 nm beam can be used directly, but the second and third harmonics (405 nm and 270 nm) can also be generated with the help of beta barium borate crystals and a half-wave plate. The fundamental and harmonic beams have separate beam paths and can be delayed independently, allowing not only FEL-laser pump-probe experiments, but also laser-laser pump-probe experiments. The laser beam(s) are then combined with the FEL beam via a drilled mirror. Both the laser and the FEL foci overlap the molecular gas jet in the interaction region of the DVMIS. The photoions and photoelectrons generated are then detected with the DVMIS. (b) Sketch of the beam combination and particle detection setup.

tipurpose CAMP endstation for ion and electron imaging, spectroscopy and pump-probe experiments. This endstation will be described in some detail in this section, providing complementary information to that given in Papers II, IV and VI. A more thorough description of the endstation has been given by Erk et al. [41].

The general layout of the beamline is shown in Fig. 2.4(a). Before the light beam from the FEL reaches the CAMP chamber, it is focused by two plane-elliptical Kirkpatrick-Baez mirrors [42] with a focal length of 810 mm horizontally (first mirror) and 550 mm vertically (second mirror). This results in a focal spot measuring 7 μm by 8 μm in the interaction region in the center of the CAMP chamber, providing focused intensities on the order of 10^{15} W/cm^2 at a photon energy of 92 eV (60 μJ, 90 fs). The gas phase samples are introduced to the interaction region via molecular jet gas sources based on supersonic expansion with several skimmer stages, such as the Even-Lavie valve [43, 44].

A 10 Hz repetition rate, 810 nm central wavelength, IR laser system (Ti:Sapphire) is available, which delivers 60 fs short pulses with 10 mJ pulse energy to the CAMP chamber. The IR laser is combined with the FEL beam via a drilled mirror, as shown in Fig. 2.4(b). The laser focus and delay can be moved separately so as to spatially and temporally overlap with the FEL pulse. Second (405 nm) and third (270 nm) harmonics of the IR laser, generated in beta barium borate crystals, are also available. An overall temporal resolution of 110 fs can be achieved with 70 fs FEL pulses. However it is a challenge to correct for the inherent jitter between the two light sources in the data analysis using shot-to-shot information from

(FEL) beam arrival time monitors and other peripheral diagnostic sensors on the beamline. Laser-FEL pump-probe experiments were performed using the third harmonic.

The CAMP chamber is very versatile and can be configured for a wide range of ion/electron imaging and spectroscopy experiments. The configuration used during the course of this work was the DVMIS configuration. In Fig. 2.4 the configuration with the DVMIS is illustrated. The charged particles are detected with multi-channel plates (MCP) in combination with phosphor screens and charge-coupled device (CCD) cameras.

2.3 High-order Harmonic Generation

HHG is a process that leads to the emission of XUV light and occurs when atoms are subjected to an external oscillating electric field with a strength on the same order of magnitude as internal atomic fields. Intensities in the range of $10^{14}\mathrm{W/cm^2}$ are readily available in the laser focus using CPA. At these intensities the internal atomic potential is considerably distorted, which leads to tunnel ionization. This phenomenon, and the dynamics of the tunneling electrons, have been studied thoroughly in the past [45, 46]. The quasi-free electrons are accelerated in the electric field of the laser and can be recaptured by the parent ion, while emitting XUV radiation [47]. The electromagnetic spectrum consists of high-order odd integer multiples of the fundamental laser field frequency [15, 16].

The first part of this section presents the fundamentals needed to describe the HHG process on a microscopic, atomic level, based on a semi-classical approximation. The three-step model, introduced by K. Schafer et al. [48] and P. Corkum [47], which models the single-atom response, is discussed, followed by, the cutoff-law [49], which predicts the highest photon energies achievable under given conditions is introduced. In the second part, the implications of the phase accumulated by the electrons during the HHG process, called the dipole phase, and its dependence on intensity is then discussed. The results given in Paper VII, in particular, provide some insight into this topic, and will be briefly presented here. HHG is then discussed from the macroscopic perspective as a collective effect of many atoms. In order to do this, the phase matching conditions in a typical gas phase medium assuming a Gaussian fundamental laser beam are examined. Additional considerations important in loose focusing geometries and the consequent implications for the upscaling of the harmonic generation process are discussed in the next section. Such a loose focusing geometry is used at the High-Intensity XUV Beamline at the Lund Laser Centre, where the experiments presented in Papers I, III, V, VII, and VIII were performed. This setup will be described in the last part of this section.

2.3.1 The three-step model

The three-step model and was first introduced in 1993/1994 [47, 48]. The atomic electric field binding the electrons is typically on the order of 10^{10} V/m. In a hydrogen atom ($Z = 1$), the field strength at a distance of 1 nm from the nucleus is about $1.4 \cdot 10^{9}$ V/m. The electric field of an 800 nm laser field with an intensity of 10^{15} W/cm^2 is $9 \cdot 10^{10}$ V/m. This leads to substantial distortion of the field experienced by a bound electron. Knowing the central light frequency, ω, and electric field amplitude, E_0, of the laser light, allows us to calculate the resulting potential, $V(x,t)$, for a given number of charges Z:

$$V(x,t) = -\frac{Z\mathrm{e}^2}{4\pi\epsilon_0 x} - \mathrm{e}xE_0\cos(\omega t), \tag{2.1}$$

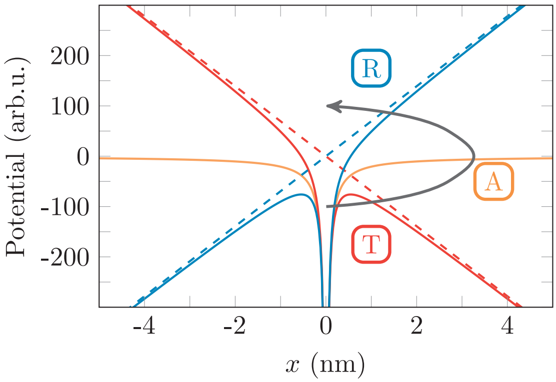

Figure 2.5: Illustration of the three-step model: The external electric field of the laser pulse distorts the atomic potential to such an extent, that one or more electrons can escape the potential via tunnel ionization, depicted in red (T). Once an electron escapes the atomic potential, it is accelerated in the laser field (orange, (A)). When the sign of the field flips, the electron is decelerated and its direction of motion is reversed. Under favorable conditions, the electron can recombine with the parent atom (blue, (R)), while emitting a photon. The energy of the photon corresponds to the energy imparted to the electron by the laser field plus the ionization potential of the atom.

where e is the elementary charge, and ϵ_0 the vacuum permitivity. This is illustrated for a set of realistic parameters ($\lambda = 800$ nm, $I = 10^{15}\mathrm{W/cm^2}$) in Fig. 2.5. The solid lines represent the total potential, while the dashed lines show the laser electric potential within a few nm of the atom. In the first step, depicted in red (T), the total potential decreases such that there is a finite probability of tunneling for the least bound electrons. In the case of a successful tunneling event, the free electron is accelerated in the oscillating laser field, shown in orange, (A). When the sign of the laser electric field flips, the force acting on the electron is reversed. Consequently, the electron will be decelerated, eventually turns around and is accelerated back towards the parent ion. Under some conditions, the electron will recombine with the atom and emit a photon in the process (blue, (R)). The photon energy depends on the kinetic energy, E_{kin}, acquired during the acceleration phase and the ionization potential, I_{p}.

In order to determine which photon energies can be achieved, and which conditions are favorable for HHG, the electron trajectories $x(t)$ must be investigated. In simplified analysis the atomic field is neglected once the electron is free. Thus, only the Coulomb force, F_{C}, of the laser field acts on the electron, and thus its acceleration is given by:

$$\ddot{x}(t) = -\frac{\mathrm{e}E_0}{m_e}\sin(\omega t), \tag{2.2}$$

where m_{e} is the electron mass. Integrating $\ddot{x}(t)$ over time twice, yields the displacement:

$$x(t) = \frac{\mathrm{e}E_0}{m_e\omega^2}[\sin(\omega t) - \sin(\omega t_{\mathrm{e}}) - \omega(t - t_{\mathrm{e}})\cos(\omega t_{\mathrm{e}})], \tag{2.3}$$

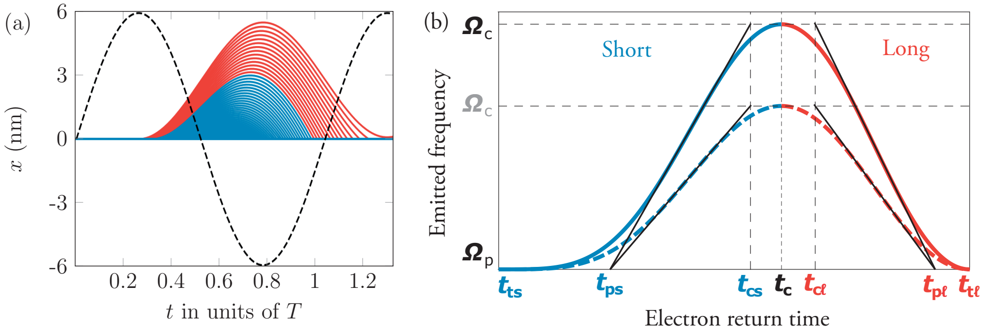

Figure 2.6: Calculation of electron trajectories that can lead to harmonic emission (a) and the corresponding frequencies Ω as a function of the electron return times (b). (a) The displacement of the electrons due to the external field (x) is plotted against the elapsed time in units of the period time (T) of an 800 nm laser field. The laser electric field is represented by the black dashed line. The successful trajectories can be divided into two categories: short (blue) and long (red), according to their time of excursion. (b) shows the emitted photon frequency as a function of electron return time. Short trajectories (blue) have earlier return times down to the threshold return time t_{ts}. The peak of the curve defines the cutoff time, t_{c}, and the cutoff frequency, Ω_{c}. Long trajectories (red) have later return times up to the threshold return time t_{tl}. The slopes can be approximated by piecewise straight lines $\Omega(t)$ originating at the modeled threshold times t_{ps} and t_{pl} and extending up to the modeled cutoff times t_{cs} and t_{cl}. The dashed curve shows similar results for a lower laser intensity. (b) was adapted from Paper VII.

where the emission time t_{e} is an important parameter. This is illustrated in Fig. 2.6(a), where the displacement, $x(t)$, of electrons with different emission times, t_{e}, is plotted. Only trajectories that lead the electron back to the atom are depicted. The laser electric field is superimposed as the black dashed line and the time axis is in units of the laser field period, T.

The kinetic energy can be derived from equations (2.2) and (2.3) and calculated according to:

$$E_{\mathrm{kin}} = 2U_{\mathrm{p}}[\cos(\omega t_{\mathrm{r}}) - \cos(\omega t_{\mathrm{e}})]^2, \tag{2.4}$$

$$U_{\mathrm{p}} = \frac{\mathrm{e}^2 E_0^2}{4m_e\omega^2}, \tag{2.5}$$

where t_{r} is the recombination time and U_{p} is the ponderomotive potential, which is the mean energy of the electron during the quiver motion in the oscillating field.

The maximum energy that can be accumulated this way is calculated to be $3.17U_{\mathrm{p}}$ and thus, taking the ionization potential, I_{p}, into consideration, the highest achievable photon energy upon recombination is:

$$E_{ph} = 3.17U_{\mathrm{p}} + I_{\mathrm{p}}, \tag{2.6}$$

also known as the cutoff law [49, 50]. The highest emitted light frequency Ω_{c}, called cutoff frequency is $(3.17U_{\mathrm{p}}+I_{\mathrm{p}})/\hbar$. Ω_p, corresponds to the ionization potential I_{p}: $\Omega_{\mathrm{p}} = I_{\mathrm{p}}/\hbar$.

The emitted frequency is plotted versus the electron return time in Fig. 2.6(b), which is reproduced from Paper VII. The trajectories are divided into shorter (blue) trajectories and longer (red) trajectories. This color coding also divides the plot into two regions. The emitted frequency has a distinct maximum at t_c (the cutoff time), which corresponds to the cutoff frequency, Ω_c. In this model, the lower frequency limit is the threshold frequency Ω_p. Trajectories with return times later than t_c are considered long, due to the longer excursion time of the electrons. While trajectories with earlier return times are called short.

As is evident from Fig. 2.6 (b), electrons with different kinetic energies (which thus generate different frequency components) have different excursion times, and consequently acquire different amounts of phase. This leads to the generation of chirped XUV pulses, known as the atto chirp, while the phase is referred to as the dipole phase [51, 52]. A pulse is chirped, when its instantaneous frequency (the temporal derivative of the phase) changes with time.

The dipole phase is intensity dependent, as the excursion time changes with the intensity of the driving field. This has been studied extensively [53, 54, 55, 56, 57], and the introduced group delay, t_i, for short ($i = \mathrm{s}$), and long ($i = \mathrm{l}$) trajectories depending on the generated frequency Ω, can be approximated by the slopes indicated in Fig. 2.6(b), (as motivated in Paper VII). This can be expressed as:

$$t_i(\Omega) = t_{pi} + \frac{t_{ci} - t_{pi}}{\Omega_c - \Omega_p}(\Omega - \Omega_p), \tag{2.7}$$

where t_{pi} is the threshold time in the linear approximation and t_{ci} is the cutoff time. The dipole phase is the indefinite integral of the group delay over $(\Omega - \Omega_p)$:

$$\Phi_i(\Omega) = \Phi_i(\Omega_p) + t_{pi}(\Omega - \Omega_p) + \frac{t_{ci} - t_{pi}}{\Omega_c - \Omega_p}\frac{(\Omega - \Omega_p)^2}{2}. \tag{2.8}$$

With $(\Omega_c - \Omega_p) = 3.17U_p/\hbar$, the fine structure constant α_FS, the speed of light c, and

$$\gamma_i = \frac{(t_{ci} - t_{pi})\pi \mathrm{c}^2 m_\mathrm{e}}{3.17\alpha_\mathrm{FS}\lambda^2} \tag{2.9}$$

the coefficient in the third term in Equation 2.8 can be rewritten as:

$$\frac{t_{ci} - t_{pi}}{\Omega_c - \Omega_p} = \frac{2\gamma_i}{I}. \tag{2.10}$$

The integration constant, which is the first term in Equation 2.8 is described in the strong field approximation (SFA) theory [50] by $\Phi_i = \alpha_i I$, and vanishes for the short trajectories, as $\alpha_s \approx 0$. The dipole phase can then be written:

$$\Phi_i(\Omega) = \alpha_i I + t_{pi}(\Omega - \Omega_p) + \frac{\gamma_i}{I}(\Omega - \Omega_p)^2. \tag{2.11}$$

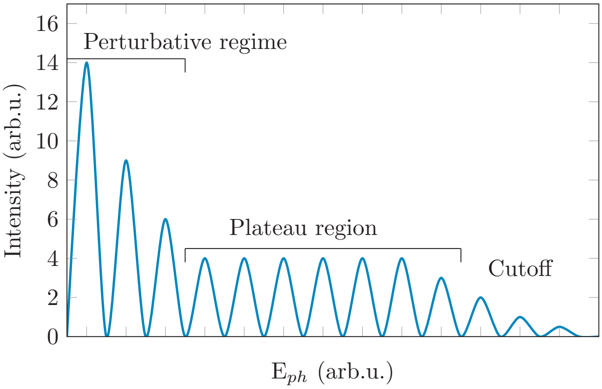

Figure 2.7: Illustration of a typical harmonic spectrum, exhibiting features such as the perturbative regime for the lower order harmonics, the plateau region and the cutoff.

This equation illustrates the intensity dependence of the dipole phase, which is important under experimental conditions, where the focus of the driving laser pulse will have an intensity distribution in space. This will be discussed in more detail in the next section.

The HHG process is repeated every half-cycle of the laser field. Due to the interference of waves emitted from consecutive half-cycles, which are phase-shifted by π, only odd order harmonics are expected in the spectrum (see Fig. 2.7). However, the single-atom response approach, does not take into account the fact that in an experiment many atoms, in relatively close vicinity to each other, will emit light waves. These waves will then interfere, and their phase relations play an important role. A more macroscopic view, considering HHG as a collective process involving an ensemble of many atoms will elucidate the effects of different phase contributions and their consequences.

2.3.2 Spatio-temporal coupling

A Gaussian optics model, combined with the analytical expression of the dipole phase in Equation 2.11, was used to investigate the importance of the frequency- and intensity-dependent dipole phase on the focus and divergence of the generated harmonic radiation (Paper VII). This model is valid for thin generation media.

The second term in Equation 2.11 is independent of intensity and will be omitted in the following of this discussion. A driving laser field with a Gaussian intensity profile $I(r, z)$ is assumed, where r is the radial coordinate and z the propagation direction. The laser focus is located at $z = 0$, while the generation position is described by the variable z (see Fig. 2.8). Furthermore, $w(z)$ is defined as the radial width at $1/\mathrm{e}^2$, $R(z)$ as the radius of curvature and I_0 as the peak intensity. At the focus, the waist is $w_0 = w(0)$. The phase of

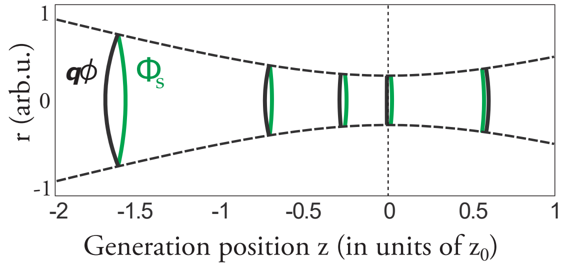

Figure 2.8: Contributions to the harmonic wavefront resulting from the fundamental wave (black) and the dipole phase (green). z_0 denotes the Rayleigh length of the fundamental beam. (Adapted from Paper VII.)

the q^{th} harmonic order field ($\Omega = q\omega$) can now be approximated by:

$$\Phi_q(r,z) = q\phi(r,z) + \Phi_i(r,z), \tag{2.12}$$

where $q\phi(r,z)$ is the phase of the fundamental field multiplied by q. Its influence on the HHG process will be further discussed in Section 2.3.3. The second term is the dipole phase, which, in the case of a Gaussian driving field is described by:

$$\Phi_i(r,z) = \frac{\alpha_i I_0 w_0^2}{w^2(z)} \mathrm{e}^{-\frac{2r^2}{w^2(z)}} + \frac{\gamma_i(\Omega-\Omega_p)^2 w^2(z)}{I_0 w_0^2} \mathrm{e}^{\frac{2r^2}{w^2(z)}}. \tag{2.13}$$

In Paper VII the radius of curvature $R(z)$ and the beam waist $w(z)$ of different harmonic orders are calculated and the consequences for focusing, like chromatic aberrations of the XUV beam, discussed. The results were compared to numerical calculations based on the time-dependent Schrödinger equation (TDSE) for single-atom response and propagation equations for the response from the generation medium [58]. The beam waist model predictions are also compared to experimental data taken at the High-Intensity XUV Beamline.

The predictions of the analytical model for the short trajectories are shown in Fig. 2.8. The wavefront induced by the dipole phase Φ_s is always divergent, independent of the position along the z-axis. The wavefront induced by the fundamental on the other hand changes from converging before the focus to diverging after it. Thus, the two contributions cancel out mostly before the focus and add up behind it.

Two main conclusions are presented in Paper VII. The First, is that the radius of curvature of the generated XUV beam will depend strongly on the location of the medium along the z-axis, and the second, is that not only do the trajectories have different divergences and source positions, but these quantities also vary with the harmonic order. The inset in Fig. 2.9 shows the focal positions and divergences for a range of harmonic orders of an 800 nm driving field around the fundamental focus with a generation medium placed before this focus.

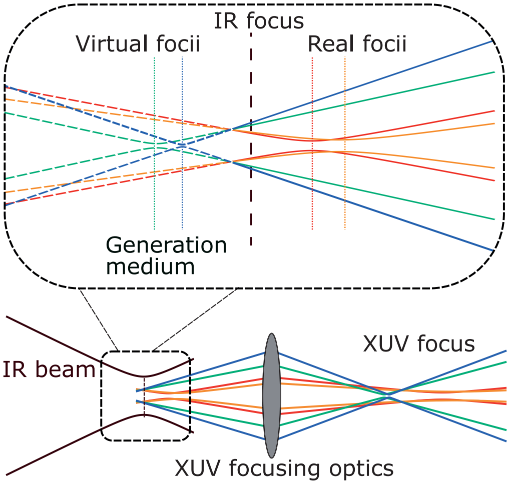

Figure 2.9: Spatio-temporal coupling in the generation of harmonic orders 25 (orange), 31 (red), 59 (turquoise) and 67 (blue). The IR focus is located close behind the thin sheet medium. The inset shows a magnification of the generation region where the different divergences and wavefront curvatures can be seen. The wavefront curvature and divergence of the harmonic beams vary considerably with frequency, leading to severe chromatic aberration and an extended focus (along z and r) after the XUV focusing optics. (Reproduced from Paper VII.)

A light pulse whose contributions have different divergences and source positions will exhibit chromatic aberration when focused. This behavior is shown in the lower part of Fig. 2.9. This might have significant repercussions in an experiment in which an XUV beam originating from HHG is to be focused.

To confirm the predictions of this model, the the dependence of the divergence and focal position on the generation position with respect to the focus of certain harmonics was further investigated. The model based on equation 2.13 and the numerical TDSE calculations were used and compared. The divergence results were then compared to spectrally-resolved data taken at the High-Intensity XUV Beamline. The beam width of several different harmonic order contributions was recorded, and the fundamental focus position was varied with respect to the gas cell containing the generation medium. Good agreements between the models and the experimental data were obtained.

Considering the importance of the XUV focal spot conditions especially in multiphoton experiments, the differences in focal spot size and focal position for different harmonic orders should not be neglected. Although it was not possible to observe these directly at the High-Intensity XUV Beamline, XUV wavefront measurements showed significant differences when comparing harmonics in the plateau region to those in the cutoff. The results of these wavefront measurements are published Papers III and VIII, and presented in Section 4.2.2, where the XUV focus in particular is studied and in Section 4.2.3, where the wavefronts of different harmonic orders are considered independently.

2.3.3 Phase matching

Phase matching is important in light-matter interactions when secondary waves are generated by several emitters that are distributed in a volume [50, 59, 60]. Seen from a point in the far field, waves from different emitters only interfere constructively if their phases are matched. This can be expressed by requiring that the wave vector mismatch, $\Delta\mathbf{k}$, between the fundamental light wave, with wave vector, $\mathbf{k}$, and the generated light wave is equal to zero [61]. In the case of generation of the q^{th} harmonic, with the wave vector of harmonic order q, $\mathbf{k}_q$, the wave vector mismatch is defined by:

$$\Delta\mathbf{k}(q) = q\mathbf{k} - \mathbf{k}_q. \tag{2.14}$$

The common experimental configuration for HHG employs a strong ($\mathrm{I} \sim 10^{14}\mathrm{W/cm^2}$), usually IR, fundamental laser beam with a Gaussian beam profile, that is focused into a gas jet or gas cell, and interacts with the gas atoms, as described in the previous two sections. For a harmonic field of order q, four main contributions to the wave vector mismatch can be identified [62, 63]:

$$\Delta\mathbf{k} = \Delta\mathbf{k}_G + \Delta\mathbf{k}_d + \Delta\mathbf{k}_n + \Delta\mathbf{k}_p. \tag{2.15}$$

For the rest of the discussion a laser beam with a Gaussian profile propagating along the z-axis is assumed, thus the vector notation will be omitted for simplicity. Such a Gaussian beam acquires a phase difference with respect to a planar wave, which is called the Gouy phase $\zeta(z)$. Δk_G denotes the gradient of the Gouy phase and has a negative sign. The on-axis Gouy phase gradient can be expressed in terms of Rayleigh length, z_R, by:

$$\Delta k_G = -\frac{q}{z_\mathrm{R}}. \tag{2.16}$$

The phase accumulated during the excursion of the electron, described in detail in the previous section, is the dipole phase. Applying the derivative with respect to z to Equation 2.11 yields:

$$\Delta k_d = \frac{\partial \Phi_i(\Omega)}{\partial z} = \alpha_i \frac{\partial I}{\partial z} - \frac{\gamma}{I^2}\frac{\partial I}{\partial z}(\Omega - \Omega_p)^2. \tag{2.17}$$

For the short trajectories ($i = \mathrm{s}$), α_s vanishes. The resulting wave vector mismatch, Δk_d, is generally negative for atoms located before the focus (z<0) and positive for those behind the focus (z>0).

The third term in Equation (2.15), Δk_n, is caused by neutral dispersion of the gas medium. Since the refractive index of the gas medium is generally higher for the fundamental field than for the harmonic fields, this contribution has a positive sign:

$$\Delta k_n = q\frac{\omega}{c}(n_1 - n_q). \tag{2.18}$$

Due to the high intensities in the laser focus, a considerable number of free electrons are produced, forming a plasma. The refractive index of the plasma, n_q^e, can be expressed in terms of the free-electron density, N_e, and the critical electron density, $N_c(\omega)$, which is the density above which a plasma becomes opaque, as $n_q^e = \sqrt{1 - N_e/N_c}$. This leads to the plasma dispersion term, Δk_p, which has a negative sign:

$$\Delta k_p = q\frac{\omega}{c}(n_1^e - n_q^e). \tag{2.19}$$

These four terms depend on experimental parameters such as the laser pulse energy, focusing conditions, gas pressure and focal spot position with respect to the gas target. Although perfect phase matching ($\Delta k = 0$) is not realistic under experimental conditions, varying the experimental parameters in order to compensate for the contributions from Equation (2.15) can yield adequate phase matching over the interaction volume.

2.3.4 Scaling of the HHG process

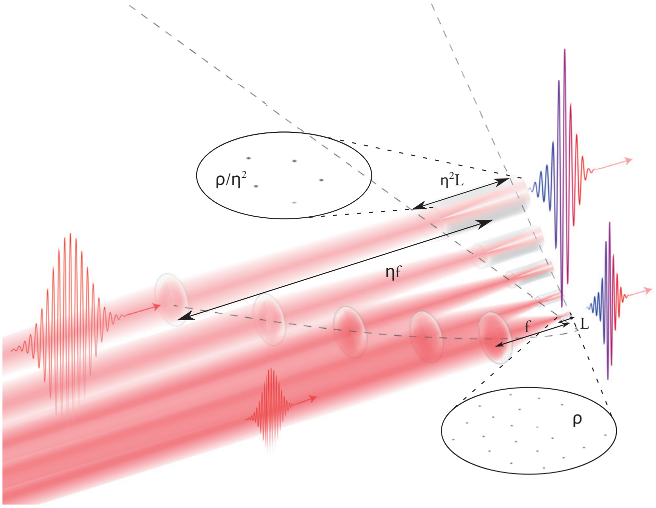

Figure 2.10: Illustration of the scale invariance of the HHG process. The lowest laser beam represents the unscaled process with gas density ρ, focal length f and gas medium length L. The size of the laser pulse represents the input pulse energy $\mathrm{E_{in}}$. The laser beam with the increased laser pulse size represents an increased input pulse energy $\eta^2\mathrm{E_{in}}$ with scaled parameters ρ/η^2, ηf and $\eta^2 L$. The conversion efficiency of the process is unaffected ($\Gamma \rightarrow \Gamma$), thus the output pulse energy scales with the input energy ($\mathrm{E_{out}} \rightarrow \eta^2\mathrm{E_{out}}$). (Image courtesy of C. Heyl.)

The scalability of nonlinear processes in gases has recently been demonstrated [64]. A scaling model based on a nonlinear wave equation in frequency (ω) representation and a paraxial approximation, known as the forward Maxwell equation [65] was introduced. Conclusions were drawn on the scalability of the parameters after transformation of the wave equation from the laboratory frame to a frame moving at the speed of light. This model was then applied to nonlinear phenomena, one of them being HHG. An especially remarkable result was the scale invariance of the HHG conversion efficiency, Γ, under scaling of the input pulse energy ($\mathrm{E_{in}} \rightarrow \eta^2\mathrm{E_{in}}$), since the output pulse energy scales equally ($\mathrm{E_{out}} \rightarrow \eta^2\mathrm{E_{out}}$). This invariance requires that experimental parameters such as the gas density, ρ, focal length, f, and gas medium length, L, are scaled accordingly ($\rho \rightarrow \rho/\eta^2$, $f \rightarrow \eta f$, $L \rightarrow \eta^2 L$).

An illustration of the scale invariance of the HHG process is shown in Fig. 2.10. Conversion efficiencies (Γ) on the order of 10^{-5} have been reported under "typical" HHG conditions [66]. In this experiment 40 fs short pulses with 1.5 mJ pulse energy ($\mathrm{E_{in}}$), and 800 nm wavelength were used at a repetition rate of 1 kHz. Under these conditions an output energy of $\mathrm{E_{out}} = 15$ nJ was achieved (corresponding to $\Gamma = 10^{-5}$) at a generation gas pressure of 15 mbar in a xenon gas jet, with a typical absorption length of $L = 1$ mm. Constant temperature is assumed under experimental conditions, allowing the simplification $p \propto \rho$, thus enabling control of the gas density, ρ, by the gas pressure, p. This scenario corresponds to the lower part of the illustration in Fig. 2.10, with the unscaled parameters (L, f, ρ and $\mathrm{E_{in}}$).

If the proposed scaling principle is now applied to these parameters ($L \rightarrow \eta^2 L$, $f \rightarrow \eta f$, $\rho \rightarrow \rho/\eta^2$, $\mathrm{E_{in}} \rightarrow \eta^2\mathrm{E_{in}}$), with the aim of increasing the output pulse energy, modern high power laser systems delivering hundreds of mJ pulse energy come to mind. The remaining laser parameters can readily be equivalent in these laser systems (40 fs, 800 nm, and the repetition rate can be omitted in this discussion). When using an input pulse energy of 100 mJ, it should be possible to achieve output powers of approximately $\mathrm{E_{out}} = 1$ μJ (retaining $\Gamma = 10^{-5}$). In order to facilitate this, the generation parameters must be scaled appropriately ($\eta = 8.2$), corresponding to the upper part of the illustration in Fig. 2.10. The scaled parameters are then: $f = 8.2$ m, $p = 0.2$ mbar, and $L = 67$ mm.

The prospect of the generation of 1 μJ XUV pulses led to the development of the High-Intensity XUV Beamline, which is described in more detail in Section 2.4. The successful generation of XUV pulses in this regime was demonstrated in 2013 [18], and in Paper I. Several other labs have developed HHG-based sources taking advantage of the up-scalability of the output pulse energy by scaling up the generation geometry [67, 68, 69, 70], and up-scaling on an even grander scale is planned at the ELI Extreme Light Infrastructure in Szeged, Hungary [71]. Scaling in the other direction, towards more compact HHG light sources, driven by low-energy per per pulse, high-repetition rate laser systems, has also been successfully demonstrated [72].

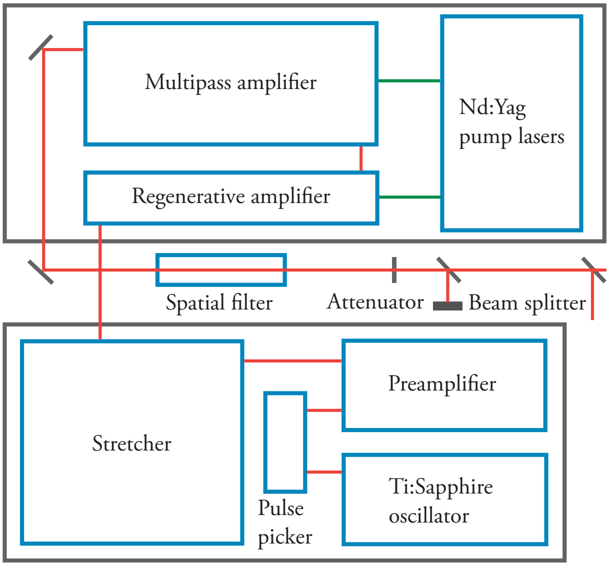

Figure 2.11: Sketch of the TW laser system at the Lund Laser Centre. The CPA-based system provides 200 mJ pulse energy, 300 ps pulse duration, 800 nm wavelength IR pulses to the High-Intensity XUV Beamline at a repetition rate of 10 Hz.

2.4 The High-Intensity XUV Beamline in Lund

The High-Intensity XUV Beamline in Lund was developed with the goal of generating μJ XUV pulses making use of the scale invariance of the HHG process, as described before. A loose focusing scheme is employed with up to 8.7 m focal length, 90 mJ IR pulse energy on target and below mbar pressure in a 6 cm long gas cell, achieving up to 1 μJ XUV pulse energies after generation. This has enabled studies involving two-photon processes such as that presented in Paper I. In this section, the High-Intensity XUV Beamline will be described, at which the experiments described in Papers I, III,V, VII and VIII were carried out.

The beamline is driven by a CPA-based TW laser system, which is illustrated in Fig. 2.11. A 80 MHz passively mode-locked oscillator with a Ti:Sapphire crystal generates 800 nm central wavelength laser light with a bandwidth of 50 nm. The repetition rate is then reduced by a pulse picker to 10 Hz, and preamplified to avoid the amplification of spontaneous emission. The pulses are then temporally stretched to about 300 ps as the first step in the CPA process. The stretched pulses are amplified in a a regenerative amplifier and a multipass amplifier (pumped by two Nd:YAG lasers) to a pulse energy of 400 mJ. The spatial profile is then cleaned by sending the beam through a telescope with no magnification, where a conical pinhole with a 400 μm diameter is positioned at the common focus of the lenses. About 200 mJ is then split off towards the High-Intensity XUV Beamline, where the pulses

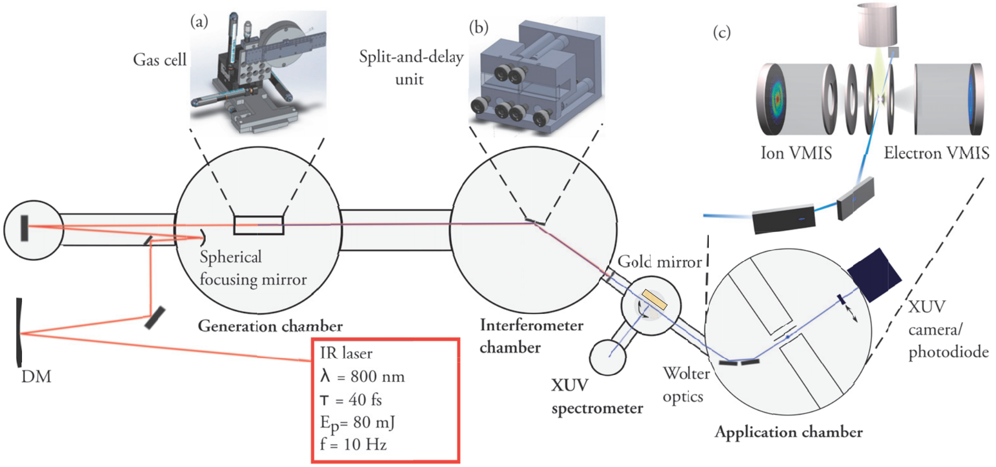

Figure 2.12: Schematic of the High-Intensity XUV Beamline setup. The IR laser pulses delivered by the TW laser system (illustrated in Fig. 2.11) are compressed to 40 fs. The laser beam is then focused into the generation chamber by a spherical mirror in combination with a deformable mirror (DM). XUV light is generated via HHG in the generation gas cell (shown in inset (a)). The beams are deflected by a silica plate in the interferometer chamber. Alternatively, the wavefront can be split by a split-and-delay unit (b) for XUV-XUV pump-probe experiments. A 200 nm aluminum filter eliminates the remaining IR light, before the XUV beam is sent to a spectrometer by a rotatable gold mirror. If the gold mirror is rotated out, the XUV beam arrives in the application chamber, where it is focused into the interaction region of the DVMIS (c). Behind the focus, the intensity fluctuation can be monitored by an XUV photodiode and the beam profile and pulse energy measured with an XUV camera.

are recompressed to about 40 fs pulse duration as the last step in the CPA process. A typical spectrum is displayed in Fig. 2.13(a). If necessary, the pulse energy can be decreased via a polarization-based attenuator, in order to be able to control the intensity as a parameter in the HHG process. The pulse energies used in the experiments in the present work ranged between 30 mJ and 90 mJ. An active stabilization system with piezo-actuated mirrors and beam-monitoring cameras is employed to avoid drifts in pointing and positioning of the beam.

At the High-Intensity XUV Beamline a loose focusing scheme with variable focal length is employed to focus the infrared laser light provided by the TW laser system into a gas cell in a vacuum chamber, as depicted in Fig. 2.12(a). In the earlier experiments (see Papers I and V), a lens with a focal length of 8.7 m was used. An upgrade to a deformable mirror in combination with a spherical mirror allowed variable focal lengths of about 7.7 m to 8.5 m (see VII and VIII). A combination of the lens and the deformable mirror was used for the experiments presented in Paper III. The deformable mirror (AKA Optics) has a diameter of 70 mm and its surface consists of 32 elements that can be actuated. The beam diameter at this stage is 32 mm ($1/e^2$), but is then usually apertured with an iris to about 28 mm.

The XUV light generated and the fundamental beam co-propagate towards the interferometer chamber. An XUV split-and-delay unit (inset (b)) based on wavefront splitting and a XUV-IR Mach-Zehnder type interferometer for XUV-XUV and XUV-IR pump-probe experiments, were conceived, designed and implemented in parallel. For the experiments carried out during this work, the interferometers were replaced by two (Paper I) or one (Papers III, V, VII and VIII) (IR) anti-reflection coated fused silica plate(s) each with an XUV reflectivity of 65 % to attenuate the IR light and redirect the beams towards the diagnostics and application chambers.

A 200 nm thick aluminum filter was used to filter out the residual IR light. It cuts the XUV spectrum below the 11$^{\text{th}}$ harmonic, due to the plasma frequency at $\sim$ 15 eV and has a transmission of about 34 % for XUV light. A rotateable gold mirror can be introduced to reflect the beam towards a flat-field XUV spectrometer (Jobin-Yvon PGM-PGS 200). A typical recorded XUV spectrum from generation in argon is shown in Fig. 2.13(b). Here, the cutoff energy is at 47.7 eV corresponding to the 31$^{\text{th}}$ harmonic.

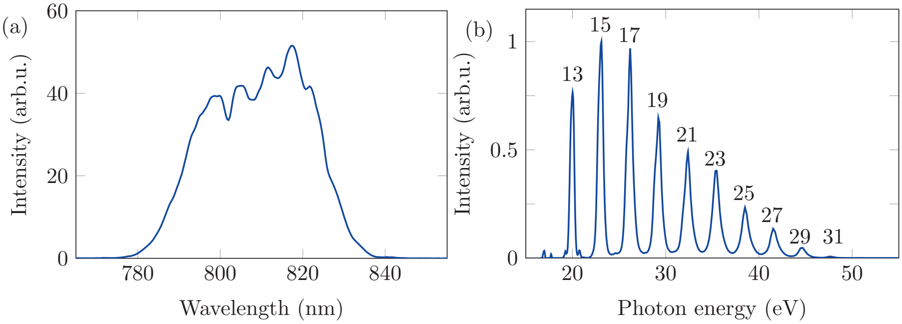

Figure 2.13: (a) Typical spectrum of the IR laser pulses delivered by the TW laser system. (b) XUV spectrum of high-order harmonics generated in argon.

The gold mirror in the diagnostics chamber can be rotated out of the beam path, allowing the beam to propagate into the application chamber. Here, two toroidal mirrors in a Wolter configuration [73], which minimizes coma aberration, are used to focus the XUV light down to a focal spot size of $3.6 \times 4.0\ \mu\text{m}^2$ full width at half maximum (FWHM) in the center of the chamber (Paper III). The mirrors are gold coated and have 46 % reflectivity for a grazing incidence angle of 15°. The atomic or molecular gas targets are introduced by a supersonic gas jet that intersects the XUV focus in the center of the chamber (as depicted in Fig. 2.12 (c)). An Even-Lavie solenoid valve mounted on top of the chamber with two skimmer stages, produces high density gas pulses with durations in the 10-30 μs range [43, 44]. The intense XUV pulses create photoions and photoelectrons upon interaction with the gas target. These charged particles and their (3D) momentum distributions are imaged in a DVMIS, which is discussed in more detail in section 2.5.

The charged particles in the DVMIS are detected with chevron type MCPs (Photonis) combined with phosphor screens, that are imaged with CCD cameras, with 1 megapixel resolution and a pixel depth of 8-16 bits (Allied Vision Pike F145). The ions generated can also be studied by recording their TOF spectrum, facilitated by decoupling the current from the MCP and acquisition with a fast digitizer (Agilent Acquiris). In order to monitor the shot-to-shot intensity fluctuations, an XUV photodiode (AXUV63HS1 from Opto Diode) can be introduced into the beam behind the focus, whose signal is also recorded with the digitizer. Furthermore, an XUV-CCD camera (Andor iKon-L) is located about 50 cm behind the interaction region and is routinely used to image the beam profile and measure pulse energies.

In order for the light and gas pulses to be present in the interaction region simultaneously, the gas jet valve opening must be triggered and synchronized with the laser arrival time. The same applies to the CCD cameras monitoring the phosphor screens of the DVMIS and the fast digitizer. For the purpose of covariance analysis (see in section 2.5.3), the acquisition of the velocity map images, the TOF signal and the photodiode signal must be synchronized on a single-shot basis and marked with timestamps. Over the course of this work, software and hardware solutions were implemented to facilitate the synchronization of data acquisition, storage and subsequent analysis. It should be noted that single-shot acquisition generates about 2 MB of raw data per laser shot, which can lead to substantial amounts of raw data considering the potential requirement of several 10 000s or even 100 000s of recorded shots for covariance analysis of a single dataset. To handle this, a lossless compression algorithm based on run-length encoding was implemented, achieving typical compression ratios of 1:40 on the acquired VMI data [74].

2.5 Velocity Map Imaging

The electrons and ions produced by photoionization or photodissociation are detected by using static electric or magnetic fields in order to accelerate them towards a detector. An instrument often used to detect photoions is the Wiley-McLaren TOF spectrometer, employing two stages of electrodes and a field-free flight tube. This allows the discrimination of ions based on their m/q and initial kinetic energy, while being independent of the position within the interaction volume with respect to the detector [75]. Flight times of photoelectrons can be recorded with magnetic bottle electron spectrometers, where an inhomogeneous magnetic field collects the photoelectrons from the interaction region and steers them towards a flight tube [76]. The spectral information obtained through these approaches allows the resolution of very fine structures, such as vibrational electronic states in molecules, and allows the analysis of correlations between the recorded channels, which may provide information on processes such as Coulomb-explosions or hydrogen transfer. However, it is often desirable to obtain more than just spectral information from the observed photoionization events. VMI is a way to obtain the momenta of the charged particles, and thus spectral information, with angular resolution in the detector plane [77]. In this section, the basic principles of VMI are described first, and charged particle trajectory simulations, that were carried out to characterize the DVMIS which was implemented during the course of this work, are described in the second part.

2.5.1 Basic principles of VMI

In a VMI spectrometer (VMIS), the charged particles are collected and accelerated towards a position sensitive detector by electrostatic lenses generated by several open electrodes. Angularly resolved momentum maps of the charged particles are recorded. However, the particle momenta recorded, are projections on the detector plane and thus contain information only on the transverse momentum, information on the longitudinal momentum being lost due to the strong electric fields, the detected particle momenta are independent of the location of the original photoionization event within the interaction region, as in the Wiley-McLaren TOF spectrometer.

A simple VMIS design, such as that shown in Fig. 2.14, consists of a repeller plate and an open extractor electrode that establish an electric field over the interaction region where the photoionization events occur. Between the extractor and the position-sensitive charged particle detector is a field-free flight tube then, as in a TOF spectrometer. The open geometry of the extractor electrode generates an electrostatic lens. The effect of this lens depends on the ratio between the repeller voltage V_{R} and the extractor voltage V_{E}, both with

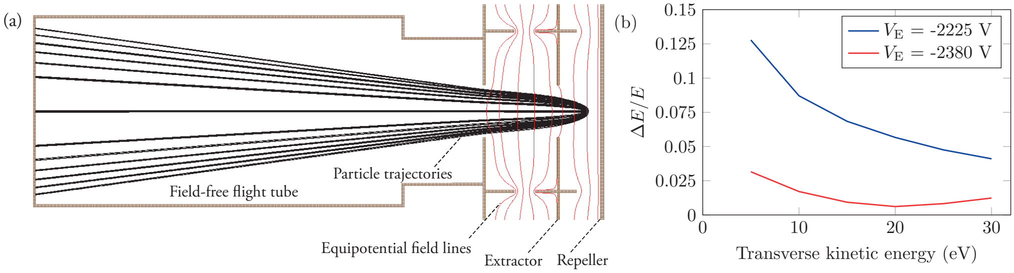

Figure 2.14: (a): A model VMIS electrode assembly showing equipotential field lines (red) illustrating the electrostatic lenses generated by the repeller and extractor electrodes. Electrons with several different kinetic energies were simulated and their trajectories in the fields calculated. Illustrations and simulations were produced using SIMION [78]. (b): Estimation of the spectral resolution for VMI mode extraction fields. The repeller voltage was set to -3000 V and the first guess of the extractor voltage was -2225 V. Simulations were performed with the 27 particle model, showing a spectral resolution between 5 and 10% (blue curve). Increasing the extractor voltage to -2380 V yielded a spectral resolution below 2.5 % (red curve).

respect to the flight tube voltage V_F, defined as:

$$\eta = \frac{V_\mathrm{E} - V_\mathrm{F}}{V_\mathrm{R} - V_\mathrm{F}}. \tag{2.20}$$

η affects the curvature of the field in the interaction and determines the imaging mode. In this section, the discussion will be limited to the VMI mode. Further details on other imaging modes can be found in Paper V and in [77].

In VMI mode, charged particles with the same m/q and transverse momentum will be imaged onto points at the same distance, R , from the center of the detector. Complete 3D momentum information can be retrieved through Abel inversion procedures provided cylindrical symmetry is ensured in the ionization process [79, 80].

2.5.2 Simulations of charged particle trajectories

Simulations of the trajectories of charged particles created in the electric fields generated around the electrodes can be carried out to evaluate the viability of a specific electrode design. This was done with the software SIMION [78], and the results for an electrode assembly with VMI voltages for electron imaging are illustrated in Fig. 2.14(a). For more realistic estimates of the resolution, comprehensive methods such as Monte Carlo (MC) simulations, that can calculate the trajectories of millions of particles, are required. However, these kinds of calculations are usually very time-consuming, and it is desirable to use a faster approach to test whether a certain voltage configuration is feasible. The so-called 27 particle model offers a practical, straightforward way of testing and estimating the energy resolution. In this approach, the trajectories of only 27 particles per kinetic energy step are calculated in order to estimate the energy resolution of the spectrometer in a specific voltage configuration. Since this can be done very quickly, various configurations can be simulated prior to investigating a specific set of voltages more thoroughly with MC simulations, or the voltages in an experiment can be adjusted in cases when, for example, a different kinetic energy range is required.

In an experiment where photoelectrons from ionization events are to be imaged, the maximum kinetic energy will determine the required amplitude of the electrode voltages. Faster electrons require higher voltages, to ensure that the distance to the detector axis is not greater than the openings in the electrodes, and they will hit the MCP detector. On the other hand, the energetic separation between electrons generated from, e.g., different states determines the energy resolution required. A good compromise is to choose the voltages such all photoelectrons generated can be detected, while their distribution is spread out as much as possible over the detector, while still in VMI mode. The 27-particle model is well-suited for this purpose and even provides an estimate of the resolution. This is done by defining a range of kinetic energies, for example, 5 eV to 30 eV, in steps of 5 eV, and placing 27 particles for each step in a defined interaction volume, where they are arranged on a $3 \times 3 \times 3$ grid.

The kinetic energy is expressed by assigning of momentum vectors in the plane parallel to the detector plane, ensuring that the complete momentum is always detected. Although this does not take into account the fact that particles with momentum vectors not parallel to the detector plane will be detected with momenta corresponding to a projection of their vectors onto this axis, lengthy inversion processes to retrieve the momentum distributions can be avoided and direct estimates of the energy resolution can thus be obtained. Such an estimation of the resolution estimation was made with for the VMIS assembly shown in Fig. 2.14(a) with voltages of -3000 V and -2250 V on the repeller and extractor, respectively.

The particles reaching the detector plane and the distance to the center of the detector recorded. The resulting distribution, (corresponding to their radii in a 2D image) for each kinetic energy is used to obtain estimates of the energy resolution, $\Delta E/E$. The results for electrons with kinetic energies from 5 to 30 eV are presented in Fig. 2.14(b) (blue). The calculated resolution of 5 to 10 % can be sufficient for some experiments, but usually a resolution around or below 2 % is desirable. Thus, the resolution was optimized, varying the extractor voltage, and a value of -2380 V gave a significantly better resolution (red curve in Fig. 2.14(b)), of less than 2 % for electron kinetic energies of 10 eV and higher. However, the 27 particle model should be considered as a tool for quickly identifying reasonably viable experimental conditions. Once a suitable set of voltages has been identified the configuration can be further investigated with an MC simulation [81].

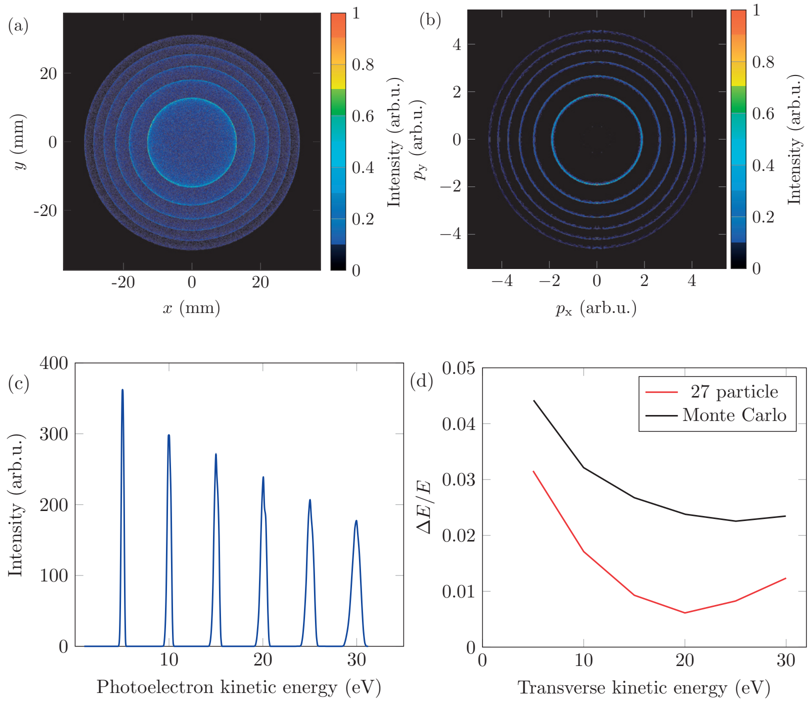

Figure 2.15: Results of Monte Carlo simulations of the example VMIS in Fig. 2.14. (a) The 2D momentum distribution of spawned electrons with kinetic energies between 5 and 30 eV. The corresponding retrieved Abel-inverted 3D momentum distribution is shown panel (b). The distribution was then angularly integrated and energy calibrated giving the spectrum shown in (c). The FWHM of Gaussian fits to the peaks in the spectrum is then used to calculate the simulated energy resolution, which is plotted in black in (d). The results of the 27 particle model, reproduced from Fig. 2.14, are shown for comparison (red curve). The simulations were performed using the SIMION software [78].

About 10^6 particles with kinetic energies from 5 eV to 30 eV and momentum vectors isotropically distributed over the whole solid angle, were placed in a Gaussian distribution over the interaction volume. As in the 27 particle model, the trajectories of the particles are simulated and their impact on the detector plane recorded. A 2D detector image is generated, as shown in Fig. 2.15(a). This image can then be Abel-inverted to obtain the complete 3D momentum distribution shown in Fig. 2.15(b). The retrieved momentum distribution is then calibrated using the known kinetic energies, and the energy resolution can be obtained from the FWHM of the Gaussian fits to the peaks in the spectrum shown in Fig. 2.15(c). The result is shown as the black curve in Fig. 2.15(d), and compared with the resolution estimated with the 27 particle model (red curve). The energy resolution obtained from the MC simulation is acceptable, being below 4 % for kinetic energies up to 10 eV and below 3 % above. As discussed in Paper V, the 27 particle model underestimates the resolution. Nevertheless this model seems to be reliable to find voltage for the optimization of the resolution in a specific kinetic energy range.

2.5.3 Double-sided Velocity Map Imaging Spectrometer

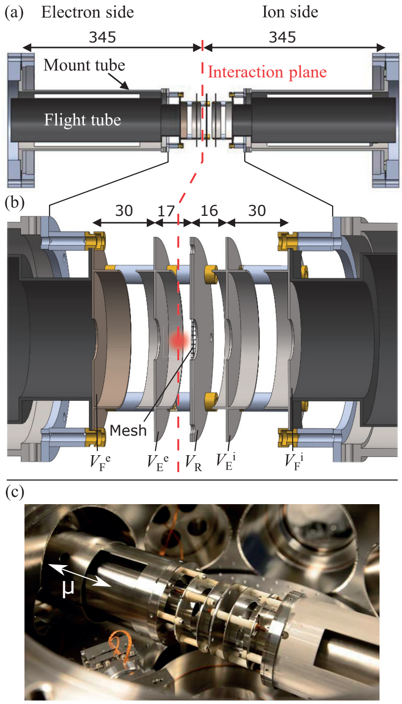

Figure 2.16: (a) A schematic section of the DVMIS along the detector axis. The flight tube and electrode assemblies are shown, as well as the mount tubes and flanges that attach the spectrometer to the vacuum chamber. A more detailed view of the electrode assembly is shown in (b). The repeller electrode, at voltage V_R and mesh are also shown. Extractor electrodes can be seen on either side of the repeller for extraction of electrons and ions (denoted V_E^e and V_E^i). The flight tubes (V_F^e and V_F^i) surrounded by the mount tubes are also shown, onto which the electrode assemblies are mounted. All distances in (a) and (b) are in mm. (c) A photograph of the DVMIS mounted inside the application chamber of the High-Intensity XUV Beamline. (Reproduced from Paper V.)

The standard VMIS design is very versatile and allows for the detection of electrons or ions, by reversing the polarity of the voltages applied to the electrodes. However, it is not straightforward to detect both photoelectrons and -ions simultaneously. Although, attempts have been made to accomplish this by fast switching of the extraction voltages, compromises must be made in the design, and sophisticated solutions are required in terms of electronics and camera exposure times [82, 83]. A different approach was taken at the High-Intensity XUV Beamline. After successfully implementing and commissioning a single-sided VMIS, the apparatus was extended by the addition of a second flight tube opposite the existing one. An additional open extractor electrode was also added, and a 20 mm diameter orifice was cut into the repeller electrode. In order to avoid penetration by electric fields from either side of the repeller plate, the hole was covered with a metallic mesh. The final assembly, which constitutes a DVMIS is illustrated in Fig. 2.16.

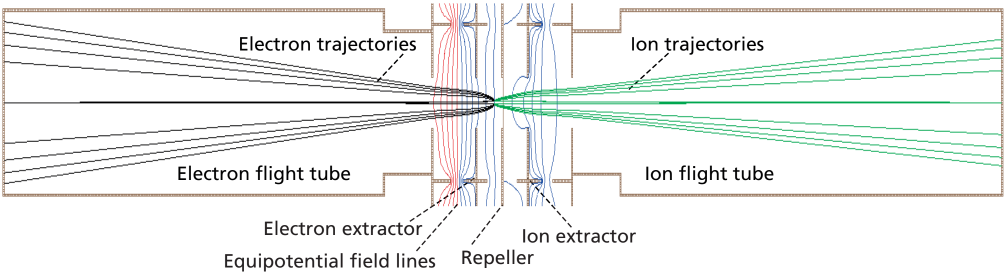

Figure 2.17: Schematic of a section through the DVMIS described in Paper V. The repeller plate has a mesh, that allows the photoions to be transmitted, but prevents electric fields from the ion side from penetrating into the electron side, and vice versa. The equipotential field lines for a typical ion and electron VMI configuration obtained using SIMION are shown: red representing positive potentials and blue negative potentials, with respect to ground potential. The electron and ion trajectories are shown in black and green, respectively.

The DVMIS was designed to have the ability to image photoelectrons with up to 90 eV kinetic energy, while also still recording ions with up to 10 eV kinetic energy. This determines the flight tube lengths, electrode hole diameters and applicable voltage limits. These and more design considerations are described in detail in Paper V.

A major challenge in the design of this spectrometer was to find a feasible configuration for the electrostatic lenses that allowed for simultaneous imaging of photoelectrons and -ions, essentially retaining the electron imaging resolution of a single sided VMIS without compromising the ion imaging capabilities.

To explore this option, particle trajectory simulations were carried out using the SIMION software. The assembly, with simulated particle trajectories and equipotential field lines, is depicted in Fig. 2.17. The behavior of the mesh was assumed to be ideal with zero electric field penetration and complete ion transmission. Several voltage configurations were simulated for the DVMIS used in this work. The results for the imaging mode with both ion and electron extraction fields configured in VMI mode are shown in Fig. 2.18. This voltage configuration was used as it provided optimal electron imaging resolution. Panel (a) shows the simulated VMI image generated from the particle impacts in SIMION. It exhibits 17 rings corresponding to the selected kinetic energies between 10 and 90 eV. The image was then Abel-inverted leading to the result shown in panel (b). This figure shows series of sharp rings, that can be angularly integrated and calibrated to obtain the kinetic energy spectrum shown in panel (c), together with the results of simulations for different extractor voltages using the 27 particle model for comparison. The widths (FWHM) of the peaks were estimated using Gaussian fits and the energy resolution calculated. The resulting

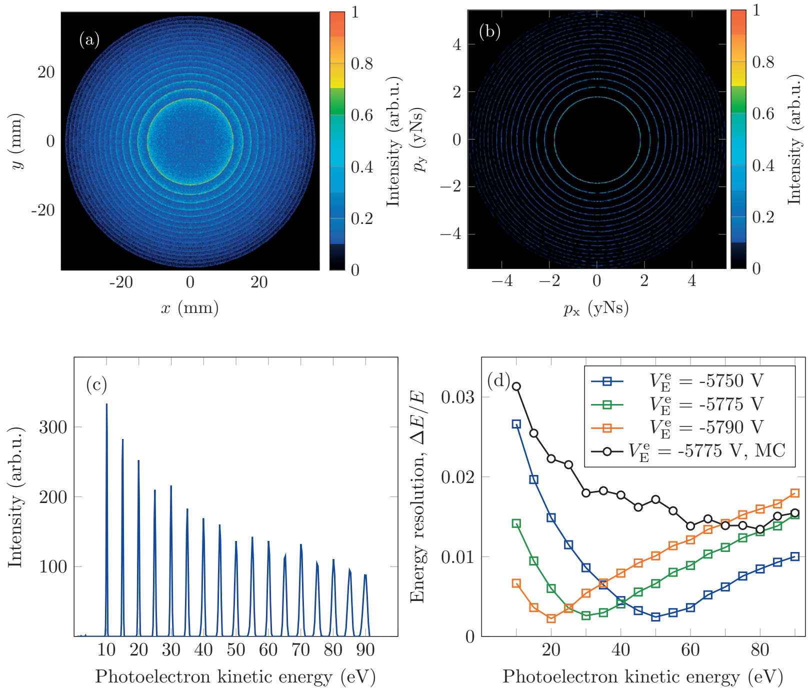

Figure 2.18: DVMIS Monte Carlo simulation of high-resolution electron mode. (a) The 2D momentum distribution of spawned electrons with kinetic energies between 10 and 90 eV. The corresponding retrieved Abel-inverted 3D momentum distribution is shown in (b). The distribution is then angularly integrated and energy calibrated to obtain the spectrum shown in (c). The FWHM of Gaussian fits to the peaks in the spectrum is used to calculate the simulated energy resolution, shown in black in (d). The results obtained with the 27 particle model for different extractor voltages are shown for comparison. (Reproduced from Paper V.)

energy resolution is plotted as open circles in panel (d). Further simulations are presented in Paper V.

During the commissioning of the spectrometer it was found that the mesh almost completely prevented penetration of electric fields from the ion side, while still transmitting about 80 % of the photoions. The ion imaging was compromised to some degree, and the recorded image exhibits a mesh pattern superimposed on a rather extended ion distribution, shown in Fig. 2.19(a) for the case of photoions of N_2. The resolution of the measured kinetic energies of the photoions is slightly deteriorated, due to the initial drift through the repeller electrode, as shown by the results from the MC simulations presented in Paper V.

In this experiment, the photoelectrons were also recorded simultaneously, as shown in Fig. 2.19(b). Note, that in panels (a) and (b) the left halves of the images show the raw data and the right halves the retrieved 3D momentum distributions respectively. The ability of

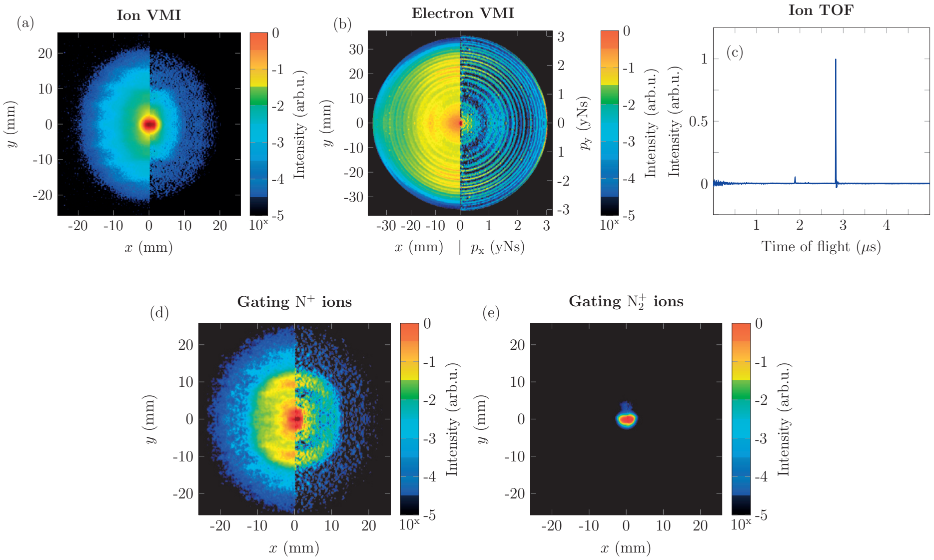

Figure 2.19: Panels (a) and (b) show the experimental presented in Paper V. Molecular nitrogen was ionized with an XUV pulse train, and the photoions (a) and photoelectrons (b) detected with the DVMIS. Panel (c) presents an average of the TOF traces acquired simultaneously with the photoion and photoelectron VMI data. The significantly larger peak at about 2.8 μs corresponds to the N_2^+ ions detected and the smaller peak about 1.8 μs corresponds to the N^+ ions. Panels (d) and (e) show the results from a separate experiment, in which the ion detector was electronically gated on the N^+ (d) and the N_2^+ (e) photoion signal. In (a), (b), (d) and (e): the left halves represent the raw data, and the right halves show the Abel-inverted complete 3D momentum distributions. (Panels (a) and (b) are reproduced from Paper V.)

the spectrometer to record ion TOF spectra was demonstrated, as shown by the results in Fig 2.19(c). Using the timing information obtained from the TOF spectra, the ion detector can be electronically gated, so as to record only particle impacts during a certain time window, usually about 10 to 20 ns. This temporal resolution is sufficient to distinguish between photoion species, if their m/q are sufficiently different.

In panels (d) and (e) of Fig. 2.19, results are shown from an electronic gating experiment performed for N^+ and N_2^+ photoions. It can be seen that the momentum distribution of N_2^+ is limited to a small area in the center of the detector, corresponding to small kinetic energies imparted by photoionization, (e). For N^+ ions however, several Coulomb explosion and dissociation channels can be accessed (for details see Paper V), resulting in several disc-shaped momentum distributions, (d).

The 3D momentum distributions retrieved from the photoionization of N_2 were then angularly integrated and energy calibrated. The resulting spectra are shown in Fig. 2.20(a) and (c) for ions and electrons respectively. The features in both spectra were successfully assigned to their corresponding original electronic states and fragmentation channels. Panel

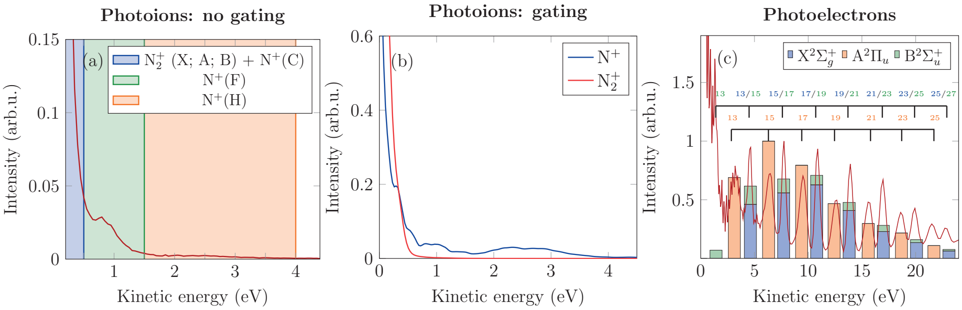

Figure 2.20: The photoion and photoelectron spectra obtained from the recorded momentum distributions in Fig. 2.19 (a) and (b) are shown in panels (a) and (c). The attributed contributions from the different ionic fragments and electronic states are shown in different colors. Panel (b) displays the photoion spectra calculated from the recorded momentum distributions of the gated detection experiment, shown in Fig. 2.19 (d) and (e).

(b) in Fig. 2.20 shows the results from the gated detection ion measurement. The results from the gated detection and the assigned fragmentation channels in panel (a) agree well: the contribution from N_2^+ dominates at lower kinetic energies (< 0.5 eV) and the N^+ contribution extends from low energies up to 4 eV, reproducing notable features around 1 and 2.5 eV.

The agreement between the gated results and the assignments in Paper V, demonstrates the abilities of the DVMIS in combination with gated detection. However, several drawbacks are associated with the gated detection technique. Firstly, the temporal resolution is limited by the width of the voltage gate, which makes the differentiation between ionic species that are only one or two atomic mass units apart unfeasible. This scenario is very common when investigating hydrocarbons, which were the subject of several studies conducted at the High-Intensity XUV Beamline. Secondly, the ability to record an ion TOF signal is lost, since the detector is turned off for all but the selected ion species. Furthermore, the technique can be very time-consuming, since the time required for a measurement scales linearly with the number of ionic species to be recorded. In the case of hydrocarbons, or other larger molecule, it may be necessary to record several dozen fragments, some of which will have very low count rates, necessitating longer acquisition times.

The drawbacks mentioned above, combined with the desire to study more complex molecules, led to the decision to apply the covariance mapping technique rather than gating at the High-Intensity XUV Beamline. In contrast to gating, covariance mapping requires only one long measurement, using several tens of thousands or if necessary sometimes, hundreds of thousands, of laser shots, which can also be very time-consuming. A detailed introduction to the covariance technique can be found in section 3.2 and covariance mapping from the High-Intensity XUV Beamline results are presented in section 4.1 .

3 Charged Particle Detection and Analytical Techniques

Photoionization events, and molecular or atomic dynamics prior to, or after, the event, are often investigated to study ultrafast processes in molecules. At least one electron and at least one ion will be generated in each ionization event. When using a low-intensity light source or low-density gas targets, there may only be one photoionization event per light pulse, or, in the case of a continuous light source, only one event during the acquisition time window of the detector. Under such conditions, coincidence detection is a very powerful technique [84]. This technique will be introduced briefly in Section 3.1. In this regime, it can be assumed that all the detected particles originate from the same photoionization event, and their correlations can be readily retrieved. This information can then be used to reconstruct the dynamics taking place to gain insight into the mechanism involved in the breakup process.

The advent of intense XUV light sources [15, 40, 48] provided much higher numbers of events per shot, but at limited repetition rates. In this regime, many photoions and photoelectrons are created by each pulse. This makes the retrieval of their correlations more complicated, since each particle detected has many potential partners. Covariance mapping [85] has been shown to be a feasible method to obtain correlation information under these conditions. The basic principles, the influence of light source intensity fluctuations and ways of correcting for them will be presented in Section 3.2.

3.1 Coincidence Detection

Coincidence detection was used as early as 1929, when W. Bothe and W. Kolhörster used two Geiger-Müller tubes for the coincident detection of cosmic radiation [86]. The technique has been used in the investigation of photoionization processes since the late 1960s. Many different schemes have been established: photoelectron-photoion-coincidence spectroscopy (PEPICO) [87], photoion-photoion coincidence spectroscopy (PIPICO) [88], photoelectron-photoion-photoion coincidence (PEPIPICO) [89], ion-neutral coincidence [90], and electron-electron coincidence techniques [91]. An introductive overview is given in a review by T. Arion and U. Hergenhahn [84].

In the coincident detection of photoionization products, it is assumed that all the particles recorded during an event are correlated. In order for this assumption to be valid, the particles must originate from the same photoionization event. Thus, the average number of events per laser shot, must be very low, typically less than one event per shot, as multiple events would lead to false correlations. These can be corrected for, but only to a limited degree [92]. In the experiments performed during this work, several hundreds to thousands of ionization events were detected per laser shot, which is far beyond the coincidence regime. It is possible to reduce the laser intensity or the target density to decrease the event rate, but unfeasible considering the low repetition rate (10 Hz) of the light sources employed, as long recording times would be necessary to record a sufficient number of events. Consequently, alternative detection and analysis schemes had to be found, and covariance detection seemed to be appropriate for this event rate regime.

3.2 Covariance Analysis

In this section the basic principles of covariance are first described on a very general level, after which an example of the application of covariance mapping in a simulation with a virtual detector is presented. An overview of recent implementations of covariance analysis can be found in a review by L. Frasinski [93]. A more fundamental mathematical description is given in W. Krzanowski's book *Principles of Multivariate Analysis* [94]. In this section $X^{(i)}$ denotes the value of variable **X** in the i$^{\text{th}}$ iteration of an experiment, whereas X_m denotes the m$^{\text{th}}$ component of the vector **X** and X_{mn} is the element of a matrix **X** that is located in the m$^{\text{th}}$ row and n$^{\text{th}}$ column.

3.2.1 Principles of covariance

Any two random variables $\mathbf{X} = \left[X^{(1)}, X^{(2)}, ..., X^{(N)}\right]$ and $\mathbf{Y} = \left[Y^{(1)}, Y^{(2)}, ..., Y^{(N)}\right]$ with a nonzero second central moment (variance) can be correlated, anti-correlated or not correlated. The covariance of these two variables is a measure of their joint variability over the course of N iterations. It yields information on whether a positive change in the value of **X** is, on average, associated with a positive change in **Y** (correlated), or a negative change in **Y** (anti-correlated), or whether there is no relation in the variations of the two variables (not correlated). This can be expressed as:

$$\mathrm{cov}(\mathbf{X},\mathbf{Y}) = \big\langle(\mathbf{X} - \langle\mathbf{X}\rangle)(\mathbf{Y} - \langle\mathbf{Y}\rangle)\big\rangle, \tag{3.1}$$

which can be simplified to

$$\mathrm{cov}(\mathbf{X},\mathbf{Y}) = \langle\mathbf{XY}\rangle - \langle\mathbf{X}\rangle\langle\mathbf{Y}\rangle, \tag{3.2}$$

$$\text{where } \langle\mathbf{X}\rangle = \frac{1}{N}\sum_{i=1}^{N} X^{(i)} \text{ and } \langle\mathbf{XY}\rangle = \frac{1}{N}\sum_{i=1}^{N} X^{(i)}Y^{(i)}\,. \tag{3.3}$$

$\langle\mathbf{XY}\rangle$ is a measure of the common occurrence of **X** and **Y**, which indicates correlation, but may also include false correlations. $\langle\mathbf{X}\rangle\langle\mathbf{Y}\rangle$ estimates the uncorrelated common occurrences and thus acts as a correction [95]. The case where **X** and **Y** have different dimensions will be discussed in Section 3.2.2.

The amplitude of the covariance of **X** and **Y** scales with their deviations from their respective central moments (mean). To obtain a measure of their correlation covariance can be normalized by dividing by the standard deviations of the random variables. This is called the Pearson correlation coefficient and has values between -1 (anti-correlated) and $+1$ (correlated):

$$\mathrm{corr}(\mathbf{X},\mathbf{Y}) = \frac{\mathrm{cov}(\mathbf{X},\mathbf{Y})}{\sqrt{\mathrm{var}(\mathbf{X})\mathrm{var}(\mathbf{Y})}}. \tag{3.4}$$

The Pearson correlation coefficient quantifies the absolute correlation between two variables. The fact that covariances of physical quantities are expressed in real physical units can yield (additional) information about the processes being investigated [95].

Covariance is unaffected by uncorrelated noise $\mathbf{a}$, due to its linear nature:

$$\mathrm{cov}(\mathbf{X}+\mathbf{a},\mathbf{Y}) = \mathrm{cov}(\mathbf{X},\mathbf{Y}) + \mathrm{cov}(\mathbf{a},\mathbf{Y}), \tag{3.5}$$

where $\mathrm{cov}(\mathbf{a},\mathbf{Y}) = 0$ for uncorrelated noise. The same applies for any uncorrelated contribution introduced into the observation.

3.2.2 Covariance mapping

In the above, covariance was described in general terms, not taking the dimensions of $\mathbf{X}$ and $\mathbf{Y}$ into account. Here, the cases up to $\mathbf{X}$ being a matrix and $\mathbf{Y}$ being a vector will be considered. Within these limitations the following holds true:

$$\dim(\mathrm{cov}(\mathbf{X},\mathbf{Y})) = \dim(\mathbf{X}) + \dim(\mathbf{Y}). \tag{3.6}$$

If both variables have scalar dimensions ($\dim(\mathbf{X}) = \dim(\mathbf{Y}) = 0$), then the covariance will also be of scalar dimension. In this section, the dimension of a variable is considered to be equal to its dimension in a single iteration. The fact that the collection of all data points over the iterations constitutes an additional dimension is neglected here, since it has no influence on the dimension of the covariance result. In the next step, $\mathbf{X}$ may be a vector and $\mathbf{Y}$ still a scalar ($\dim(\mathbf{X}) = 1,\ \dim(\mathbf{Y}) = 0$), thus, the covariance is also a vector with the same length as $\mathbf{X}$.

If $\mathbf{X}$ is a vector of length m and $\mathbf{Y}$ a vector of length n ($\dim(\mathbf{X}) = 1,\ \dim(\mathbf{Y}) = 1$, $\dim(\mathrm{cov}(\mathbf{X},\mathbf{Y})) = 2$). In such a case the covariance will be an $m \times n$ matrix of the form:

$$\mathrm{cov}(\mathbf{X},\mathbf{Y}) = \begin{bmatrix} \mathrm{cov}(X_1,Y_1) & \mathrm{cov}(X_1,Y_2) & \dots & \mathrm{cov}(X_1,Y_n) \\ \mathrm{cov}(X_2,Y_1) & \mathrm{cov}(X_2,Y_2) & \dots & \mathrm{cov}(X_2,Y_n) \\ \vdots & \vdots & \ddots & \vdots \\ \mathrm{cov}(X_m,Y_1) & \mathrm{cov}(X_m,Y_2) & \dots & \mathrm{cov}(X_m,Y_n) \end{bmatrix}, \tag{3.7}$$

This is called a covariance map and consequently the term “covariance mapping” can be used if the covariance has a dimension greater than 1.

In some of the covariance mapping experiments carried out during this work, $\mathbf{X}$ was a series of VMI recordings collected over N laser shots ($\dim(\mathbf{X}) = 2$) and $\mathbf{Y}$ was the shot-to-shot integral over q selected molecular fragment channels in a TOF spectrum ($\dim(\mathbf{Y}) = 1$). The resulting covariance map would have a dimension of 3. This means every vector element Y_k of $\mathbf{Y}$ would generate a matrix with $\mathbf{X}$ like:

$$\operatorname{cov}(\mathbf{X}, Y_k) = \begin{bmatrix} \operatorname{cov}(X_{11}, Y_k) & \operatorname{cov}(X_{12}, Y_k) & \dots & \operatorname{cov}(X_{1n}, Y_k) \\ \operatorname{cov}(X_{21}, Y_k) & \operatorname{cov}(X_{22}, Y_k) & \dots & \operatorname{cov}(X_{2n}, Y_k) \\ \vdots & \vdots & \ddots & \vdots \\ \operatorname{cov}(X_{m1}, Y_k) & \operatorname{cov}(X_{m2}, Y_k) & \dots & \operatorname{cov}(X_{mn}, Y_k) \end{bmatrix}, \tag{3.8}$$

resulting in a total of q matrices or covariance maps like this.

3.2.3 Covariance mapping simulation

In an experiment, in which the momentum of charged particles is mapped (VMI) or imaged onto a 2-dimensional detector (e.g. MCP), the detector is (usually) incapable of distinguishing between different kinds of particles. This differs from a TOF spectrometer, where particles with different m/q are distinct by their different flight times. If both the momentum distribution and the TOF spectrum are recorded, covariance mapping could be applied to identify individual momentum distributions of selected fragments. Since the flight time is an accessible observable in VMI spectrometers, this approach will be exemplified through a simplified simulation of this experimental scenario. Using the 2D image from the VMI and q different fragments in the TOF spectrum, according to Equation 3.8, q 2-dimensional covariance maps can be calculated.

In this simulation, a virtual detector with 80 × 80 pixels represents the charged particle detector in a VMIS and is the two-dimensional random variable **X**. Three random variables **A**, **B** and **C** serve as observables for the number of charged particles, of kind A, B or C, detected per shot as it would be detected with a TOF spectrometer. The random (integer) numbers generated for **A**, **B** and **C** for each shot determine the number of counts generated in the virtual detector in a specified area, as illustrated in Fig.3.1 (a). Here, it is important to note that, for the covariance to be of any value, the observed random variables must have a nonzero variance, since covariance is a measure of their joint variation. In a VMI detection scheme, centrocymmetric patterns (e.g. rings, discs) are typically observed due to symmetries in the experimental geometry. Large areas of these patterns also tend to overlap on the recorded images. This is reflected in the shapes and positions of the specified target areas for **A**, **B** and **C**. In order for covariance mapping to be useful, the areas designated for the variables should be clearly distinguished in the covariance maps.

The simulation was run for 10 000 iterations. In each iteration i, normally distributed random integer values $A^{(i)}$, $B^{(i)}$ and $C^{(i)}$ are generated around a common mean value of 9.2 counts per shot, with a standard deviation of 2. Some uncorrelated noise counts, which constitute about 4 % of the total signal, are also distributed over the whole detector. The number of hits according to the generated values is then created in each single-shot image

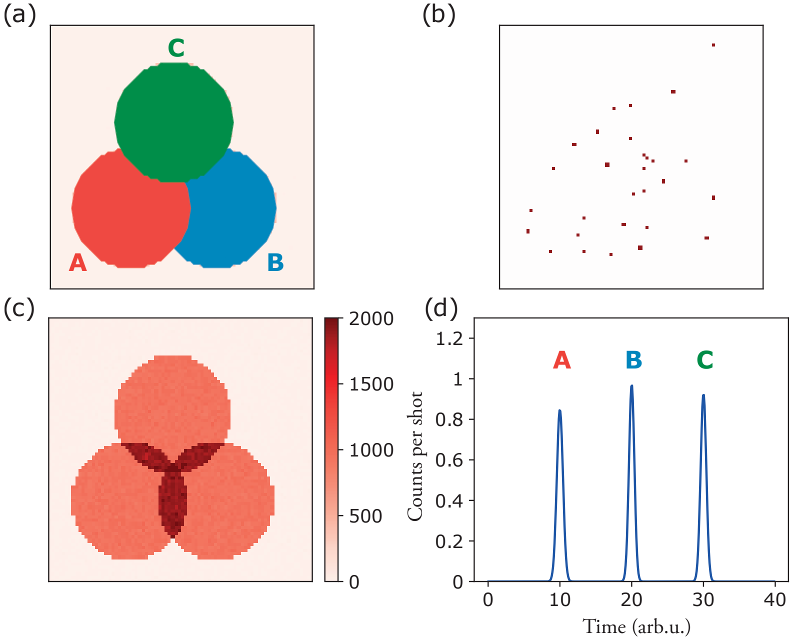

Figure 3.1: Simulation of a covariance analysis of three observables A, B and C on a virtual square detector with an area of 80x80 pixels. Each observable has a designated area, in which their counts are distributed every iteration. Panel (a) displays these areas, note that all areas partially overlap. A generated single shot image that is shown as an example in (b). The detector does not distinguish between the variables, and an accumulated image of all the counts after 10 000 iterations is shown in (c). Panel (d) shows a flight-time spectrum representation of the data for variables A, B and C as they could be observed in an experiment.

recorded by the virtual detector. An example of such an image is shown in Fig.3.1 (b). It can be seen from the number of counts, that this simulation is well outside the scope of the coincidence regime, which requires less than 2 hits per frame. The single-shot images of the detector and the sets of values for **A**, **B** and **C** comprise the dataset. An accumulated image including all frames is presented in (c), and a representation of A, B and C sketched as a TOF spectrum in (d). The covariance of every pixel in **X** with **A**, **B** and **C**, respectively, can now be calculated individually, since every pixel is an independent variable. The results are shown in Fig.3.2 (a-c). It can be seen that each variable exhibits significant covariance with their designated area on the detector, while traces of the other two areas are visible. No apparent influence of the random noise is visible, as predicted by Equation 3.5, can be seen.

These simulated conditions are very static and may not reflect a realistic experimental scenario, where the intensity of the light source, **I**, undergoes shot-to-shot fluctuations. In order to take this into account, a Poisson distributed, random integer number was generated each shot around 50 ($\lambda = 50$), with a standard deviation of 7.1, to model light source fluctu-

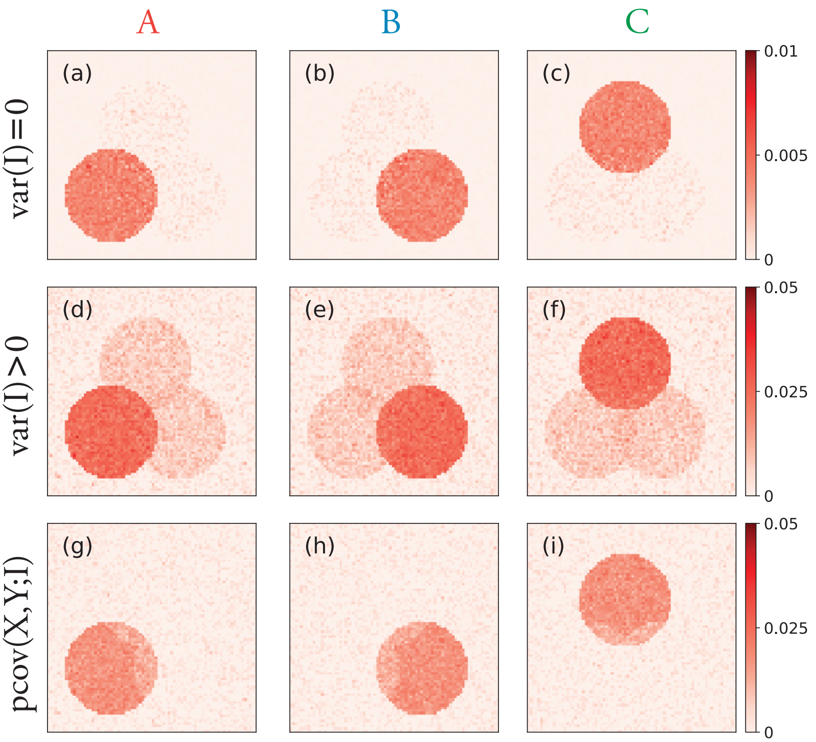

Figure 3.2: Resulting maps from covariance simulation. Panels (a-c) display the covariance maps of the virtual detector X and random variables A, B and C respectively, without any variation of the total number of incidents I. The case of a nonzero variation of I is shown panels (d-f) with the corresponding results of the partial covariance in panels (g-i), which represent an estimate of the maps in (d-f) where an estimate of the influence of the intensity variation is removed.

ations. The effects of this variation in the light source are shown in Fig.3.2 (d-f). Although the main features remain mostly unchanged compared to the case of nonzero intensity variation, it is obvious that the false correlations of each variable with the areas of the remaining two variables are considerably stronger than in the nonzero variation case in Fig.3.2 (a-c). Furthermore, the amplitude of the noise, which is distributed over the whole image, increased significantly. The increased covariance between the variables can be attributed to their common dependence on the intensity **I**, which introduces false correlations.

False correlations between two random variables (**X** and **Y**) caused by a fluctuating associated parameter, **I**, can be calculated and thus corrected for. If a data subset is selected, in which the value of **I** is constant, the variance of **I** vanishes, and thus also the influence on the correlation of **X** and **Y**. This is not always feasible, and in order to make use of all the data collected, the correlation of **X** and **Y** when **I** was held constant can be estimated [94]:

$$\mathrm{pcov}(\mathbf{X},\mathbf{Y};\mathbf{I}) = \mathrm{cov}(\mathbf{X},\mathbf{Y}) - \frac{\mathrm{cov}(\mathbf{X},\mathbf{I})\mathrm{cov}(\mathbf{I},\mathbf{Y})}{\mathrm{var}(\mathbf{I})}, \tag{3.9}$$

where division by the variance of **I** eliminates the dependence on the amplitude of **I**. This is referred to as partial covariance. Experimentally, this means that **I** must be recorded on a single-shot basis, in addition to **X** and **Y**. This correction was applied to the results of the simulation (Fig.3.2 (g-i)). It can be seen that the false correlations are almost completely removed, and the covariance maps resemble those in the case of no intensity variation in (a-c). The overlapping of the designated areas, appears to be bleached. This can be attributed to the fact that covariance is scales with the amplitude of the variables, and as the overlapping areas have the highest number of counts, they will be most affected in terms of amplitude by false correlations, which were overestimated in this partial covariance analysis. The contrast to the noise is improved in comparison to the map in panels (d-f), but not completely removed. Despite these shortcomings, the results show that partial covariance can be used to remove false correlations from covariance maps, especially if the selection of a subset of data with constant intensity is unfeasible.

4 Results

The results of this thesis work can be divided into three categories: covariance mapping experiments at the High-Intensity XUV Beamline; XUV metrology experiments at the High-Intensity XUV Beamline; and time-resolved studies at FLASH.

In the first part, the covariance mapping results obtained with the DVMIS at the High-Intensity XUV Beamline are presented. Photoion-photoion covariance results from the proof-of-principle experiment on molecular nitrogen (Paper V) as well as results on adamantane ($C_{10}H_{16}$) are discussed. In the XUV metrology section the two photon-double ionization experiment in neon (Paper I) and the micro-focusing and wavefront measurements (Paper III and VIII) are described. Then, the time-resolved studies on halomethanes, carried out at the free electron laser facility FLASH, are summarized (Papers II, IV and VI).

4.1 Covariance Mapping Experiments

In this section, covariance mapping results obtained with the DVMIS at the High-Intensity XUV Beamline are described. The general approach in these experiments was to exploit the possibility of acquiring photoelectron and photoion momentum maps as well as photoion TOF spectra simultaneously. By selecting ionic fragments in the TOF for the covariance analysis, the momentum maps could then be filtered to isolate the fragment distributions. In a proof-of-principle experiment on N_2, this is demonstrated for ion TOF-ion VMI and ion TOF-electron VMI covariance mapping, as presented in Paper V. Subsequently, ion TOF-ion TOF covariance and ion TOF-ion VMI covariance mapping was applied to adamantane ($C_{10}H_{16}$). The results are presented in the second part of the section and the preliminary analysis of the fragmentation dynamics is discussed.

4.1.1 Nitrogen covariance mapping

Some of the results from Paper V, from a proof-of-principle experiment on N_2, have already been presented in Section 2.5. Fig. 4.1 shows the acquired ion velocity map and the TOF spectrum. The contributions from the two ion species cannot be distinguished. Nevertheless, covariance mapping as described in Section 3.2 can be applied to disentangle the distributions. The results of the covariance mapping analysis described in Paper V will be presented in this section.

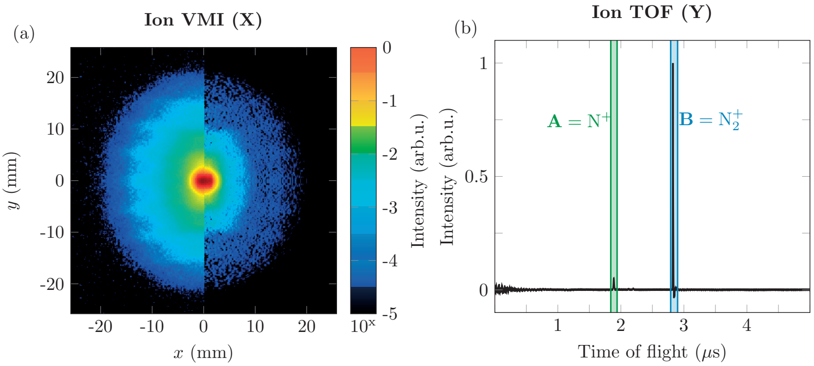

Figure 4.1: Photoion dataset synchronously acquired with the DVMIS using N_2 molecules as target gas. (a) The ion VMI image, where the left half represents the integrated detector image, and the right half the Abel-inverted image. (Reproduced from Paper V.) (b) The acquired ion TOF spectrum. The time windows used for the covariance analysis are indicated in green (N^+) and blue (N_2^+).

During this experiment, 25 000 single-shot velocity map images and TOF spectra were recorded. Applying the covariance mapping approach as described in Section 3.2, the dataset is comprised of 25 000 2D images, which constitute variable $\mathbf{X}$ (with $\dim(\mathbf{X}) = 2$), and the same number of TOF spectra. The two fragments N^+ and N_2^+ were selected in the TOF spectra and the integral over the time windows indicated in Fig. 4.1(b) was calculated. These two sets of scalar integral results (indicated as **A** and **B** in Fig. 4.1), correspond to variable $\mathbf{Y}$ in two separate analyses (with $\dim(\mathbf{Y}) = 1$). This is the situation described in equation 3.8, regarding the dimensions of $\mathbf{X}$ and $\mathbf{Y}$. The result of $\mathrm{cov}(\mathbf{X}, \mathbf{Y})$ is thus a covariance map (matrix) for each fragment with the same number of elements as a velocity map image. In this analysis partial covariance, according to Equation (3.9), was applied, using the signal from an XUV photodiode as the fluctuating intensity variable **I**.

The covariance maps calculated for N_2^+ and N^+ are shown in Fig. 4.2 (a) and (b). In the N_2^+ ion covariance map (a), the covariance is in the center of the image, corresponding to low kinetic energy ions assigned to the X, A and B electronic states of N_2 (Paper V). This result is expected, since the N_2^+ ions do not acquire up significant amounts of kinetic energy during the photoionization process. The N^+ ion covariance map (b) exhibits both slower ions in

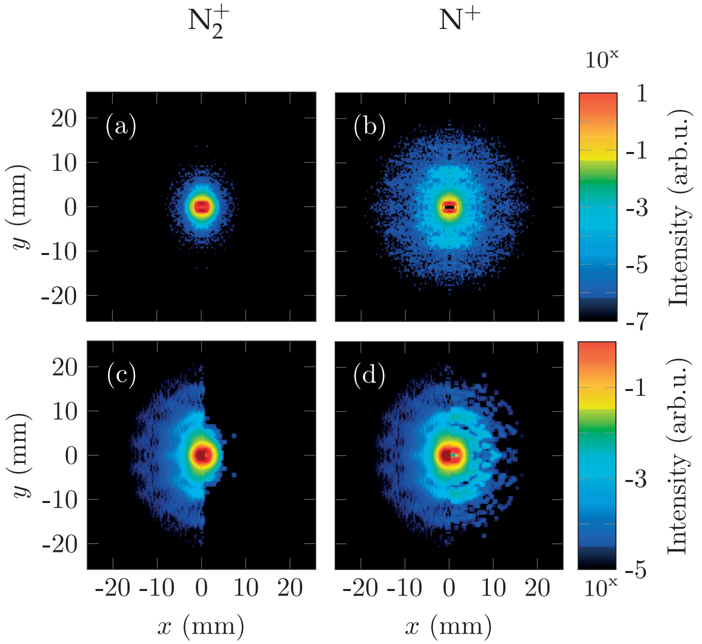

Figure 4.2: (a) and (b) show the partial covariance maps of the N_2^+ and N^+ TOF signals with the VMI detector images. The right halves of (c) and (d) show the Abel-inverted covariance maps, and the left halves the Abel-inverted detector images for comparison. It is apparent that N_2^+ can be assigned to most of the signal in the center of the image, while the signal outside the center can be attributed to N^+ ions. (Reproduced from Paper V.)

the center, attributed to predissociation from the C state, as well as higher kinetic energy ions in two disc-shaped distributions assigned to the F state and the H band [96, 97, 98]. The covariance maps were then treated as velocity map images and Abel-inverted. The results of the inversion are shown in the right halves of the images in (c) and (d). The left halves show the Abel-inverted integrated detector image for comparison. The results of this covariance mapping are consistent with the results obtained from the electronic gating experiment outlined in Section 2.5 and presented in Fig. 2.19. All features in the integrated images were successfully assigned using covariance mapping.

The same analysis was applied to the electron data. Covariance maps in which the electron VMI data (Fig. 4.3(a)) constituted variable **X**, with N_2^+ and N^+ selected from the TOF spectra constituting variable **Y** were calculated in the same way as in the ion data analysis. The resulting covariance maps are not as conclusive as the ion covariance maps and successful Abel inversion was not possible due to insufficient statistics. The maps were instead angularly integrated to obtain transverse momentum spectra, as shown in Fig. 4.3(b). The N^+ covariance is plotted in blue, and most of the signal is seen at low transverse momentum, corresponding to low-kinetic-energy electrons, consistent with being emitted from the dis-

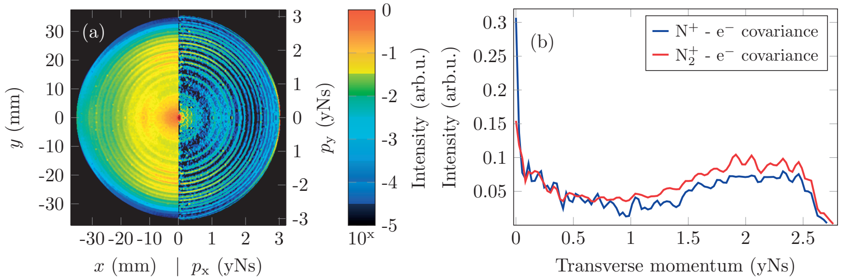

Figure 4.3: Nitrogen electron VMI results (a) and electron covariance momentum spectrum (b) reproduced from paper V. Similar to the ion-ion covariance approach, the TOF signal of the N_2^+ and N^+ channels was used to calculate electron VMI covariance maps with both fragments. These maps were then angularly integrated and the resulting transversal momentum spectra plotted in panel (b). N^+ covariance is predominant for small momenta, while N_2^+ covariance dominates the larger momenta. These attributions agree with the expected momenta resulting from the assigned electronic states corresponding to N_2^+ and N^+ ions.

sociating states. The N_2^+ covariance, plotted in red, displays fewer low-momentum electrons and is dominates in the region of 1.5 to 2.6 yNs (y - yokto = 10^{-24}). The covariance with N^+ resembles the features in this region, but has lower amplitude. This is attributed to the fact that signal in the recorded electron images originated mainly from the X, A and B, states which are stable and produce mainly N_2^+ ions, and dominate the covariance results in this region.

Although the electron-ion covariance analysis was not as satisfactory as the ion TOF - ion VMI covariance analysis, the results presented in Paper V demonstrate that the DVMIS in combination with the XUV light source at the High-Intensity XUV Beamline in Lund is a suitable tool for covariance mapping. The conclusive ion-ion covariance results were especially encouraging, indicating that this scheme can be applied to larger molecular systems, in an attempt to obtain information about the fragmentation dynamics resulting from photoionization with ultrashort XUV light pulses. Several ion-ion covariance mapping experiments have subsequently been performed on larger molecules, yielding promising results, some of which are presented in the next section. No conclusive ion-electron covariance analysis with angular resolution has yet been applied to a molecular target, although this remains a goal currently being pursued at the High-Intensity XUV Beamline.

4.1.2 Adamantane covariance mapping

The promising covariance mapping results, presented in Paper V, demonstrate that ion TOF - ion VMI covariance is a viable method to disentangle different ion distributions in acquired VMI data. A natural next step was, to apply this to more complex molecular systems. In the experiment described in this section, the target molecule was adamantane ($C_{10}H_{16}$), the smallest diamondoid structure (displayed in Fig. 4.4(a)). The results and analysis presented in this section, are part of a study currently being prepared for publication. But due to the size of the dataset and the complexity of the underlying physics, further data analysis and support by theoretical calculations is necessary before a coherent manuscript can be produced.

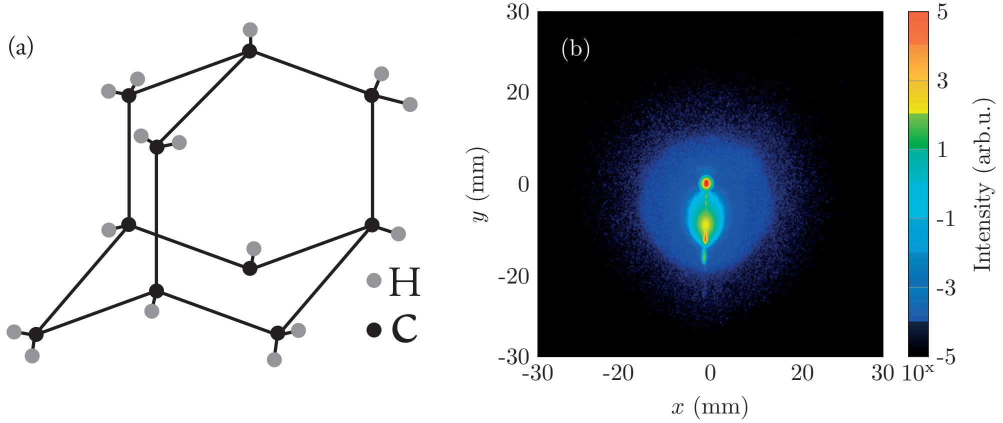

Figure 4.4: (a) Sketch of the molecular structure of adamantane. It has the smallest diamondoid structure. Carbon atoms in the structure are symbolized by black circles and hydrogen atoms by gray circles. Bold lines represent covalent bonds. (b) Ion transverse momentum map of adamantane sample after XUV irradiation. The contributions of all generated ionic fragments are superimposed in this image.

Adamanane has widespread application as a nanomaterial [99], e.g. its occurrence in petroleum is used to trace oil spills [100], its derivatives have uses in medicine[101, 102]. Diamondoids have gained increased interest, when they were found to be the most abundant particles in presolar grains and are also expected to be abundant in the interstellar medium, due to their high stability [103, 104]. Their abundance in the interstellar medium could not be confirmed by recent findings [105]. A possible explanation for this was suggested: their ionization threshold is around 8-9 eV, which is close to the hydrogen Lyman α-lines. Cations are efficiently produced after absorption of photons in this regime, followed by dissociation [106].

The experimental conditions were similar to those described in Section 2.5.3 and in Paper V. Since adamantane is solid at room temperature, it was introduced into the interaction region with the Even-Lavie valve [43, 44] which is installed at the Intense XUV beamline. The used adamantane sample was a powder, that was put into the cartridge of the valve. The cartridge was then heated to 100°C, generating sufficient vapor pressure, so that the now gaseous sample was transported into the interaction region by helium that was used as carrier gas.

The recorded ion velocity map images were summed up and are displayed in Fig. 4.4 (b). The image contains many intense features along the central vertical axis. These can be attributed to ions, that possess initial velocity from the gas jet, but did not obtain any additional kinetic energy from the photoionization process. They are distributed according to their mass, with the heavier fragments being recorded with more distance to the center. This indicates the production of many charged fragments. Furthermore, several more spread out features are visible, originating from ions with additional kinetic energy, obtained in photodissociation or Coulomb explosion processes.

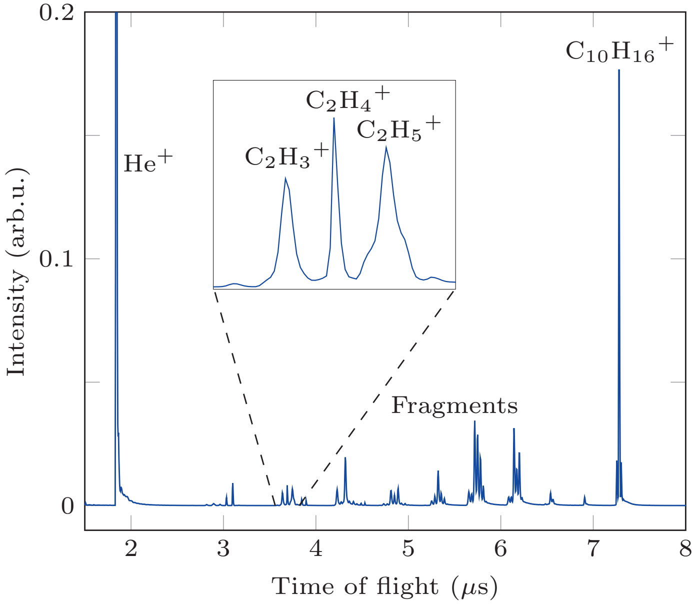

Figure 4.5: Acquired ion TOF data from adamantane molecules in helium carrier gas photoionized with XUV light pulses. The spectrum clearly shows the strong helium peak around 1.9 μs flight time, the intact adamantane cation approximately at 7.3 μs and all the ionic fragments, originating from cation dissociation or dication Coulomb explosions, between 3 and 7 μs flight time. A zoom-in highlights the group of $C_2H_x^+$ fragments, with particular attention on $C_2H_5^+$, which was chosen as an example for fragmentation dynamics. The shape and width of this particular peak indicates it acquired additional kinetic energy after the photoionization event.

The recorded ion TOF spectrum, displayed in Fig. 4.5, stretches out over 8 μs and contains a variety of features. The strongest signal is the He$^+$ peak from ionized carrier gas at 1.9 μs flight time and the second strongest peak stems from the adamantane cation ($C_{10}H_{16}^+$), located at 7.3 μs. Between these two lines is the signal of the fragments originating from cation dissociations or dication Coulomb explosions. The peaks in this region are distributed in nine groups. Each group corresponds to a different amounts of carbon atoms, starting from the $C_9H_x^+$ group around 7 μs down to the CH_x^+ group at 3 μs flight time.

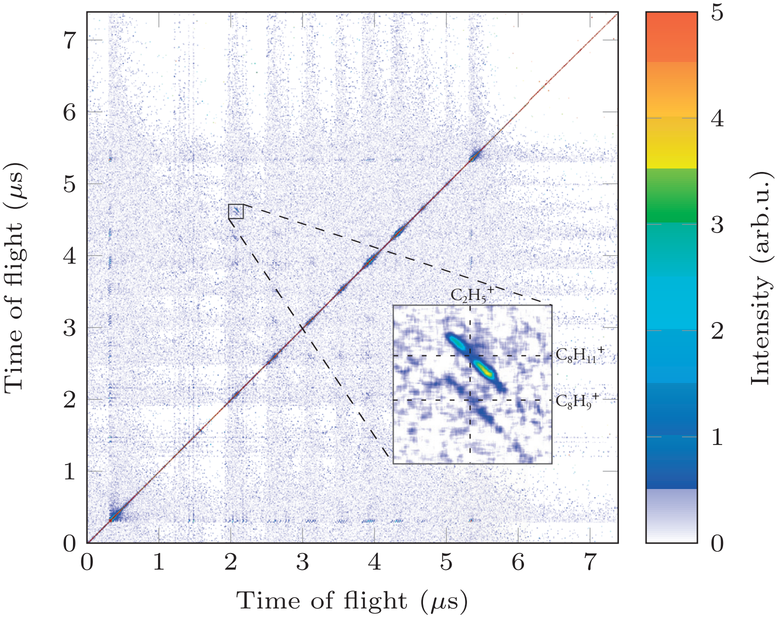

Figure 4.6: Covariance map between all channels in the adamantane TOF spectrum displayed in Fig. 4.5. The diagonal is saturated, since it contains the autocorrelation of each channel. The covariance map is axial symmetric around the diagonal, since $\mathrm{cov}(X, Y) = \mathrm{cov}(Y, X)$. The zoom-in highlights the covariance of $C_2H_5^+$ with $C_8H_{11}^+$.

In Fig. 4.5, the group of fragments with two carbon atoms, but different number of hydrogen atoms, is highlighted with a zoom-in. The peak shape and width of the $C_2H_5^+$ photoion peak stands out. The shoulders on the side of the peak, increasing the overall width, indicate a larger spread of momentum. Some ions picked up momentum towards the detector and thus arrived earlier, causing the shoulder on the left side. Ions that gained momentum away from the detector were consequently arriving later and are the origin of the right shoulder of the peak. Possible causes of this momentum pick-up are dissociation or Coulomb explosion processes. In case of a Coulomb explosion, $C_2H_5^+$ would have a photoion fragment partner, whose detection would be correlated to that of $C_2H_5^+$. Another reason to specifically study the dynamics surrounding $C_2H_5^+$, is its mere occurrence in the spectrum, since a hydrogen transfer is required to produce it. A covariance analysis correlating all TOF channels with each other was conducted to investigate the fragmentation dynamics further.

The covariance map obtained from the TOF spectrum is shown in Fig. 4.6. The diagonal is saturated, since it shows the correlation of every channel with itself. It is also the axis of symmetry for the covariance map, because $\mathrm{cov}(X, Y) = \mathrm{cov}(Y, X)$. Many correlations between ionic fragments were revealed by this map, the analysis of the majority is still ongoing. A particularly interesting region in the map was found to be around the $C_2H_5^+$ photoion. It exhibits correlation with several other fragments. One is particularly highlighted in the zoom-in of the figure. $C_2H_5^+$ has the strongest correlation with $C_8H_{11}^+$. In this fragmentation, no neutral fragment was produced. The underlying process can be formulated as:

$$C_{10}H_{16}{}^{2+} \rightarrow C_2H_5{}^+ + C_8H_{11}{}^+. \tag{4.1}$$

The momentum between $C_2H_5^+$ and $C_8H_{11}^+$ is divided equally and the momentum vectors of both fragments will point in opposite directions, due to momentum conservation. If $C_2H_5^+$ moves towards the detector, corresponding to the earlier shoulder in the TOF peak, $C_8H_{11}^+$ moves away from the detector, corresponding to the later shoulder in the TOF peak and vice versa. This behavior is the reason for the tilt of the island of correlation signal in the covariance map. Covariance distributions like this are indications for Coulomb explosions. In case of equal momentum distribution, without the production of a neutral fragment, the slope of the tilt is expected to be -1, which is the case for $C_2H_5^+$ and $C_8H_{11}^+$. These two partners would form the full molecule together. If that wouldn't be the case and a slope of -1 was obtained regardless, a split-off of a neutral partner prior to the Coulomb explosion can be concluded. The slope in the covariance map contains information about which of the ionic fragments emitted the neutral partner, if any. Slopes between 0 and -1 indicate the departure of a neutral fragment from the fragment on the y-axis. And slopes smaller than -1 from the fragment on the x-axis.

Analogous to previous procedure (as in Section 4.1.1), TOF-ion VMI covariance maps for all fragments were calculated. A non-exhaustive selection is shown as insets in the mass spectrum displayed in Fig. 4.7. Many of the calculated maps exhibit ring or disc-like structures. The recorded ions thus obtained momentum from either photodissociation or Coulomb explosion processes. In case a fragment was part of a Coulomb explosion, it should be detected in correlation with its reaction partner and thus visible in the TOF-TOF covariance map (Fig.4.6). 15 fragmentation channels from the dication could be identified and are subject of further analysis, similar to the one presented for the $C_2H_5^+ + C_8H_{11}^+$ channel.

In Fig. 4.8(a) and (c) the Abel-inverted covariance maps of $C_2H_5^+$ and $C_8H_{11}^+$ are shown. Both maps exhibit ring structures and correlation in the center. The covariance in the center can be attributed to contributions from dissociative channels of the cation, where only small amounts of momentum is obtained by the ionic fragments. The ring structures however, confirm the indications of Coulomb explosion from the TOF-TOF covariance analysis. Both covariance maps (a,c) were angularly integrated and energy calibrated, the resulting spectra a displayed in panels (b) and (d). The Coulomb explosion ring peak of $C_2H_5^+$ is

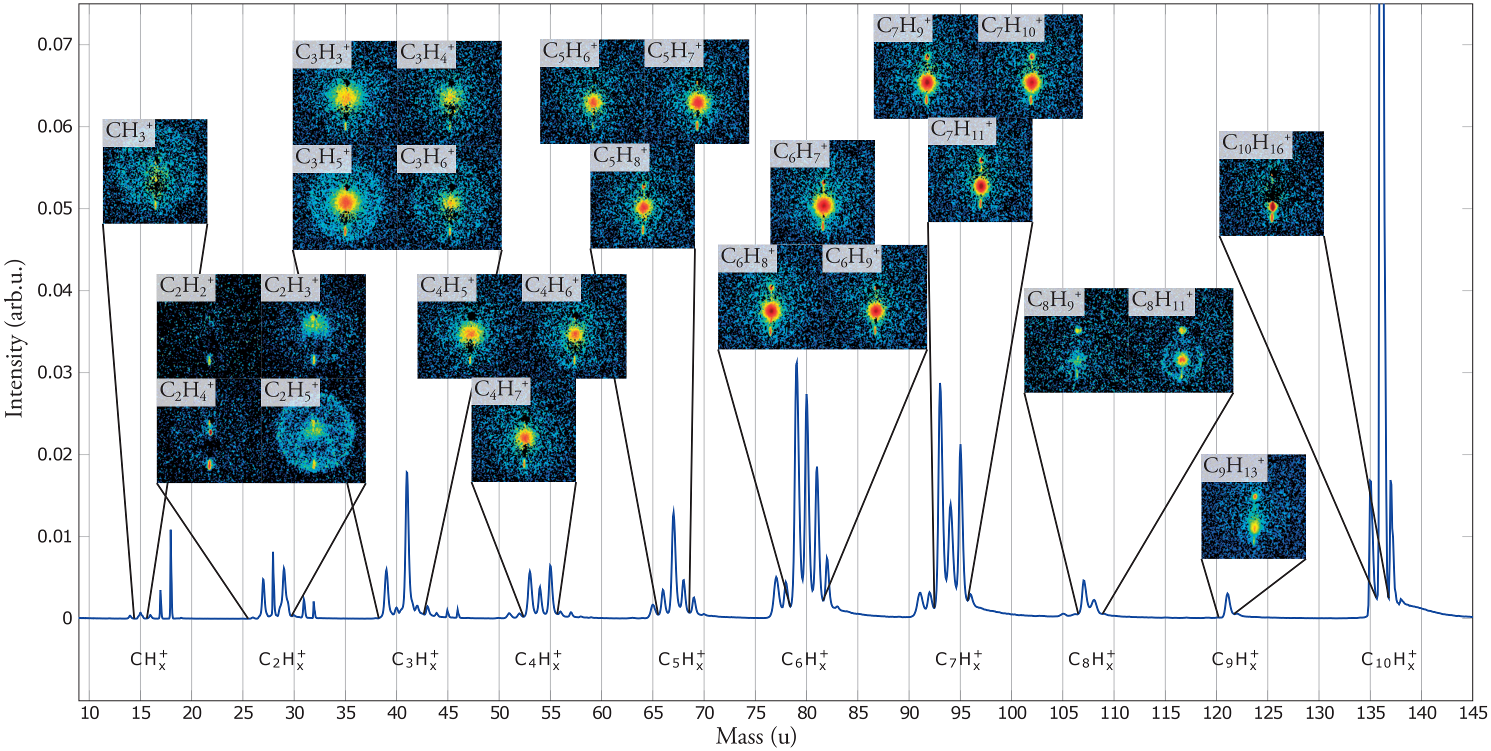

Figure 4.7: Mass spectrum obtained from average adamantane TOF spectrum. Insets show ion TOF - ion VMI covariance maps for the majority of the recorded fragments.

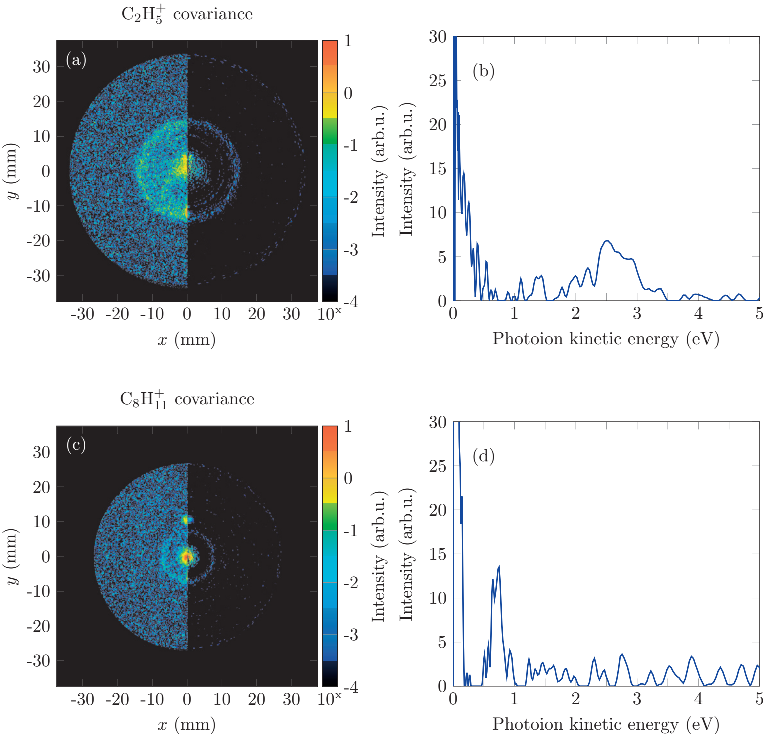

Figure 4.8: Ion TOF - ion VMI covariance mapping: (a) shows the ion covariance map for the $C_2H_5^+$ fragment, where the left half is the raw covariance and the right half is Abel-inverted. Angular integration and energy calibration yields the transverse kinetic energy spectrum. Panels (c) and (d) show the covariance map and transverse kinetic energy spectrum for the $C_8H_{11}^+$ fragment analogously.

located at around 2.5 eV. Considering momentum conservation, the corresponding kinetic energy of $C_8H_{11}^+$ should be scaled with the ratio of the masses 29/107 and thus be 0.68 eV. Convincingly, this is where the ring peak is located in panel (d).

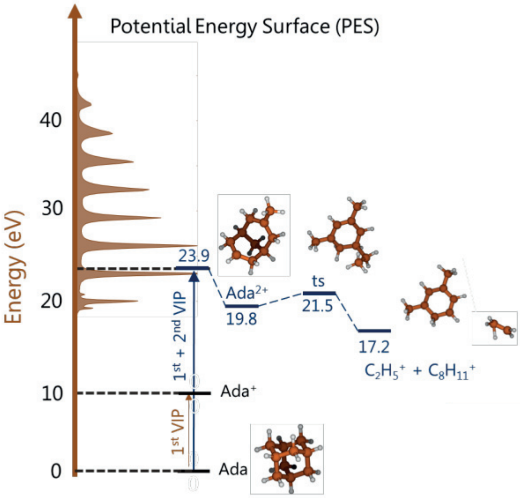

Figure 4.9: Sketch of adamantane potential energy surface simulation results. On the energy axis, the harmonic spectrum is plotted and the first and second ionization thresholds of adamantane are marked. Several intermediate fragmentation dynamic steps are illustrated on the right, note the cage opening before the fragmentation.

Several more fragment pairs like $C_2H_5^+$ and $C_8H_{11}^+$, that are undergoing a Coulomb explosion, were found and are still subject of further investigation. These findings motivated us to seek out a collaboration with a theoretician from the Autonomous University of Madrid (Sergio Díaz-Tendero), in order to get more insight into the structural dynamics in the molecule during the reaction. In Fig. 4.9 the XUV spectrum on the y-axis with the first and second ionization threshold of adamantane are marked. A preliminary result from the density functional theory (DFT) simulations of the potential energy surface (PES) is displayed in the right half of the figure, where the displayed points correspond to minima of the PES. Note the cage-opening and hydrogen migration from the dication to the third point (marked as ts), occurring within 500 fs, and then the fragmentation of the molecule into $C_2H_5^+$ and $C_8H_{11}^+$. This represents one possible trajectory of the molecular dynamic simulation after double ionization, but so far confirms qualitatively the findings of the covariance analysis.

The analysis of the remaining observed fragmentation channels and comparison and interpretation through simulations is still ongoing. The analysis and interpretation of the recorded photoelectron momentum maps is also currently ongoing. Further experimental investigations are planned: beamtime at the FLASH FEL for XUV-XUV pump-probe experiment using on adamantane coincident detection is scheduled later in 2019. In opposite to the experiment presented here, the FEL experiment should deliver time- and spectrally- (between 20 and 30 eV) resolved data and will thus give more direct access to the potential energy surfaces and lifetimes of the induced molecular dynamics.

4.2 XUV Metrology Experiments

In the three experiments that are presented in this section, different properties of the XUV light generated at the High-Intensity XUV Beamline are studied and can be categorized as XUV metrology experiments. In the first experiment the ability to facilitate enough XUV intensity in the focus to double ionize neon atoms with two XUV photons is demonstrated (Paper I). The experimental conditions and results as well as the nature of the two-photon process are discussed. The employed XUV focusing optics are studied in an XUV wavefront measurement experiment, where the wavefront aberrations were successfully determined and even corrected for by aligning the optics accordingly (Paper III). Further XUV wavefront measurement results, complemented by IR wavefront measurements, are presented, in which the influence of the HHG experimental parameters on XUV wavefront quality and yield are investigated as well as the transfer of IR wavefront properties to the XUV wavefront (Paper VIII).

4.2.1 Two-photon double ionization of neon

The High-Intensity XUV Beamline has been developed with the goal of achieving a high XUV yield by upscaling the HHG process (see Sections 2.3.4 and 2.4). The reason for wanting to increase the yield is to enable experiments to be carried out in the nonlinear regime, e.g. multiphoton ionization processes (Paper I) and XUV-XUV pump-probe experiments [107]. At the time of the publication of Paper I, only a few studies had been reported involving two-photon processes in the XUV regime [108, 109, 110, 111]. Paper I presented the first report of the two-photon double ionization of neon using an XUV attosecond pulse train (APT) in an experiment where both direct and sequential ionization channels were accessible. We summarize arguments to distinguish between these two channels as well as the implications of the results to the development of the High-Intensity XUV Beamline.

Two-photon double ionization via a direct process, illustrated in Fig. 4.10 (a), implies that both photons are absorbed simultaneously. If the added photon energy is sufficient to overcome the double ionization threshold (62.5 eV for neon), two photoelectrons are released and a doubly charged ion is left behind. The probability of this process is governed by the two-photon double ionization cross section $\sigma_{\mathrm{d}}^{(2)}$ ([$\mathrm{m}^4\mathrm{s}$]). Double ionization can also proceed sequentially, as shown in Fig. 4.10 (b). First, one photon with energy exceeding the ionization threshold (21.6 eV for neon) is absorbed and a photoelectron is released with a kinetic energy corresponding to the excess energy from the ionization process. The probability of this process is determined by the cross section for one-photon (single) ionization $\sigma_{\mathrm{I}}^{(1)}$ ([m^2]). The ion is now in the Ne^+ ground state, which is not populated in the direct process. For two-photon double ionization via a sequential process, the photon energy

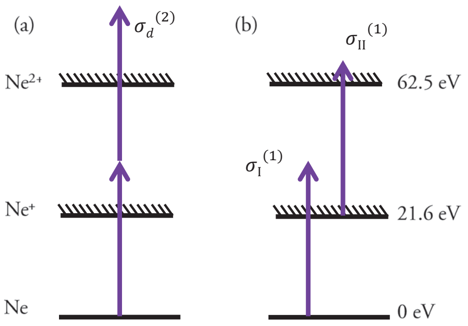

Figure 4.10: Direct (a) and sequential (b) two-photon double ionization pathways for neon atoms. The photoionization cross sections for the direct (σ_d) process, and the sequential process (σ_I and σ_II) are indicated. (Adapted from Paper I.)

needs to overcome the difference between the Ne^+ ground state and the double ionization threshold, equal to 40.9 eV for neon. A second photoelectron is released, with a kinetic energy equal to the excess energy above the ionization threshold of Ne^+. This process has a different cross section, $\sigma_\mathrm{II}^{(1)}$ ([m^2]), than the first ionization process, because the initial state is now the Ne^+ ground state.

The two double ionization channels have different temporal behavior, since in the sequential process, the atom is ionized in an intermediate step and is in the Ne^+ ground state, before a second photon is absorbed that leads to the emission of a second photoelectron. In Paper I, a ratio between the yields of the two channels was derived to gain insight into this different temporal behavior. Within lowest order perturbation theory, the yield for the ionization process can be expressed as a function of the photon flux, F, the pulse duration, τ, and the, previously introduced, cross sections. The ratio between the sequential (N_s^{2+}) and direct double ionization (N_d^{2+}) yields is equal to:

$$\frac{N_\mathrm{s}^{2+}}{N_\mathrm{d}^{2+}} = \frac{(\sigma_\mathrm{I}^{(1)}F\tau)(\sigma_\mathrm{II}^{(1)}F\tau)}{2\sigma_\mathrm{d}^{(2)}F^2\tau} = \frac{\sigma_\mathrm{I}^{(1)}\sigma_\mathrm{II}^{(1)}}{2\sigma_\mathrm{d}^{(2)}}\tau. \tag{4.2}$$

Using values of cross sections for neon from the literature [112, 113, 114], Equation 4.2 predicts comparable yields at a pulse duration below 500 as for photon energies around 41 eV. In the experiment, described in Paper I, a 20 fs long APT consisting of about 15 pulses with estimated durations of approximately 300 as was used. These conditions should favor the sequential channel. The XUV spectrum contained odd-order harmonics of the 800 nm fundamental light between the 15th (23.3 eV) and the 33rd order (51.2 eV). While none of these have sufficient photon energy for single-photon double ionization, several combinations of two would be sufficient to overcome the double ionization threshold of

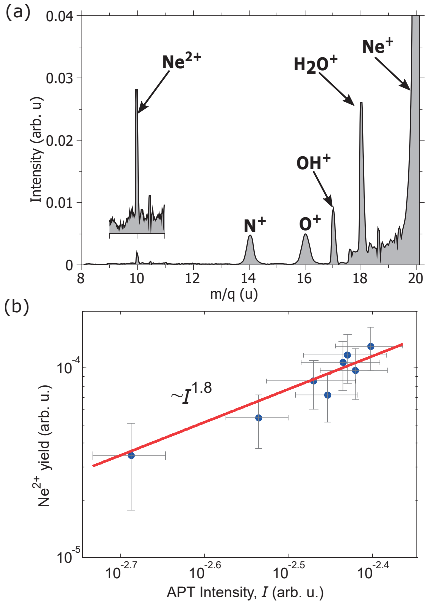

Figure 4.11: Panel (a) shows the mass spectrum, calculated from the acquired TOF spectrum. The region around the Ne^{2+} peak is shown in the magnified inset. Panel (b) shows the Ne^{2+}-yield versus the APT intensity on logarithmic axes. The slope of the linear fit was found to be 1.8, which is close to the expected slope of 2 for a second order nonlinear process such as two-photon double ionization. (Reproduced from Paper I.)

neon at 62.5 eV. Only the highest energy photons can be used for the second step of the sequential process.

In our experiment (see Paper I), the fundamental IR beam was focused into a HHG gas cell a lens with a focal length of 9 m. The experiment was performed prior to the implementation of the split-and-delay unit and two silica plates were used to attenuate the IR. An ion TOF spectrometer operated in Wiley-McLaren conditions [75] and a piezo-nozzle gas jet were installed. Additionally, the focal spot of the XUV was measured. A more in-depth discussion of the focal spot imaging setup and its applications can be found in Paper III.

The acquired TOF data is plotted in Fig. 4.11 (a). Apart from the dominating Ne^+ at 20 u, several peaks associated with species from the background gases (H_2O^+, OH^+, O^+ and N^+) are visible. The Ne^{2+} peak at 10 u is shown magnified in the inset. The ratio between the Ne^{2+} and Ne^+ yields was found to be 0.35 % . The nonlinearity of the Ne^{2+} yield was studied by varying the XUV intensity by changing the gas pressure in the generation gas cell, which does not affect the spectrum significantly. The H_2O^+ yield was used as a measure of the XUV intensity on target. The results of this nonlinearity study are shown in Fig. 4.11 (b) in a double logarithmic plot. The slope of the linear fit was determined to be 1.8, close to the predicted slope of 2 for a two-photon process.

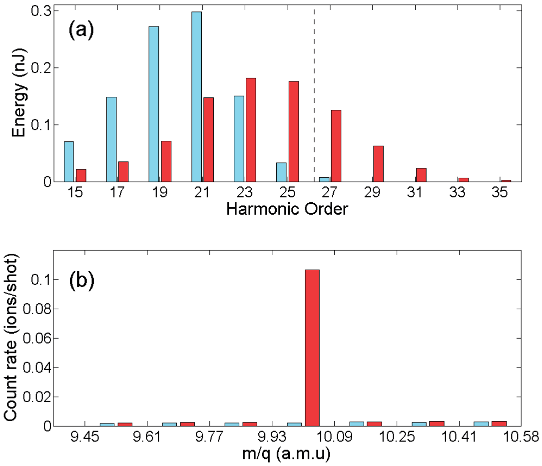

Figure 4.12: The cutoff of the harmonic spectrum was shifted to investigate whether the direct or the sequential process dominated the two-photon double ionization process in neon. In the XUV spectrum in panel (a), the unaltered spectrum with a cutoff around the 35^{th} harmonic order is shown in red. The blue bars correspond to the case, where the cutoff is shifted to the 27^{th} order harmonic. The threshold for the sequential double ionization process (40.9 eV) is indicated with a vertical dashed line between harmonic orders 25 and 27. With the spectral intensity predominantly below the threshold for the sequential process, the Ne^{2+}-yield vanishes for the shifted cutoff harmonic beam (panel (b), blue), while significantly more Ne^{2+} is produced using the unaltered harmonic beam (panel (b),red). (Adapted from Paper I.)

In an attempt to identify the dominant ionization pathway, an additional experiment, where the XUV spectrum was changed, was performed. The aim was to bring the maximum photon energy below the ionization threshold of Ne^{+} (40.9 eV), thus making sequential double-ionization by absorption of two photons impossible. It is important to keep the same XUV photon flux (number of photons / area·time) as in the original experiment, since a variation in flux would obscure any variation due to the change in spectral content.

The experiment was realized by performing HHG in krypton. In addition the IR intensity was adjusted to get an even lower cutoff energy. The XUV pulse energy was controlled by adjusting the pressure in an absorption cell filled with argon, located in the beam path between the generation chamber and the target gas in the application chamber. As visible in Fig. 4.12 (a), generation in krypton lead to an XUV spectrum (blue bars) where only a very small contribution in the 27th order harmonic (41.85 eV) was located above the threshold of 40.9 eV. The Ne^{2+} yield vanishes, shown in blue in panel (b). The comparative measurement at the same XUV pulse energy where the cutoff of the spectrum is located above the threshold, displayed in red (a), shows no reduction in the Ne^{2+} yield (panel (b), red). This indicates that double-ionization of neon occurs predominantly by a sequential process.

This demonstration of nonlinear light matter interaction in the XUV regime was the start of the development at the High-Intensity XUV Beamline towards XUV-XUX pump-probe experiments. The findings from Paper I demonstrated the importance of XUV focusing on the nonlinear signal. The correct alignment of the XUV focusing optics and compensation of wavefront aberrations are essential to achieve enough XUV intensity and are further discussed in Papers III and VIII and Sections 4.2.2 and 4.2.3. The experimental attempts towards XUV-XUX pump-probe experiments have unfortunately been unsuccessful so far, probably due to a lack of sufficient beam pointing and intensity stability, or alternatively due to chromatic aberrations as discussed in Paper VII. Since the implementation of the split-and-delay unit, several upgrades have been implemented in the beamline to improve its performance, such as an active beam stabilization and a reduced beam path length in air. Further upgrades are planned and this ongoing development will be discussed in the outlook.

4.2.2 Micro-focusing experiment

In the experimental results presented in Paper III, the XUV focal spot size and wavefront aberrations were investigated. A wavefront sensor and a scintillation crystal were employed for these purposes. The focusing optics in Wolter configuration [73] and their effect on the focusing conditions were especially scrutinized. The experimental findings were then compared to the results obtained from numerical calculations using the FRED Optical Engineering software (Version 14, Photon Engineering LLC, Tucson, AZ, USA, https://photonengr.com/fred-software/).

The experimental setup was very similar to that described in Section 2.4, but with some minor modifications: an 8.7 m focal length lens was used to focus the IR beam into the HHG chamber, the DVMIS was removed to make room for the scintillation crystal and its optical imaging setup in one part of the experiment and the wavefront sensor setup in the other part. The fundamental IR laser pulses used for HHG were 45 fs long with a pulse energy of 20 mJ. The diameter of the IR beam was apertured to 22 mm (FWHM), and then focused into the generation chamber with a 60 mm long gas cell filled with argon. The deformable mirror had already been implemented to compensate aberrations in the fundamental beam, in conjunction with an IR wavefront sensor. The HHG process was optimized, by varying the aperture, gas cell pressure, and IR focal position via the deformable mirror. The XUV-XUV split and delay unit was translated so that only a single silica plate with IR anti-reflection coating was used, resulting in only a single reflection of the XUV beam between generation and the XUV focusing optics. The residual IR beam was filtered out with a 200 nm aluminum filter directly after the silica plate. An XUV spectrum was acquired, which exhibited odd-order harmonics between the 15^{th} and the 29^{th}. The divergence of the harmonics was extracted from the image obtained with the XUV spectrometer. The divergence of harmonic 19 was determined to be 0.33 mrad. Harmonic 19 was used as benchmark for the results presented in Paper III, since it represents the weighted center of the XUV spectrum.

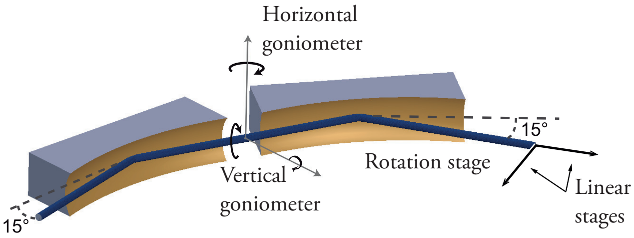

Figure 4.13: The double toroidal mirror assembly in Wolter configuration. Solid arrows indicate translatable axes, and the curved arrows indicate the pivoting axes for revolutions. (Reproduced from Paper III.)

The XUV focusing optics consist of two toroidal mirrors in Wolter configuration, in which any coma aberration introduced by the first mirror should be compensated for by the second mirror. Each mirror is each 30 mm long, and 10 mm high, and their center-to-center distance is 30 mm. Their position and orientation can be precisely manipulated with several goniometers and translation stages as depicted, in Fig. 4.13. The position and orientation of the two mirrors relative to each other is fixed. The angle of incidence is grazing at 15° and the total deflection angle of the assembly is 60°. The combined focal length is 164.2 mm. The HHG light source is located 6 m before the focusing optics. In this configuration the light source is imaged onto a position 170 mm behind the toroidal mirrors. This corresponds to a demagnification of 35. The mirrors are gold-coated for broadband reflectivity in the XUV region to support the broad spectrum of the ultrashort light pulses generated via HHG.

The wavefront measurements were carried out using a wavefront sensor consisting of a Hartmann mask and a XUV CCD camera [115]. A schematic of the working principle is shown in Fig. 4.14. If a flat, non-tilted wavefront, W, hits the mask, it will be diffracted and a series of equidistantly distributed spots will be illuminated on the CCD. These spots serve as a reference. Such a reference image was obtained by generating a spherical wavefront by pinhole diffraction. The diffraction patterns from distorted wavefronts deviate from the reference spots on the sensor. The local wavefront slopes ($\partial W/\partial x, \partial W/\partial y$) in the mask plane are proportional to the deviations. These are calculated for each illuminated hole and the wavefront can then be retrieved over the whole aperture.

The wavefront sensor used in the experiment was developed by the group of Philippe Zeitoun at the Laboratoire d'Optique Appliquée in collaboration with Imagine Optics. The sensor was provided for the duration of this collaboration in the framework of a Laser Lab Europe campaign. It features a 0.1 mm nickel plate with 34 × 34 holes as a Hartmann

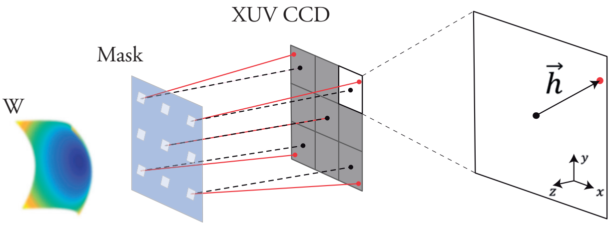

Figure 4.14: Sketch of the working principle of a Hartmann mask-based wavefront sensor. The wavefront W is diffracted by the mask and the diffraction pattern is recorded with the XUV CCD. The black lines correspond to the beam path and pattern of a flat reference wavefront and the red lines to the path and pattern of a distorted wavefront. $\vec{h}$ corresponds to the deviation of the distorted wavefront spot from the reference wavefront spot in one segment of the sensor. (Adapted from Paper III.)

mask. The holes are square-shaped with a side length of 110μm, a separation of 387 μm, and are tilted to avoid overlapping between consecutive diffraction patterns. The accuracy of the sensor was determined to be 0.6 nm root mean square (RMS), which corresponds to $\lambda/70$ RMS at 42 nm (19$^{\text{th}}$ harmonic). The sensor was placed 500 mm after the XUV focus, in order for the beam size to match the aperture.

Two types of wavefront reconstruction were used. The first was the zonal method, where direct numerical integration of the local slopes was applied. The second was a modal method, in which the wavefront is decomposed into a basis of orthogonal polynomials (Zernike polynomials), that represent different aberrations. Thus, aberrations can be extracted independently. More details can be found in Paper III.

The effect of the XUV focusing optics on the wavefront was investigated, and optimal positions of three of the adjustable axes with respect to the wavefront quality were determined. The XUV wavefronts were found to be dominated by astigmatism. It was confirmed that using the Wolter configuration of the double toroidal focusing mirrors minimized the coma aberration introduced into the beam and that even pre-existing astigmatism could be corrected for. A focal spot size of 3.6×4.0 μm^2 was achieved experimentally, which was close to the ideal focal size of 3.2×3.2 μm^2 obtained with a FRED simulation . The focal spot was subsequently imaged with a scintillation crystal, which is combined with a microscope. However, due to saturation of the crystal, despite the use of thicker aluminum filters, the measured focal spot was about 2-3 time larger than the results from the wavefront measurement and the numerical calculations suggest. Optimization of the wavefront and thus also the focal spot size achievable increased the available XUV intensity in the interaction region, which is beneficial for nonlinear XUV light-matter interaction experiments.

4.2.3 Wavefront measurements

Paper VIII presents the investigation of the impact of the HHG experimental conditions on the XUV wavefront and yield, measured after the generation and before the focusing optics. The effect of the variation in fundamental IR laser beam properties was studied in particular. Furthermore, the IR wavefront was also recorded with a separate wavefront sensor, and the impact of the deformable mirror on the IR wavefront quality and subsequently on the XUV wavefront was investigated.

All optics used to deflect the XUV beam towards the sensor were characterized prior to the experiments. A known reference wavefront was generated using a 100 μm pinhole aperture introduced in the path before the XUV beam is incident on the investigated optics. All aberrations recorded must then be caused by the optics, and can thus be used to characterize their impact on the measured XUV wavefronts. The effect of the optics can then be eliminated from the measurements. Unless stated otherwise, λ refers to the wavelength of the 19th order harmonic at 42 nm, which corresponds to the weighted center of the harmonic spectrum. In Paper VIII and some of the figures reproduced from it in this section, the XUV beam is referred to as APT.

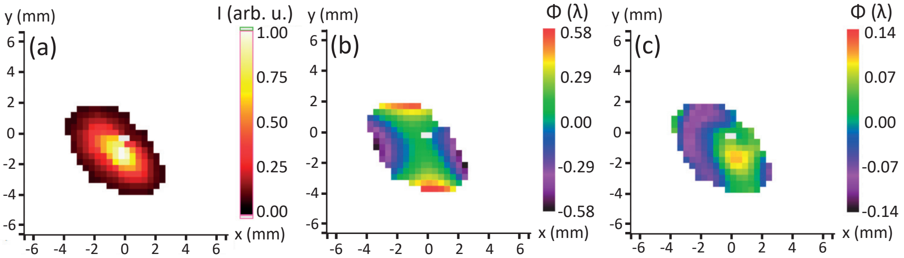

Figure 4.15: Single-shot intensity (a) and wavefront (b) distribution of the complete XUV beam. Panel (c) shows the wavefront after numerical removal of the astigmatism from the wavefront shown in (b). (Reproduced from Paper VIII.)

In one of the measurements, the complete XUV beam wavefronts were recorded. Due to the low divergence of the beam, only 0.2 mrad, the wavefront sensor had to be placed 9.5 m behind the gas cell to illuminate a sufficient number of pupils on the Hartmann mask. This beam path length was achieved by deflecting the beam through a vacuum tube extension prior to the application chamber, and then onto the wavefront sensor. Typical results from these measurements are shown in Fig. 4.15. The spatial phase variation perpendicular to the propagation axis was observed, and this was compared to a perfect parabolic wavefront. The difference is expressed in units of the central XUV wavelength λ. All RMS values are averaged over five laser shots. Figure 4.15 (a), shows the XUV intensity distribution and (b) the recorded wavefront, where it can be seen that the defocus and tilt components were filtered out. The wavefront RMS is $(0.287 \pm 0.064)\lambda$ and is dominated by astigmatism at 0°. It can also be seen in Fig. 4.15(c), where astigmatism has been eliminated, that the remaining aberrations are of significantly lower magnitude at an RMS of $(0.062\pm0.006)\lambda$.

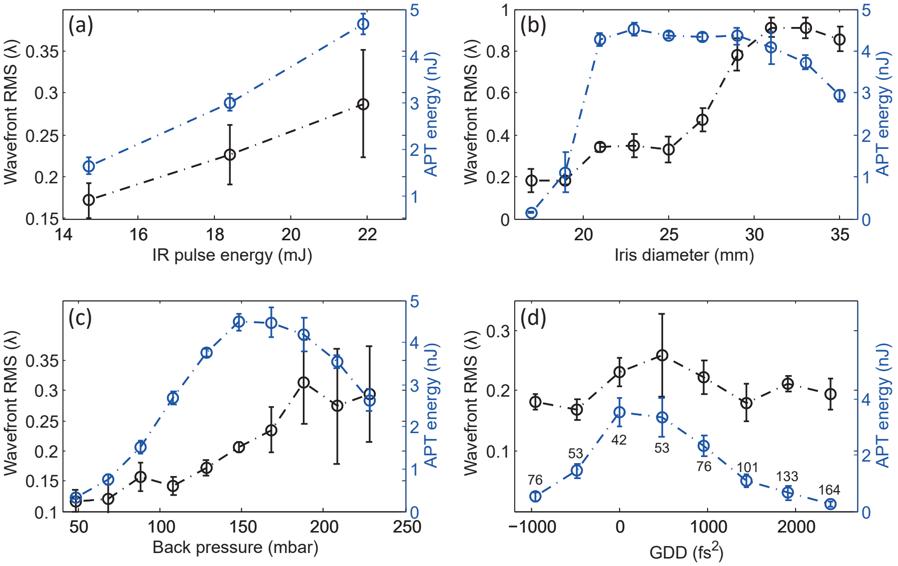

Figure 4.16: Results from the generation parameter scan measurement. The wavefront RMS and the APT energy was measured as a function of the (a) IR pulse energy, (b) (IR) iris diameter, (c) generation gas back pressure and (d) the IR group delay dispersion (GDD). (Reproduced from Paper VIII.)

In the measurements, presented in Fig. 4.16, the IR pulse energy (a), IR beam diameter (b), generation gas pressure (c), and IR group delay dispersion (d) were scanned, while the other parameters were kept constant. The observables in these scans were the wavefront RMS (black) and the XUV pulse energy (blue). The wavefront RMS varies considerably with the scanned parameters from as low as $\lambda/10$ up to almost λ in some cases. High XUV pulse energies are often associated with large aberrations, which means that compromises have to be made between pulse energy and wavefront quality. The wavefront aberrations were mostly dominated by astigmatism, which can be corrected for by focusing optics as shown in Paper III and previously [116, 117]. Since the astigmatism always had a similar orientation, it is apparent that the influence of the IR polarization should be investigated. Three different polarization orientations were studied: horizontal, vertical and 45° with respect to the optical table. The XUV astigmatism and wavefront remained constant in all cases.

It has been previously found that different harmonic orders have different wavefronts [118]. To complement the full beam measurements, 3 harmonic orders were isolated using dielectric multilayer mirrors (orders: 19 (41.4 nm), 23 (35 nm), and 33 (23.9 nm)). The wavefront quality of harmonics 19 and 23 were found to be significantly better than the full beam. Harmonic 33 exhibited a deteriorated wavefront. This was attributed to adjusted generation parameters, which were necessary to maintain sufficient photon flux at harmonic 33 in order to perform single shot experiments.

The relation between the IR beam and the harmonics was further investigated during the experiments. In an effort to improve the XUV wavefront, the deformable mirror was used to improve the IR wavefront. This was very successful and led to a decrease in the RMS XUV wavefront aberration from $\lambda/4$ to $\lambda/11$, while the harmonic spectrum did not change significantly, and the XUV pulse energy increased three-fold. It is apparent that the IR wavefront not only affects the high-order harmonic beam wavefront, but also its shape and size, as well as the conversion efficiency.

4.3 Time-resolved Experiments at FLASH

Several measurement campaigns were carried out at the XUV/soft-Xray FEL facility between 2015 and 2018, all of which were performed at the CAMP endstation at beamline BL1 of FLASH. The studies on halomethanes led to the publication of Papers II, IV and VI, while the results of more recent campaigns have yet to be published. The photodissociation dynamics of different halomethane molecules were successfully probed in time-resolved studies. In the first part of this section, selected results from Paper II will be discussed, mainly concerning the UV initiated photodissociation of CH_2BrI, which was probed with an IR laser pulse. The photodissociation dynamics of CH_3I and CH_2ClI are the subject of the second part of this section, the results of which are presented in Paper VI. Greater attention will be devoted to the results of the CH_2ClI study as covariance mapping was used to analyze the data. The transition of iodine from being bound in CH_3I to being an isolated atom during a photodissociation reaction was observed, and is reported in Paper IV. In this experiment a laser UV pulse pump and FEL soft X-ray pulse probe scheme was successfully implemented. The author's contributions to these studies were mainly experimental, therefore this section will be limited to summaries of only selected results.

In these experiments a fast CCD camera was used for ion imaging. The ion arrical time in an ion VMI spectrometer, depends on m/q, as in a TOF spectrometer. These arrival times are usually on the order of microseconds, while the arrival times of different ionic species can differ by several tens of nanoseconds. It is possible to image the momentum distributions of these ionic species separately with the aid of fast electronics and quickly decaying phosphor screens. The CCD camera used is capable of imaging the momentum distributions of up to four ionic species per shot. The Pixel Imaging Mass Spectrometry (PImMS [119, 120]) camera works at an 80 MHz refresh rate, which corresponds to a temporal resolution of 12.5 ns, and has four timestamp registers in each of the 324×324 pixels. This camera provides the momentum maps of selected ions directly. This feature was exploited in the experiments described in this section.

4.3.1 Photodissociation dynamics of CH_2BrI

Paper II reports on the time-resolved study of the photodissociation dynamics of gas phase CH_2BrI at the CAMP endstation of FLASH (details in Section 2.2.2 and in [41]). The original plan was to use the FEL for time-resolved inner-shell photoelectron spectroscopy (which later succeeded, see Paper IV) in combination with IR (815 nm) or UV (271.6 nm) laser pulses. However, spatial and temporal overlap of the FEL light pulses and the laser pulse could not be achieved. Therefore, the UV and IR laser pulses were used to initiate and probe the photodissociation dynamics of CH_2BrI with a temporal resolution of 170 fs. Transverse momentum distributions were recorded with a VMIS and fragment-resolved

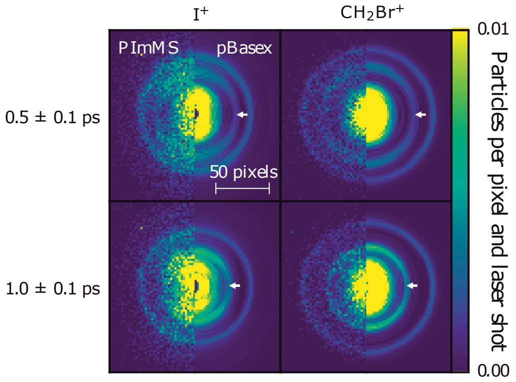

Figure 4.17: Momentum distributions of I^+ and CH_2Br^+ recorded using the DVMIS of the CAMP endstation with the PImMS camera with delays of 0.5 ps and 1.0 ps between pump and probe laser pulses. The left halves of the images show raw data, while the right halves show Abel-inverted images using the pBasex method [121]. The arrows indicate time-dependent features observed for both fragments. (Reproduced from Paper II)

images were obtained with the fast PImMS camera. The images recorded for the I^+ and CH_2Br^+ fragments at 0.5 ps and 1.0 ps delay are shown in Fig. 4.17. The images of both fragments exhibit 3 distinct features, which were attributed to three different processes. The features between the saturated central part and the outer ring (indicated by white arrows) are delay dependent in both fragments. Negative delays indicate that the IR pulse arrives first, while positive delays mean that the UV pulse arrives first.

Angular integration of the momentum distribution (shown for selected delays in Fig. 4.18) elucidates the time dependence (or independence) of the three processes. The process yielding ions with the highest kinetic energies is the irradiation of the molecules with IR photons only. This leads to (multiphoton-) double ionization and Coulomb explosion of the molecule into I^+ and CH_2Br^+ channels centered at (1.73 ± 0.17) eV and (2.31 ± 0.21) eV kinetic energy, respectively. The absorption of a UV photon preferentially leads to breakup of the C-I bond and subsequent photodissociation of the molecule into the neutral fragments CH_2Br and ground state $I(^2P_{3/2})$ or excited state $I(^2P_{1/2})$. The subsequent absorption of a UV photon breaks the C-Br bond of CH_2Br. The absorption of an IR photon during dissociation initiates a Coulomb explosion with charges located on iodine and bromine, yielding the time-dependent channel at 1.76 eV for I^+ and 2.41 eV for CH_2Br^+, the kinetic energies of which slowly decrease to their asymptotic energies of (0.25 ± 0.02) eV and (0.35 ± 0.02) eV with increasing delay. The iodine spin-orbit splitting could not be resolved. The near-zero kinetic energy channels seen in both photoions, were attributed to strong-field or multiple UV photon ionization producing I^+ or CH_2Br^+ with neutral partners. The delay dependent-channel was also modeled using simple assumptions on the time taken for the photodissociation fragments to reach their final velocity, v. The outcome of the simulations is shown in Fig. 4.18.

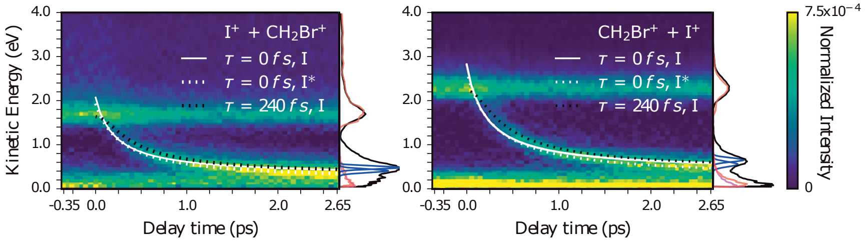

Figure 4.18: Kinetic energy spectrogram of I^+ ions (left) and CH_2Br^+ ions (right), obtained from Abel-inverted momentum distributions. Two static and one time-dependent channel are clearly visible for both fragments. The solid and dotted white lines represent results from a simulation under the assumption that the photodissociaton fragments reach their final velocity instantaneously, while the black dotted line represents a simulation in which this process is assumed to take 240 fs. (Reproduced from Paper II)

The results presented in Paper II, demonstrate the application of Coulomb explosion imaging in the investigation of the photochemical processes in molecules in a time-resolved experiment. Two main conclusions were drawn from this work: first, the application of covariance analysis (even on the existing dataset) would reveal more information on the structural dynamics and ion correlations, and second, the successful use of the FEL in a pump-probe scheme would allow the study of ultrafast structural and electronic dynamics in molecules, especially while also giving access to inner shell electrons, allowing site-specific photoionization.

4.3.2 Photodissociation dynamics of CH_2ClI

The study presented in Paper VI is a continuation of the work presented in Paper II. The results are also based on data, collected during extensive consecutive FEL measurement campaigns at FLASH; however, no time-resolved data was obtained with the FEL. The data was collected under identical conditions and by identical means to the data on which the results published in Paper II was collected. The photodissociation dynamics of two further halomethanes (CH_3I and CH_2ClI) was studied using VMI data from different delay times between the UV and IR laser pulses analog to the approach in Paper II. The VMI data was fragment-resolved due to the application of the PImMS camera. The velocity map images obtained from CH_2ClI are displayed in Fig. 4.19. The analysis of the data presented in Paper VI however, also used a covariance mapping approach to follow the Coulomb explosion channels in a time-resolved manner.

Velocity map images of CH_3I and CH_2ClI molecules were recorded in separate measurements after irradiation with UV and IR light pulses with variable delays. The delays ranged from -1 ps to 10.1 ps in steps of 0.1 ps, where negative delays denote the arrival of the IR light pulse first and the UV pulse last. Vice versa for positive delays. Since the covariance analysis was only applied to the CH_2ClI data, this summary will focus on the results ob-

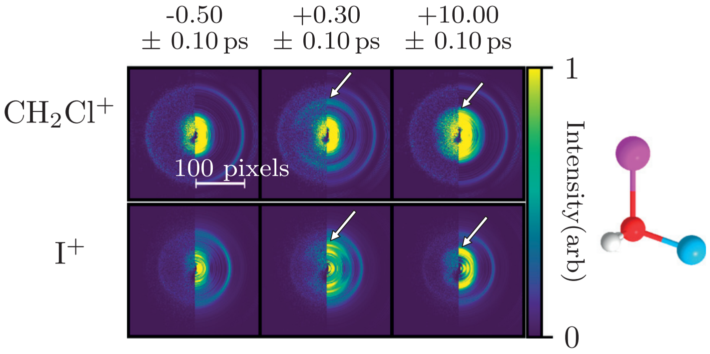

Figure 4.19: Momentum distributions of CH_2Cl^+ and I^+ recorded using the DVMIS at the CAMP endstation with the PImMS camera for delays of -0.5 ps, 0.3 ps, and 10.0 ps between pump and probe laser pulses. The left halves of the images show raw data, while the right halves show Abel-inverted images using the pBasex method. The arrows indicate time-dependent features observed for both fragments. (Figure reproduced from Paper VI)

tained from that molecule. Close to the pump wavelength of 272 nm lies the center of the CH_2ClI A-band (stretches from 225 to 325 nm). Excitation of this band is preferentially followed by cleavage of the C-I bond and photodissociation into neutral CH_2Cl and I radicals in the ground state or excited spin-orbit state.

The momentum distribution images (shown for selected delays in Fig. 4.19) were angularly integrated and plotted versus delay between the pump (UV) and probe (IR) laser pulses for the I^+ and the CH_2Cl^+ fragments. The resulting spectrogram is displayed in Fig. 4.20. Similar to the results from Paper II, one time-dependent (I) and two static channels (II and III) were observed in each fragment. Channel I originates from the cleavage of the C-I bond and subsequent dissociation after UV absorption. This photodissociation is probed by the IR pulse. IR photon absorption initiates Coulomb explosion into I^+ and CH_2Cl^+ fragments, whose final kinetic energy depends on the internuclear distance between the two fragments at the time of IR absorption. Thus, the recorded final kinetic energy decreases with increasing delay until the fragments reach their asymptotic energies at (0.27 ± 0.12) eV and (0.63 ± 0.30) eV for I^+ and CH_2Cl^+, respectively. The second channel (II) was attributed to originate from Coulomb explosion initiated by multiphoton absorption of IR photons only, with the charges being located on the halogen atoms. The third channel (III) was assigned to multiphoton dissociative ionization, yielding I^+ or CH_2Cl^+ photoions with neutral partners.

The molecular dynamics displayed in the three observed channels was further investigated using a recoil frame covariance mapping approach. Due to the use of the fast CCD camera (PImMS), the momentum distributions of the photoion fragments were directly accessible. The velocity map images recorded for CH_2Cl^+ were used as the X variable. From the I^+ momentum maps, the ion yield from ions with a constricted momentum, marked

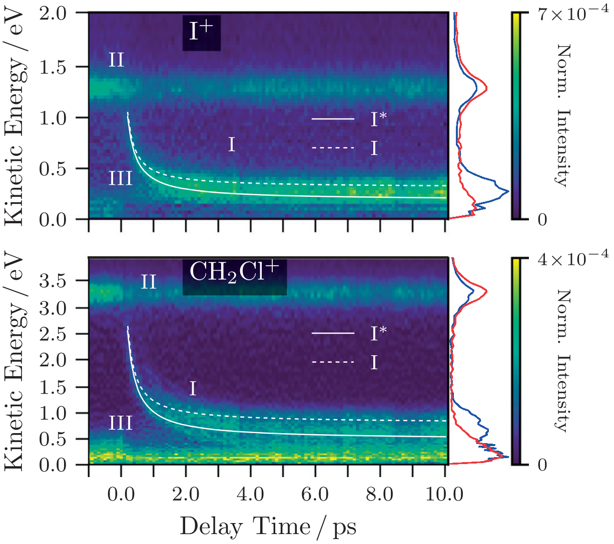

Figure 4.20: Kinetic energy spectrogram of I$^+$ ions (top) and CH$_2$Cl$^+$ ions (bottom), obtained from Abel-inverted momentum distributions. One time-dependent (I) and two static (II and III) channels are clearly visible for both fragments. Simulated curves for dissociation pathways leading to the ground state I($^2P_{3/2}$) (dashed) and to the spin-orbit excited state I*($^2P_{1/2}$) (solid) are drawn in white. (Reproduced from Paper VI.)

by the vertical arrow in Fig. 4.21, was chosen as variable **Y**. This will reveal which CH$_2$Cl$^+$ fragments are correlated to the selected I$^+$ ions. Of the observed processes, only Coulomb explosions produce charged fragments with correlated momentum vectors. Thus, it is expected to observe only covariance in channels that exhibit Coulomb explosions. This kind of analysis was termed recoil-frame covariance imaging [122]. Since the available data is time-resolved, this approach was repeated for several delays and the resulting time-dependent covariance maps are displayed in Fig. 4.21. At negative delays (leftmost frame), only one strong feature is visible, with opposite momentum as the selected I$^+$ ions. This is due to their momentum vectors, which point in opposite directions, resulting from the Coulomb explosion (momentum conservation). This feature was accordingly identified as originating from channel II, where multiphoton absorption of IR photons initiates a Coulomb explosion between the fragments I$^+$ and CH$_2$Cl$^+$. For positive delays a time-dependent feature appears, marked by a white cross. This feature was assigned to channel I. For increasing delays, the momentum of the CH$_2$Cl$^+$ is decreasing, as observed before in the spectrogram in Fig. 4.20. This observation confirms the earlier assignment of a UV initiated photodissociation, that is then probed with the IR pulse causing a subsequent Coulomb explosion. The more the photodissociation is progressed (later delays), the larger the internuclear distance between the fragment gets, therefore, causing the products of the Coulomb explosion to obtain smaller momenta. The low kinetic energy (and thus also momentum) features from channel III do not appear in the covariance maps, which con-

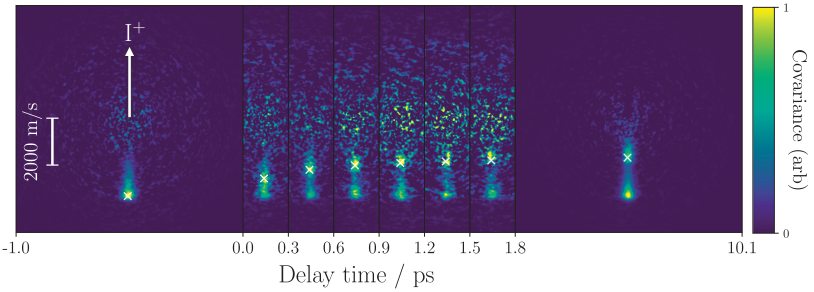

Figure 4.21: Recoil-frame covariance maps for different time delays between the pump (UV) and probe (IR) laser pulses. The maps represent the CH_2Cl^+ momentum correlation with respect to I^+ ions with their momentum vector constrained upwards in the images (white arrow). The time-dependent channel is marked with a white cross. (Reproduced from Paper VI.)

firms their assignment to dissociative ionization. These channels only produce either I^+ or CH_2Cl^+ with their respective neutral partners, and no charged fragments with correlated momenta.

In Paper VI, the photodissociation dynamics of iodomethane (CH_3I) and iodochloromethane (CH_2ClI) were successfully studied in a time-resolved manner using UV and IR laser pulses in a pump-probe scheme. As a continuation of the work in Paper II, the experimental and analytical approach were analogous. In Paper VI, however, recoil frame covariance mapping was applied successfully to the initiated Coulomb explosions in CH_2ClI, confirming previous assignments and gaining insight into the photofragment momentum correlations. It was concluded, that this approach could be used to study the structural dynamics of more complex photochemical processes.

4.3.3 Time-resolved inner-shell photoelectron spectroscopy of CH_3I

The results presented in Paper IV, are based on a FEL beamtime at FLASH, during which spatial and temporal overlap of the laser pump and FEL probe pulse were successfully established. The experimental scheme is otherwise identical to the approaches described in the previous section summarizing the results of Papers II and VI. A 100 fs long (FWHM) UV laser (272 nm) pump pulse was used to initiate the photodissociation in iodomethane (CH_3I) through C-I bond cleavage into neutral CH_3 and ground state $I(^2P_{3/2})$ or spin-orbit excited $I^*(^2P_{1/2})$. The 11.6 nm (107 eV) wavelength, 120 fs long (FWHM) FEL soft X-ray pulses employed as probe pulses are energetically close to the 4d centrifugal-barrier shape resonance in iodine [123]. Ionization of 4d electrons in iodine is therefore the dominant ionization channel observed, due to its tenfold higher ionization cross section at 107 eV than for valence ionization of CH_3I. The electron vacancies in the inner shells relax within few femtoseconds by one or several Auger processes. This leads to rapid fragmentation of the ions due to fast charge redistribution within the molecule. The main phenomenon ob-

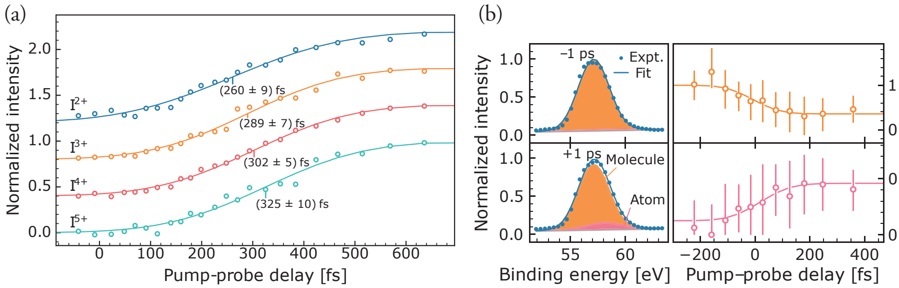

Figure 4.22: (a) Time-dependent multiply charged iodine ion yield with fits. (b) Analysis of iodine 4d photoelectron peak shape for negative and positive delays. The relative photoelectron yield for molecular and atomic distribution is shown on the right. (Adapted and reproduced from Paper IV.)

served in the photodissociation dynamics, is the transition of the iodine from being bound in the molecule to being an isolated atom. This transition was seen in the photoion as well as in the photoelectron data.

The absorption of the UV pump pulse initiates the photodissociation into neutral CH_3 and I by C-I bond cleavage. During this process the internuclear distance increases progressively. The absorption of one or multiple soft X-ray photons after a time delay predominantly leads to the release of electrons from the 4d orbital of iodine, followed by Auger process(es), creating localized charge(es) at iodine. The efficiency of charge redistribution within the molecule was found to be dependent on the delay between pump and probe pulse, evident by the increased yield of multiply charged iodine ions with longer delays, shown in Fig. 4.22(a). The increase in yield for the higher charge states seems to be slightly shifted to later times the more charged the ion is. This is attributed to the increasingly less efficient charge redistribution process for larger internuclear distances between the iodine and the methyl group and is seen as an indication of the transition from the molecule bound iodine to an isolated atom during the observed timeframe.

Further confirmation of this behavior was found in the photoelectron data. In particular the 4d photoelectron line of iodine was investigated. Atomic iodine has a binding energy of 58.3 eV for the 4d shell, but undergoes a chemical shift to 57.3 eV when bound in a CH_3I molecule. This chemical shift was observed in the time-dependent photoelectron data. Figure 4.22(b) shows the 4d photoelectron peak at negative (-1 ps) and positive delays (1 ps). For negative delays, the photodissociation process was not initiated before the soft X-ray light pulse ionized the molecules and a purely molecular feature is observed. For positive delays, a slight shift to higher binding energies is observed, indicating the emergence of atomic iodine that was probed. The time dependent yield of both the molecular (top) and atomic (bottom) contribution is shown on the right half of the image. The decay and rise times were found to be about 120 fs. The time resolution of the experiment is of the same order, indicating, that the process may occur on a faster timescale. Two calculations were presented in the paper that suggest the iodine to reach the atomic limit after 40 fs and respectively 45 fs.

In conclusion, Paper IV presents the time-resolved study of the photodissociation dynamics of CH_3I, specifically observing the transition of iodine from being bound in the molecule to being an isolated atom. While lacking the experimental time resolution to really resolve the transition, the study demonstrates that probing the process via inner-shell ionization is a viable method and potentially allows to follow processes on a shorter timescale than the analysis of the photoion data or valence shell ionization.

Summary and Outlook

The goal of the work presented in this thesis was to develop and apply experimental and analytical tools in order to study molecular dynamics not only on the nuclear, but also on the electronic timescale. The experiments presented in this thesis were carried out at the FLASH FEL in Hamburg and the High-Intensity XUV Beamline in Lund, exploiting the short pulse durations and photon energies in the XUV to soft X-ray range. Aside from the different light sources, two different experimental approaches have been pursued to gain insight into molecular dynamics. First, the pump-probe principle, which was applied during the FEL experiments in the form of IR-UV pump-probe (Papers II and VI) and UV-soft X-ray pump-probe (Paper IV). But also at the High-Intensity XUV Beamline efforts were made towards eventually implementing an XUV-XUV pump-probe scheme, by first establishing a high-intensity XUV light source capable of inducing nonlinear processes (Paper I). Subsequently, the importance of the XUV focusing and wavefront properties were identified and investigated (Papers III,VII and VIII).

The second approach that was pursued was the application of covariance mapping in an experimental scheme where photoion and photoelectron momenta are recorded simultaneously. In order to achieve this, a DVMIS was implemented at the High-Intensity XUV Beamline. This scheme was subsequently employed to study smaller molecules like nitrogen and more complex ones, such as adamantane.
Below, I will give some insight into current development and an outlook to the future plans concerning both covariance mapping as well as time-resolved experiments.

Towards photoion-photoelectron covariance mapping

Up to this point, the analysis of the photoion correlations has been very successful, however the study of the photoelectron correlations and dynamics was not as successful so far. This is attributed to higher noise levels on the electron detector and the relatively low photoelectron yield from the photoionization of larger molecular targets, that lead to significantly worse signal to noise ratios in the electron detection compared to the ion detection.

Recent efforts have, however, led to ion-electron covariance results obtained from recording of photoions and photoelectrons originating from the photoionization of carbon dioxide (CO_2) molecules. Analogous to the procedure applied in the ion-ion covariance, the correlation between the recorded species in the TOF spectra and the VMI signal was calculated. The CO_2 molecules were ionized with XUV light, produced via HHG, with photon energies between 20 eV and 45 eV. Four electronic states can be accessed: $X^2\Pi_g$, $A^2\Pi_u$, $B^2\Sigma_u^+$ and $C^2\Sigma_g^+$. Of these, only the C state leads to photodissociation into O^+ or CO^+ [87]. In a preliminary analysis, displayed in Fig.4.23, an increased correlation of the CO_2^+ ions with the X, A and B state was found and the O^+ and CO^+ ions (combined) show an increased correlation with the C state. The contributions caused by photoionization with photons from harmonic orders 15 and 17 are indicated in the correlation spectrum and assigned to the respective state. The difference spectrum exhibits negative signal for the C state, thus attributing the photoelectron signal to correlate with O^+ and CO^+ ions. The difference spectrum is positive, where photoelectrons from the X, A and B state are expected, correlating this signal with CO_2^+ ions. This is in agreement with the previous assignment of the dissociation behavior of the accessed electronic states. These results show that photoelectron-photoion covariance mapping is feasible at the High-Intensity XUV Beamline. The data is currently subject of further analysis. An effort to attribute the fragment contributions to the recorded photoelectrons for the presented adamantane data in a similar analysis is currently in progress as well. However, lower photoelectron yield and considerably broader spectral features make photoion-photoelectron covariance significantly more difficult when applied to larger molecules.

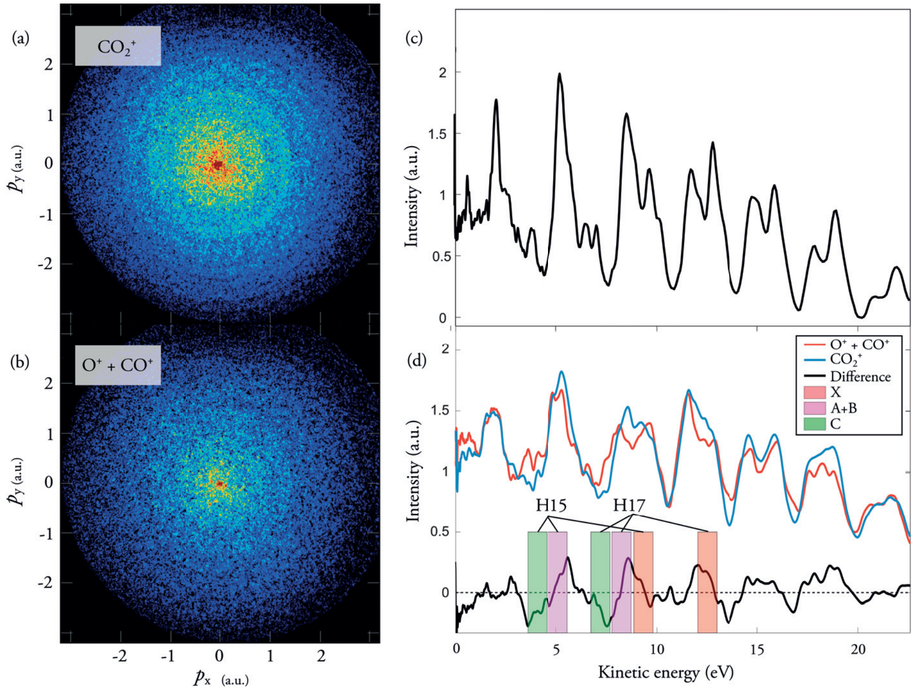

Figure 4.23: Photoion-photoelectron covariance results from photoionization of CO_2. (a) and (b) show photoelectron momentum maps in covariance with CO_2^+ and O^++CO^+ photoions, whose TOF spectra were recorded. The photoelectron spectrum calculated from the VMI data is shown in panel (c). (d) The covariance maps in (a) and (b) were Abel-inverted and angularly integrated to obtain the photoelectron covariance shown in red (O^++CO^+) and blue (CO_2). The calculated difference spectrum is displayed in black. The assigned contributions from the X, A+B and C states are indicated for photoelectrons produced by photons from harmonic orders 15 and 17.

Several improvements could be made to the photoelectron detection at the High-Intensity XUV Beamline: the elimination of sources of electron noise, like stray light and electrons liberated by ion impact would improve the signal-to-noise ratio; the increase of the photoelectron yield by e.g. higher intensities or higher target densities; and an increased laser repetition rate would reduce the acquisition time necessary to obtain sufficient statistics.

Towards time-resolved experiments with attosecond resolution

Time-resolved measurements involving soft X-ray pulses, produced by the FLASH FEL, have been performed over the course of this work. The results are presented in Paper IV. Subsequent measurement campaigns, involving IR-XUV and UV-XUV pump-probe schemes, on polycyclic aromatic hydrocarbons followed and the data is currently being analyzed. The temporal resolution in the experiments at FLASH, however, was limited by the pulse durations, which were on the order of 100 fs. The implementation of an XUV-IR interferometer is currently ongoing at the High-Intensity XUV Beamline. This would allow pump-probe experiments on molecules with femtosecond resolution as well as phase sensitive measurements in atoms.

Based on the static results on adamantane, which were presented in this work, a beamtime for a subsequent time-resolved experiment at the FLASH2 FEL was recently granted. The photodissociation dynamics will be studied in an XUV-XUV pump probe experiment in a coincidence detection scheme. The time-resolved imaging of ultrafast cage-opening, hydrogen transfer and the cation dissociation dynamics will be investigated in particular. The ability to record not only photoions in coincidence, but also the coincident photoelectrons with a temporal resolution below 100 fs will be very beneficial. The experiment is expected to answer some of the open questions concerning the dynamics during the photodissociation process that could not be accessed in the static study presented in this work.

On the way to performing pump-probe experiments with XUV pulses, the generation of XUV pulses that are intense enough to induce multiphoton processes, was a crucial step at the High-Intensity XUV Beamline. The XUV split-and-delay unit based on wavefront splitting [107], which has been developed and implemented prior and in parallel to the work presented in the thesis, will enable a range of time-resolved experiments that allow to directly probe molecular dynamics, even on the attosecond timescale, allowing the study of the electronic dynamics in addition to the nuclear dynamics.

References

[1] M. Born and R. Oppenheimer. Zur Quantentheorie der Molekeln. *Annalen der Physik*, 84(4):457, 1927.

[2] E. Condon. A Theory of Intensity Distribution in Band Systems. *Physical Review*, 28(6):1182–1201, 1926.

[3] F. Calegari, D. Ayuso, A. Trabattoni, et al. Ultrafast electron dynamics in phenylalanine initiated by attosecond pulses. *Science*, 346(6207):336–339, 2014.

[4] Zewail. Laser Femtochemistry. *Science*, 242:1645, 1988.

[5] W. E. Lamb. Theory of an Optical Maser. *Physical Review*, 134(6A):A1429–A1450, 1964.

[6] L. E. Hargrove, R. L. Fork, and M. A. Pollack. Locking of He–Ne Laser Modes Induced by Synchronous Intracavity Modulation. *Applied Physics Letters*, 5(1):4–5, 1964.

[7] D. Strickland and G. Mourou. Compression of amplified chirped optical pulses. *Optics Communications*, 55(6):447–449, 1985.

[8] M. Drescher, M. Hentschel, R. Kienberger, et al. X-ray pulses approaching the attosecond frontier. *Science*, 291(5510):1923–1927, 2001.

[9] P. M. Paul. Observation of a Train of Attosecond Pulses from High Harmonic Generation. *Science*, 292(5522):1689–1692, 2001.

[10] M. Hentschel, R. Kienberger, C. Spielmann, et al. Attosecond metrology. *Nature*, 414(6863):509–513, 2001.

[11] P. B. Corkum and F. Krausz. Attosecond science. *Nature Physics*, 3(6):381–387, 2007.

[12] J. M. J. Madey. Stimulated Emission of Bremsstrahlung in a Periodic Magnetic Field. *Journal of Applied Physics*, 42(5):1906–1913, 1971.

[13] S. Schreiber. First Lasing At 32 Nm of the Vuv-Fel At Desy. *Proceedings of the 27th International Free Electron Laser Conference*, (August):12–18, 2005.

[14] C. Pellegrini, A. Marinelli, and S. Reiche. The physics of x-ray free-electron lasers. *Reviews of Modern Physics*, 88(1):015006, 2016.

[15] A. McPherson, G. Gibson, H. Jara, et al. Studies of multiphoton production of vacuum-ultraviolet radiation in the rare gases. *Journal of the Optical Society of America B*, 4(4):595, 1987.

[16] M. Ferray, A. L'Huillier, X. F. Li, et al. Multiple-harmonic conversion of 1064 nm radiation in rare gases. *Journal of Physics B: Atomic, Molecular and Optical Physics*, 21(3):L31–L35, 1988.

[17] S. Schreiber, K. Honkavaara, B. Faatz, et al. Status of the Flash Facility. *Proceedings of FEL2012, Nara, Japan*, pages 4–7, 2012.

[18] P. Rudawski, C. M. Heyl, F. Brizuela, et al. A high-flux high-order harmonic source. *Review of Scientific Instruments*, 84(7), 2013.

[19] D. Oepts, A. van der Meer, and P. van Amersfoort. The Free-Electron-Laser user facility FELIX. *Infrared Physics & Technology*, 36(1):297–308, 1995.

[20] V. Ayvazyan, N. Baboi, J. Bähr, et al. First operation of a free-electron laser generating GW power radiation at 32 nm wavelength. *The European Physical Journal D*, 37(2):297–303, 2006.

[21] P. Emma, R. Akre, J. Arthur, et al. First lasing and operation of an ångstrom-wavelength free-electron laser. *Nature Photonics*, 4(9):641–647, 2010.

[22] T. Ishikawa, H. Aoyagi, T. Asaka, et al. A compact X-ray free-electron laser emitting in the sub-ångström region. *Nature Photonics*, 6(8):540–544, 2012.

[23] E. Allaria, R. Appio, L. Badano, et al. Highly coherent and stable pulses from the FERMI seeded free-electron laser in the extreme ultraviolet. *Nature Photonics*, 6(10):699–704, 2012.

[24] M. Svandrlik, E. Allaria, F. Bencivenga, et al. Fermi status report. *5th International Particle Accelerator Conference*, pages 2885–2887, 2012.

[25] M. Altarelli. XFEL Technical Design Report http://xfel.desy.de/technical information/tdr/tdr/. Technical report, 2007.

[26] M. Yoon, W. H. Hwang, D. E. Kim, et al. A 0.1 nm SASE FEL at Pohang Accelerator Laboratory. *Preoceedings of FEL08*, pages 218–221, 2008.

[27] C. Milne, T. Schietinger, M. Aiba, et al. SwissFEL: The Swiss X-ray Free Electron Laser. *Applied Sciences*, 7(7):720, 2017.

[28] R. W. Schoenlein, S. Boutet, M. P. Minitti, and A. M. Dunne. The Linac Coherent Light Source: Recent Developments and Future Plans. *Applied Sciences*, 7(8):850, 2017.

[29] K. Wille. *The Physics of Particle Accelerators*. Clarendon Press, 2001.

[30] D. H. Bilderback, P. Elleaume, and E. Weckert. Review of third and next generation synchrotron light sources. *Journal of Physics B: Atomic, Molecular and Optical Physics*, 38(9):S773–S797, 2005.

[31] L. B. Fletcher, H. J. Lee, T. Döppner, et al. Ultrabright X-ray laser scattering for dynamic warm dense matter physics. *Nature Photonics*, 9(4):274–279, 2015.

[32] S. Schorb, T. Gorkhover, J. P. Cryan, et al. X-ray-optical cross-correlator for gas-phase experiments at the Linac Coherent Light Source free-electron laser. *Applied Physics Letters*, 100(12), 2012.

[33] H. N. Chapman, A. Barty, M. J. Bogan, et al. Femtosecond diffractive imaging with a soft-X-ray free-electron laser. *Nature Physics*, 2(12):839–843, 2006.

[34] A. Barty, S. Boutet, M. J. Bogan, et al. Ultrafast single-shot diffraction imaging of nanoscale dynamics. *Nature Photonics*, 2(7):415–419, 2008.

[35] L. Young, E. P. Kanter, B. Kräsignssig, et al. Femtosecond electronic response of atoms to ultra-intense X-rays. *Nature*, 466(7302):56–61, 2010.

[36] C. Pellegrini. The history of X-ray free-electron lasers. *European Physical Journal H*, 37(5):659–708, 2012.

[37] A. M. Kondratenko and E. L. Saldin. Generation of coherent radiation by a relativistic electron beam in an ondulator*. *Zhurnal Tekhnicheskoi Fiziki*, 10:207–216, 1980.

[38] Y. Derbenev, A. Kondratenko, and E. Saldin. On the possibility of using a free electron laser for polarization of electrons in storage rings. *Nuclear Instruments and Methods in Physics Research*, 193(3):415–421, 1982.

[39] J. Murphy and C. Pellegrini. Free electron lasers for the XUV spectral region. *Nuclear Instruments and Methods in Physics Research Section A: Accelerators, Spectrometers, Detectors and Associated Equipment*, 237(1-2):159–167, 1985.

[40] W. Ackermann, G. Asova, V. Ayvazyan, et al. Operation of a free-electron laser from the extreme ultraviolet to the water window. *Nature Photonics*, 1(6):336–342, 2007.

[41] B. Erk, J. P. Müller, C. Bomme, et al. CAMP@FLASH: an end-station for imaging, electron- and ion-spectroscopy, and pump–probe experiments at the FLASH free-electron laser. *Journal of Synchrotron Radiation*, 25(5):1529–1540, 2018.

[42] A. V. Baez and P. Kirkpatrick. Formation of Optical Images by X-Rays X-RAY OPTICS. *Journal of the Optical Society of America*, 38(9):766–774, 1948.

[43] U. Even. Pulsed Supersonic Beams from High Pressure Source: Simulation Results and Experimental Measurements. *Advances in Chemistry*, 2014(Section 3):1–11, 2014.

[44] U. Even. "The Even-Lavie valve as a source for high intensity supersonic beam". *EPJ Techniques and Instrumentation*, 2(1):17, 2015.

[45] M. V. Ammosov and V. P. Krainov. Tunnel ionization of complex atoms and of atomic ions in an alternating electromagnetic field. *Sov.Phys.JETP*, 6(64):4–7, 1986.

[46] L. V. Keldysh. Ionization in the field of a strong electromagnetic wave. *SOVIET PHYSICS JETP*, 20(5):1945–1957, 1965.

[47] Corkum. Plasma perspective on strong field multiphoton ionization. *Physical review letters*, 71(13):1994–1997, 1994.

[48] K. J. Schafer, B. Yang, L. F. Dimauro, and K. C. Kulander. Above threshold ionization beyond the high harmonic cutoff. *Physical Review Letters*, 70(11):1599–1602, 1993.

[49] J. L. Krause, K. J. Schafer, and K. C. Kulander. High-order harmonic generation from atoms and ions in the high intensity regime. *Physical Review Letters*, 68(24):3535–3538, 1992.

[50] M. Lewenstein, P. Balcou, M. Y. Ivanov, A. L'Huillier, and P. B. Corkum. Theory of high-harmonic generation by low-frequency laser fields. *Physical Review A*, 49(3):2117–2132, 1994.

[51] Y. Mairesse. Attosecond Synchronization of High-Harmonic Soft X-rays. *Science*, 302(5650):1540–1543, 2003.

[52] M. Holler, F. Schapper, L. Gallmann, and U. Keller. Attosecond electron wave-packet interference observed by transient absorption. *Physical Review Letters*, 106(12):1–4, 2011.

[53] M. Lewenstein, K. C. Kulander, K. J. Schafer, and P. H. Bucksbaum. Rings in above-threshold ionization: A quasiclassical analysis. *Physical Review A*, 51(2):1495–1507, 1995.

[54] P. Salières, A. L'Huillier, and M. Lewenstein. Coherence Control of High-Order Harmonics. *Physical Review Letters*, 74(19):3776–3779, 1995.

[55] K. Varjú, Y. Mairesse, B. Carré, et al. Frequency chirp of harmonic and attosecond pulses. *Journal of Modern Optics*, 52(2-3):379–394, 2005.

[56] S. Carlström, J. Preclíková, E. Lorek, et al. Spatially and spectrally resolved quantum path interference with chirped driving pulses. *New Journal of Physics*, 18(12):123032, 2016.

[57] C. Guo, A. Harth, S. Carlström, et al. Phase control of attosecond pulses in a train. *Journal of Physics B: Atomic, Molecular and Optical Physics*, 51(3):034006, 2018.

[58] A. L'Huillier, P. Balcou, S. Candel, K. J. Schafer, and K. C. Kulander. Calculations of high-order harmonic-generation processes in xenon at 1064 nm. *Physical Review A*, 46(5):2778–2790, 1992.

[59] A. L'Huillier, X. F. Li, and L. A. Lompré. Propagation effects in high-order harmonic generation in rare gases. *Journal of the Optical Society of America B*, 7(4):527, 1990.

[60] S. Kazamias, S. Daboussi, O. Guilbaud, et al. Pressure-induced phase matching in high-order harmonic generation. *Physical Review A - Atomic, Molecular, and Optical Physics*, 83(6):1–6, 2011.

[61] C. M. Heyl, C. L. Arnold, A. Couairon, and A. L'Huillier. Introduction to macroscopic power scaling principles for high-order harmonic generation. *Journal of Physics B: Atomic, Molecular and Optical Physics*, 50(1), 2017.

[62] S. Kazamias, D. Douillet, F. Weihe, et al. Global optimization of high harmonic generation. *Physical Review Letters*, 90(19):193901/1–193901/4, 2003.

[63] M. B. Gaarde, J. L. Tate, and K. J. Schafer. Macroscopic aspects of attosecond pulse generation. *Journal of Physics B: Atomic, Molecular and Optical Physics*, 41(13), 2008.

[64] C. M. Heyl, H. Coudert-Alteirac, M. Miranda, et al. Scale-invariant nonlinear optics in gases. *Optica*, 3(1):75, 2016.

[65] A. V. Husakou and J. Herrmann. Supercontinuum generation of higher-order solitons by fission in photonic crystal fibers. *Physical Review Letters*, 87(20):203901–1–203901–4, 2001.

[66] E. Constant, D. Garzella, P. Breger, et al. Optimizing High Harmonic Generation in Absorbing Gases: Model and Experiment. *Physical Review Letters*, 82(8):1668–1671, 1999.

[67] E. Takahashi, Y. Nabekawa, and K. Midorikawa. Generation of 10-μJ coherent extreme-ultraviolet light by use of high-order harmonics. *Optics Letters*, 27(21):1920, 2002.

[68] J.-F. Hergott, M. Kovacev, H. Merdji, et al. Extreme-ultraviolet high-order harmonic pulses in the microjoule range. *Physical Review A*, 66(2):021801, 2002.

[69] E. Skantzakis, P. Tzallas, J. Kruse, C. Kalpouzos, and D. Charalambidis. Coherent continuum extreme ultraviolet radiation in the sub-100-nJ range generated by a high-power many-cycle laser field. *Optics Letters*, 34(11):1732, 2009.

[70] B. Bergues, D. E. Rivas, M. Weidman, et al. Tabletop nonlinear optics in the 100-eV spectral region. *Optica*, 5(3):237, 2018.

[71] S. Kühn, M. Dumergue, S. Kahaly, et al. The ELI-ALPS facility: the next generation of attosecond sources. *Journal of Physics B: Atomic, Molecular and Optical Physics*, 50(13):132002, 2017.

[72] A. Harth, C. Guo, Y.-C. Cheng, et al. Compact 200 kHz HHG source driven by a few-cycle OPCPA. *Journal of Optics*, 20(1):014007, 2018.

[73] H. Wolter. Spiegelsysteme streifenden Einfalls als abbildende Optiken für Röntgenstrahlen. *Annalen der Physik*, 445(1-2):94–114, 1952.

[74] C. Cherry, M. H. Kubba, D. E. Pearson, and M. P. Barton. An Experimental Study of the Possible Bandwidth Compression of Visual Image Signals. *Proceedings of the IEEE*, 51(11):1507–1517, 1963.

[75] W. C. Wiley and I. H. McLaren. Time of Flight Mass Spectrometer with Improved Resolution. *Review of Scientific Instruments*, 26(12):1150–1157, 1955.

[76] P. Kruit and F. H. Read. Magnetic field paralleliser for 2 phi electron spectrometer and electron magnifier. *J. Phys. E*, 16:313–324, 1983.

[77] A. T. J. B. Eppink and D. H. Parker. Velocity map imaging of ions and electrons using electrostatic lenses: Application in photoelectron and photofragment ion imaging of molecular oxygen. *Review of Scientific Instruments*, 68(9):3477, 1997.

[78] D. A. Dahl. SIMION for the personal computer in reflection. *International Journal of Mass Spectrometry*, 200(1-3):3–25, 2000.

[79] L. Montgomery Smith, D. R. Keefer, and S. Sudharsanan. Abel inversion using transform techniques. *Journal of Quantitative Spectroscopy and Radiative Transfer*, 39(5):367–373, 1988.

[80] M. J. J. Vrakking. An iterative procedure for the inversion of two-dimensional ion/photoelectron imaging experiments. *Review of Scientific Instruments*, 72(11):4084, 2001.

[81] O. Ghafur, W. Siu, P. Johnsson, et al. A velocity map imaging detector with an integrated gas injection system. *Review of Scientific Instruments*, 80(3), 2009.

[82] C. S. Lehmann, N. B. Ram, and M. H. M. Janssen. Velocity map photoelectron-photoion coincidence imaging on a single detector. *Review of Scientific Instruments*, 83(9), 2012.

[83] A. Zhao, P. Sándor, and T. Weinacht. Coincidence velocity map imaging using a single detector. *Journal of Chemical Physics*, 147(1), 2017.

[84] T. Arion and U. Hergenhahn. Coincidence spectroscopy: Past, present and perspectives. *Journal of Electron Spectroscopy and Related Phenomena*, 200:222–231, 2015.

[85] L. J. Frasinski, K. Codling, and P. A. Hatherly. Covariance Mapping: A Correlation Method Applied to Multiphoton Multiple Ionization. *Science*, 246(4933):1029–1031, 1989.

[86] W. Bothe and W. Kolhörster. Das Wesen der Höhenstrahlung. *Zeitschrift für Physik*, 56(11-12):751–777, 1929.

[87] J. H. D. Eland. Predissociation of triatomic ions studied by photo-electron-photoion coincidence spectroscopy and photoion kinetic energy analysis. I. CO2 +. *International Journal of Mass Spectrometry and Ion Physics*, 9(4):397–406, 1972.

[88] K. E. McCulloh, T. E. Sharp, and H. M. Rosenstock. Direct Observation of the Decomposition of Multiply Charged Ions into Singly Charged Fragments. *The Journal of Chemical Physics*, 42(10):3501–3509, 1965.

[89] J. Eland. The dynamics of three-body dissociations of dications studied by the triple coincidence technique PEPIPICO. *Molecular Physics*, 61(3):725–745, 1987.

[90] S. Martin, R. Brédy, A. R. Allouche, et al. Coincidence method for measuring the mass of neutral fragments emitted in a delayed fragmentation process from a singly charged molecule: Fragmentation pathway of adenine. *Physical Review A*, 77(6):062513, 2008.

[91] H. W. Haak, G. A. Sawatzky, and T. D. Thomas. Auger-Photoelectron Coincidence Measurements in Copper. *Physical Review Letters*, 41(26):1825–1827, 1978.

[92] G. Prümper and K. Ueda. Electron-ion-ion coincidence experiments for photofragmentation of polyatomic molecules using pulsed electric fields: Treatment of random coincidences. *Nuclear Instruments and Methods in Physics Research, Section A: Accelerators, Spectrometers, Detectors and Associated Equipment*, 574(2):350–362, 2007.

[93] L. J. Frasinski. Covariance mapping techniques. *Journal of Physics B: Atomic, Molecular and Optical Physics*, 49(15):152004, 2016.

[94] W. J. Krzanowski. *Principles of Multivariate Analysis*. Oxford University Press, Oxford, 1 edition, 1988.

[95] V. Zhaunerchyk, L. J. Frasinski, J. H. D. Eland, and R. Feifel. Theory and simulations of covariance mapping in multiple dimensions for data analysis in high-event-rate experiments. *Physical Review A - Atomic, Molecular, and Optical Physics*, 89(5):1–8, 2014.

[96] M. Lucchini, K. Kim, F. Calegari, et al. Autoionization and ultrafast relaxation dynamics of highly excited states in N 2. *Physical Review A - Atomic, Molecular, and Optical Physics*, 86(4):1–4, 2012.

[97] M. Eckstein, C. H. Yang, M. Kubin, et al. Dynamics of N2dissociation upon inner-valence ionization by wavelength-selected XUV pulses. *Journal of Physical Chemistry Letters*, 6(3):419–425, 2015.

[98] T. Aoto, K. Ito, Y. Hikosaka, et al. Inner-valence states of N2+ and the dissociation dynamics studied by threshold photoelectron spectroscopy and configuration interaction calculation. *Journal of Chemical Physics*, 124(23):234306, 2006.

[99] S. Stauss and K. Terashima. *Diamondoids: Synthesis, Properties, and Applications*. CRC Press, 2017.

[100] H. Schwertfeger, A. A. Fokin, and P. R. Schreiner. Diamonds are a Chemist's Best Friend: Diamondoid Chemistry Beyond Adamantane. *Angewandte Chemie International Edition*, 47(6):1022–1036, 2008.

[101] J. E. Wolf, D. Kaplan, S. J. Kraus, et al. Efficacy and tolerability of combined topical treatment of acne vulgaris with adapalene and clindamycin: a multicenter, randomized, investigator-blinded study. *Journal of the American Academy of Dermatology*, 49(3):S211–S217, 2003.

[102] X. Jing, C. Ma, Y. Ohigashi, et al. Functional studies indicate amantadine binds to the pore of the influenza A virus M2 proton-selective ion channel. *Proceedings of the National Academy of Sciences*, 105(31):10967–10972, 2008.

[103] E. Anders and E. Zinner. Interstellar Grains in Primitive Meteorites: Diamond, Silicon Carbide, and Graphite. *Meteoritics*, 28(4):490–514, 1993.

[104] T. Henning and F. Salama. Carbon in the Universe. *Science*, 282(5397):2204–2210, 1998.

[105] B. Acke and M. E. van den Ancker. A survey for nanodiamond features in the 3 micron spectra of Herbig Ae/Be stars. *Astronomy & Astrophysics*, 457(1):171–181, 2006.

[106] K. Lenzke, L. Landt, M. Hoener, et al. Experimental determination of the ionization potentials of the first five members of the nanodiamond series. *The Journal of Chemical Physics*, 127(8):084320, 2007.

[107] F. Campi, H. Coudert-Alteirac, M. Miranda, et al. Design and test of a broadband split-and-delay unit for attosecond XUV-XUV pump-probe experiments. *Review of Scientific Instruments*, 87(2):023106, 2016.

[108] P. Tzallas, D. Charalambidis, N. A. Papadogiannis, K. Witte, and G. D. Tsakiris. Direct observation of attosecond light bunching. *Nature*, 426(6964):267–271, 2003.

[109] Y. Nabekawa, H. Hasegawa, E. J. Takahashi, and K. Midorikawa. Production of Doubly Charged Helium Ions by Two-Photon Absorption of an Intense Sub-10-fs Soft X-Ray Pulse at 42 eV Photon Energy. *Physical Review Letters*, 94(4):043001, 2005.

[110] P. Tzallas, E. Skantzakis, L. A. A. Nikolopoulos, G. D. Tsakiris, and D. Charalambidis. Extreme-ultraviolet pump–probe studies of one-femtosecond-scale electron dynamics. *Nature Physics*, 7(10):781–784, 2011.

[111] E. J. Takahashi, P. Lan, O. D. Mücke, Y. Nabekawa, and K. Midorikawa. Attosecond nonlinear optics using gigawatt-scale isolated attosecond pulses. *Nature Communications*, 4(1):2691, 2013.

[112] A. M. Covington, A. Aguilar, I. R. Covington, et al. Photoionization of Ne+ using synchrotron radiation. *Physical Review A*, 66(6):062710, 2002.

[113] J. B. West and G. V. Marr. The Absolute Photoionization Cross Sections of Helium, Neon, Argon and Krypton in the Extreme Vacuum Ultraviolet Region of the Spectrum. *Proceedings of the Royal Society A: Mathematical, Physical and Engineering Sciences*, 349(1658):397–421, 1976.

[114] M. Førre, S. Selstø, and R. Nepstad. Nonsequential two-photon double ionization of atoms: Identifying the mechanism. *Physical Review Letters*, 105(16):1–4, 2010.

[115] B. C. Platt and R. Shack. History and Principles of Shack-Hartmann Wavefront Sensing. *Journal of Refractive Surgery*, 17(5):S573–S577, 2001.

[116] L. Poletto, F. Frassetto, F. Calegari, A. Trabattoni, and M. Nisoli. Micro-focusing of XUV attosecond pulses by grazing-incidence toroidal mirrors. In *2013 Conference on Lasers & Electro-Optics Europe & International Quantum Electronics Conference CLEO EUROPE/IQEC*, volume 21, pages 1–1. IEEE, 2013.

[117] C. Bourassin-Bouchet, M. M. Mang, F. Delmotte, P. Chavel, and S. de Rossi. How to focus an attosecond pulse. *Optics Express*, 21(2):2506, 2013.

[118] E. Frumker, G. G. Paulus, H. Niikura, D. M. Villeneuve, and P. B. Corkum. Wavefront Characterization. *Optics Letters*, 34(19):3026–3028, 2009.

[119] A. Nomerotski, M. Brouard, E. Campbell, et al. Pixel Imaging Mass Spectrometry with fast and intelligent Pixel detectors. *Journal of Instrumentation*, 5(07):C07007–C07007, 2010.

[120] A. T. Clark, J. P. Crooks, I. Sedgwick, et al. Multimass Velocity-Map Imaging with the Pixel Imaging Mass Spectrometry (PImMS) Sensor: An Ultra-Fast Event-Triggered Camera for Particle Imaging. *The Journal of Physical Chemistry A*, 116(45):10897–10903, 2012.

[121] G. A. Garcia, L. Nahon, and I. Powis. Two-dimensional charged particle image inversion using a polar basis function expansion. *Review of Scientific Instruments*, 75(11):4989–4996, 2004.

[122] C. S. Slater, S. Blake, M. Brouard, et al. Coulomb-explosion imaging using a pixel-imaging mass-spectrometry camera. 053424:1–14, 2015.

[123] S. T. Manson and J. W. Cooper. Photo-Ionization in the Soft x-Ray Range: 1 Z Dependence in a Central-Potential Model. *Physical Review*, 165(1):126–138, 1968.

Scientific publications

The author's contributions

Paper I: Two-photon double ionization of neon using an intense attosecond pulse train

This was the first experiment in which I participated, at the beginning of my PhD studies. I participated in performing the experiment, especially the high-order harmonic generation in krypton using the absorption cell to shift the cutoff. I was involved in the discussions on the manuscript, especially concerning the question of whether the sequential or direct process dominates and gave feedback on the manuscript.

Paper II: Coulomb-explosion imaging of concurrent CH2BrI photodissociation dynamics

During this FEL beamtime, the overlap between the FEL and the optical laser could not be established. A part of the people involved in the beamtime, including me, decided to run an auxiliary experiment, between the FEL shifts, involving only the optical laser. I played a substantial experimental role in that experiment, especially the laser part. I did not take part in the analysis, but gave feedback on the manuscript.

Paper III: Micro-Focusing of Broadband High-Order Harmonic Radiation by a Double Toroidal Mirror

From the state of the High-Intensity XUV Beamline in Paper I towards the ability to perform the XUV wavefront sensor measurements presented in this paper, major rebuilding and upgrades were performed, in which I was greatly involved. I took part in preparing and performing the experiment. I was involved in scientific discussions, and gave feedback on the manuscript.

Paper IV: Time-resolved inner-shell photoelectron spectroscopy: From a bound molecule to an isolated atom

During this FEL experiment, the overlap of the optical laser and the FEL was established, to which I contributed. I was involved in most parts of the experiment. I did not perform the analysis, but gave feedback on the manuscript.

Paper V: A Versatile Velocity Map Ion-Electron Covariance Imaging Spectrometer for High-Intensity XUV Experiments

At the beginning of my PhD studies, the DVMIS had already been conceptualized and designed. I participated in assembling and commissioning of the single-sided VMIS and subsequently the DVMIS. Linnea Rading wrote the first half of the paper, regarding the technical design and performance of the DVMIS. I performed simulations, and made major changes to the entire manuscript. Sylvain Maclot performed simulations and contributed substantially to the manuscript and analysis through discussions and feedback. I wrote the second half of the manuscript, presenting the practical implementation of the DVMIS as a tool for covariance mapping. I was the lead experimental investigator and developed and implemented the synchronized data acquisition scheme. I analyzed the nitrogen data and performed the covariance analysis.

Paper VI: Coulomb explosion imaging of CH3I and CH2ClI photodissociation dynamics

This paper is based on data, obtained in the same auxiliary experiment as in Paper II. I played an important experimental role, especially in the laser part. I gave feedback on the manuscript, but did not take part in the analysis.

Paper VII: Spatio–temporal coupling of attosecond pulses

I was involved in preparing the HHG beamline for this experiment and played a minor experimental role. I was involved in discussions on the manuscript and gave feedback on the drafts.

Paper VIII: Single-shot extreme-ultraviolet wavefront measurements of high-order harmonics

This paper is based on wavefront measurements similar to those in Paper III. I was significantly involved in upgrading and developing the HHG beamline, partially in preparation for this experiment. I contributed to discussions on the manuscript and gave feedback on the drafts.

Printed by Media-Tryck, Lund 2019 NORDIC SWAN ECOLABEL 3041 0903

LUND
UNIVERSITY

Lund University,
Faculty of Engineering
Department of Physics

ISBN 978-91-7753-976-6
ISSN 0281-2762
Lund Reports on Atomic Physics, LRAP 554 (2019